Title:
Fact or friction: Inferring rheology from nonvolcanic tremor and low-frequency earthquakes on the deep San Andreas fault

Author:
Thomas, Amanda

Acceptance Date:
2012

Series:
UC Berkeley Electronic Theses and Dissertations

Degree:
Ph.D., Earth & Planetary ScienceUC Berkeley

Advisor(s):
Burgmann, Roland

Committee:
Dreger, Douglas, Brillinger, David

Permalink:
http://escholarship.org/uc/item/3dm2m115

Abstract:

Fact or friction: Inferring rheology from nonvolcanic tremor and low-frequency earthquakes on the deep San Andreas fault

by

Amanda Thomas

A dissertation submitted in partial satisfaction of the
requirements for the degree of
Doctor of Philosophy

in

Earth and Planetary Science

in the

Graduate Division

of the

University of California, Berkeley

Committee in charge:

Professor Roland Bürgmann, Chair
Professor Douglas Dreger
Professor David Brillinger

Fall 2012

Fact or friction: Inferring rheology from nonvolcanic tremor and low-frequency earthquakes on the deep San Andreas fault

Abstract

Fact or friction: Inferring rheology from nonvolcanic tremor and low-frequency earthquakes on the deep San Andreas fault

by

Amanda Thomas

Doctor of Philosophy in Earth and Planetary Science

University of California, Berkeley

Professor Roland Bürgmann, Chair

Here I present results from a collection of three papers that document the response of deep non-volcanic tremor and constituent low-frequency earthquakes to stress perturbations from the Earth tides. Variations in the seismicity rate are used to constrain the rheology of the deep San Andreas fault and to infer *in situ* conditions in the deep crust. I find that effective stresses orders of magnitude smaller than expected can explain observed response of non-volcanic tremor and low-frequency earthquakes to primarily small, tidally-induced shear stresses. Low effective stress also provides a mechanism for frictional slip to occur in environments where elevated temperature and pressure conditions are thought to make ductile creep processes the favored mode of deformation.

To my family in Georgia

Contents

List of Figures

List of Tables

Acknowledgments

First, I would like to thank my family for their love and support over the past five years, for calling me on my birthday, and forgiving me when I forgot to call on theirs. Completing a thesis would have been much more difficult without the stability they provide in my personal life. Second, I thank a group of people I like to call my entourage namely Jim Watkins, David Shimabukuro, KT King, Nick Beeler, Sue Beeler, Ved Lekic, Jana Broadhurst, Leif Karlstrom, Max Rudolph, Joanne Emerson, Edwin Kite, Dan Evans, Jenny Druhan, Ian Rose, Colin Amos, Pascal Audet, Manoo Shirzaei, Brent Delbridge, Brian Kessler, Ayesha Johnson, Kelly Wiseman, and Zach Geballe. Third, I thank all of the staff that made sure my paychecks arrived eventually and for technical support that usually came with an unwarranted smile. Fourth, I would like to thank the faculty members that are not on my committee but had open doors and allowed me to come through them, unannounced, to ask questions. Finally, I thank David Brillinger for his patience and conversation, Douglas Dreger for his patience and taking me to 49ers games, and Roland Bürgmann for his patience and being a kind, inspiring role model.

Chapter 1

Introduction

Strain energy within the Earth is released on faults that can either rupture abruptly–causing hazardous earthquakes–or slip slowly in largely aseismic events that can last hours to years. The physical mechanisms that govern the transition between slow, aseismic and fast, seismic slip are not well understood. Here, I study the influence of the small stresses induced in the crust on the occurence of a very special class of small earthquakes that occur on deep faults and are diagnostic of slow slip events. Deep faults were once thought to be completely aseismic because conditions at the depths where non-volcanic tremor and low-frequency earthquakes (LFEs) occur, such as elevated pressure and temperature, should favor ductile creep over frictional slip. Since the deep crust was once thought to be incapable of hosting earthquakes, very little is known about its mechanical behavior. The recently discovered suite of seismic events that do occur there provide a means of studying this previously inaccessible region of the Earth's interior. The response of these earthquakes to small stress perturbations can be used to infer both the rheology of deep fault zones as well as probe the *in situ* conditions deep in the crust. Such information is interesting for two reasons. First, from a basic science standpoint, study of transient fault slip phenomena improves our understanding of the anatomy of fault zones, particularly where and how slip is accommodated, how stress is transferred within the crust, and which physical characteristics of faults are responsible for earthquake ground motions. Second, earthquake forecasts and ground motion estimates predict the probability of a large earthquake, the intensity of shaking, and its potential impact on a region of interest. These tools rely heavily on estimated parameters such as magnitude, recurrence interval, and rupture area. While deep slip could potentially influence each of these parameters, its effect is excluded from rupture forecasts because it is neither well characterized nor well understood. Incorporating the results gleaned from studies of slow-slip phenomena into earthquake forecasts and ground motion simulations may improve such models.

1.1 Transient fault slip

Recently, due largely to improvements in the quality of seismic recording instruments, a new class of deep fault slip phenomena have been observed in fault zones worldwide. These events, collectively dubbed transient fault slip, are different from standard earthquakes in a number of ways. First, transient fault slip, in general, occurs on the deep extensions of faults below the "seismogenic zone" in a part of the fault previously thought to be incapable of hosting earthquakes. Second, these fault slip phenomena obey different moment-duration scaling relationships than regular earthquakes do. In standard earthquakes moment scales with the cube of duration while in slow earthquakes moment is proportional to duration. Third, such events, in some cases, are very nearly periodic. Fourth, the seismic manifestation of deep fault slip is depleted in frequency content relative to regular earthquakes and does not appear to have the same spectral character (though this fact is poorly documented and will be a topic of future research). Fifth, many transient fault slip phenomena are extremely sensitive to very small stress perturbations such as those from passing surface waves from distant teleseismic earthquakes, static stress changes from nearby earthquakes, and the periodic fluctuations in stress caused by the solid Earth tides. Sixth, transient fault slip is oberved in many places but it is not observed everywhere.

1.2 Earth tides

Computation of stresses induced, on faults for example, from the tides consists of three steps: calculating the tidal forcing (the applied load), computing the response of the solid Earth to that forcing, and finally, computing the response of the solid Earth to changes in ocean water column heights induced by the tides. The tidal potential can be expressed as a function of space and time on the surface of the Earth using spherical harmonic sums where the arguments of the colatitude and longitude of both the observation point and the subbody points of the satellites of interest (e.g. the Moon, Sun, etc.). From those expressions the tidal forcing can be computed at a specified location in one of two ways. If the ephemerides of the bodies causing the forcing as a function of time are known, the tides can be computed directly. Alternatively, harmonic decompositions can be used to produce tables of amplitudes and frequencies which are valid over long periods of time. Once the tidal forcing is computed, the response of a spherical, non-rotating, elastic and isotropic Earth can be computed by scaling the solutions for quantities such as tilt and gravity on a rigid Earth by summed combinations of Love numbers. Displacements are functions of love numbers, potential, and spatial derivatives of the potential. Finally, the ocean tide contribution to the strains is found by convolving Greens functions for the Earth's response to surface loads with changes in water column height due to the tides. Such models are generally created using numerical models of water height in the open ocean and empirical models in regions of complex coastal morphology (bays, inlets, straights, etc.).

1.3 Tides and slow slip

Since transient fault slip phenomena are known to respond to small stress perturbations a number of researchers have studied the influence of the Earth tides on their occurence. However, all of these studies were conducted in subduction zone environments where shear and normal stresses from the load tides are highly correlated due to the geometry of the subducting slab and their individual effects cannot be distinguished. The San Andreas fault, in contrast, is a vertical transform fault extending from the Salton sea in southern California to the Mendocino Triple Junction in northern California and is known to host transient fault slip in its central section near the town of Parkfield, CA. The motivation to study tidal modulation of transient fault slip in Parkfield came from three different sources. First, at the time, Parkfield was the only tectonic environment of its kind known to host non-volcanic tremor and it was unknown whether tremor and slip in Parkfield was tidally correlated similar to tremor in subduction zones. While this may seem trivial, it has long been debated whether the tides have any influence on the occurence of regular earthquakes and the observation that they have substantial influence on tremor generation has implications for the mechanism responsible for generation of slow slip. Second, the geometry of the San Andreas allowed us to determine which types of stresses (normal vs. shear stresses or stressing rates) are most effective at triggering non-volcanic tremor. And third, since Parkfield is not close to the ocean, the primary source of tidal stressing comes from the body tides which are very small amplitude. It was already known that tremor were sensitive to stress changes between one and ten kilopascals but when we eventually observed a robust correlation with tidally induced shear stress, it put a new lower bound on the stress magnitude required to produce a response ($<$ 1 kPa). Chapters 2-4 are a collection of three papers that infer deep fault conditions and rheology based on obervations of the response of non-volcanic tremor and LFEs to stress changes from the solid Earth tides. The first paper, *Thomas et al.* (2009), showed that tremor in Parkfield were tidally modulated and primarily responded to shear stresses induced by the solid Earth tides. We then used a scaling relationship derived using rate-and-state friction theory to estimate the magnitude of the effective stress in the source region. This effective stress was five orders of magnitude smaller than what pressure conditions were thought to be at these depths suggesting that pore fluid pressure in the tremor source region was near-lithostatic. Chapter 3 extends the premise of the study presented in chapter 2 to a catalog of over 500,000 LFEs with the added advantage that LFEs are grouped into 88 different families based on waveform similarity. Each family is thought to represent a separate asperity on the deep fault that repeatedly fails. This is advantagous because it allows resolution of spatial variability in tidal sensitivity (*Thomas et al.*, 2012). Finally, chapter 3 uses the observations reported in *Thomas et al.* (2012) to argue that the rheology of the deep fault must be frictional and that all of the other creep mechanisms that could potentially operate at these depths cannot reproduce the observations. This fact has long been assumed in studies that model slow slip using rate and state friction however this is the first study to show that rate and state friction is the only appropriate constitutive equation.

Chapter 2

Tremor-tide correlations and near-lithostatic pore pressure on the deep San Andreas fault

2.1 Introduction

Since its initial discovery nearly a decade ago (*Obara*, 2002), non-volcanic tremor has provided information about a region of the Earth that was previously thought incapable of generating seismic radiation. A thorough explanation of the geologic process responsible for tremor generation has, however, yet to be determined. Owing to their location at the plate interface, temporal correlation with geodetically measured slow-slip events and dominant shear wave energy, tremor observations in southwest Japan have been interpreted as a superposition of many low-frequency earthquakes that represent slip on a fault surface (*Shelly et al.*, 2006, 2007a). Fluids may also be fundamental to the failure process in subduction zone environments, as teleseismic and tidal modulation of tremor in Cascadia and Japan and high Poisson ratios in both source regions are indicative of pressurized pore fluids (*Shelly et al.*, 2006; *Rubinstein et al.*, 2008; *Audet et al.*, 2009; *Nakata et al.*, 2008; *Gomberg et al.*, 2008). Here we identify a robust correlation between extremely small, tidally induced shear stress parallel to the San Andreas fault and non-volcanic tremor activity near Parkfield, California. We suggest that this tremor represents shear failure on a critically stressed fault in the presence of near-lithostatic pore pressure. There are a number of similarities between tremor in subduction zone environments, such as Cascadia and Japan, and tremor on the deep San Andreas transform (*Shelly et al.*, 2006; *Rubinstein et al.*, 2008; *Audet et al.*, 2009; *Nakata et al.*, 2008; *Gomberg et al.*, 2008; *Rogers and Dragert*, 2003; *Brenguier et al.*, 2008; *Rubinstein et al.*, 2007; *Nadeau and Guilhem*, 2009; *Nadeau and Dolenc*, 2005) suggesting that the results presented here may also be applicable in other tectonic settings.

2.2 Tidal calculations

Analysis of the response of non-volcanic tremor to small stress oscillations induced in the lithosphere by the Earths tidal deformation allows the determination of the stress orientations and magnitudes under which tremors preferentially occur, providing additional insight into the frictional processes that control tremor generation. Tidal modulation of tremor was previously established in both Japan and Cascadia (*Rubinstein et al.*, 2008; *Nakata et al.*, 2008; *Shelly et al.*, 2007b; *Lambert et al.*, 2009). The stresses induced by the ocean tides at these locations are nearly an order of magnitude larger than those near Parkfield (*Nakata et al.*, 2008; *Lambert et al.*, 2009) which primarily arise from the deformation of the solid Earth. The tidally induced stresses in the lithosphere were computed using the SPOTL code developed by D. Agnew (*Agnew*, 1997). SPOTL uses Greens functions to compute azimuthal and vertical strains that can subsequently be converted to stress. A more thorough description of the mathematical treatment of tides and code specifics can be found on the SPOTL webpage (http://www.igpp.ucsd.edu/ agnew/spotlmain.html). The results in this analysis include contributions from both the body tides, which arise due to deformation of the solid Earth, and the ocean load tides. The computation includes the semi-diurnal M2, N2, S2 and K2, and diurnal K1, O1, P1 and Q1 tidal constituents and we used the TOPEX/Poseidon global ocean tide model included in the SPOTL package to compute the load tides. Tidal model predictions were compared with strain-meter records in Pinon Flat using the perturbation matrix of ref. (*Hart et al.*, 1996), as well as previous studies to verify the calculation (*Vidale et al.*, 1998; *Hart et al.*, 1996). We compute the extensional, shear and volume strains induced by the solid Earth and ocean tides (*Agnew*, 1997) assuming a typical tremor source region depth of ∼25km (refs (*Nadeau and Guilhem*, 2009; *Shelly et al.*, 2009)).

2.3 Earthquake and tremor catalogs

We develop our analysis in parallel using a catalogue of 1,777 non-volcanic tremors detected over an eight-year period (*Nadeau and Guilhem*, 2009), a regional catalogue of earthquakes, and a catalogue of characteristically repeating micro-earthquakes located along the creeping segment of the San Andreas fault, northwest of Cholame (*Nadeau and McEvilly*, 2004) (Figure 2.1). The tremor catalogue includes a total of 1,777 events between July 2001 and May 2008 using the detection methodology described in *Nadeau and Guilhem* (2009). A small portion (5-10%) of the non-volcanic tremor occur farther north beneath Monarch Peak, but the tidally induced stresses do not vary in a significant way over such small distances, so tidal-stress time series were computed for Cholame only. The repeating earthquake catalogue contains 2,594 events between 1984 and 1999 on the 175-km creeping section of the San Andreas fault (*Nadeau and McEvilly*, 2004). The tidal stresses for this catalogue were computed at the centre of the creeping section at 5km depth. We include the repeating earthquake catalogue because it is composed of events that are all located on the creeping San

Andreas fault and might thus be expected to experience enhanced tidal triggering compared to regional catalogues (*Dieterich*, 1987). Finally, the regional earthquake catalogue consists of all earthquakes from the Advanced National Seismic System catalogue, for the same time period as the tremor catalogue, that are within 0.5° from the centre of the Cholame tremor. The same tidal time series were used for the tremor and regional earthquakes and were computed at 35.666°N, 120.2854°W. For each catalogue the fault-normal, shear, Coulomb (friction coefficient $\mu = 0.4$), and volumetric stresses and stress rates are computed for the times of each event.

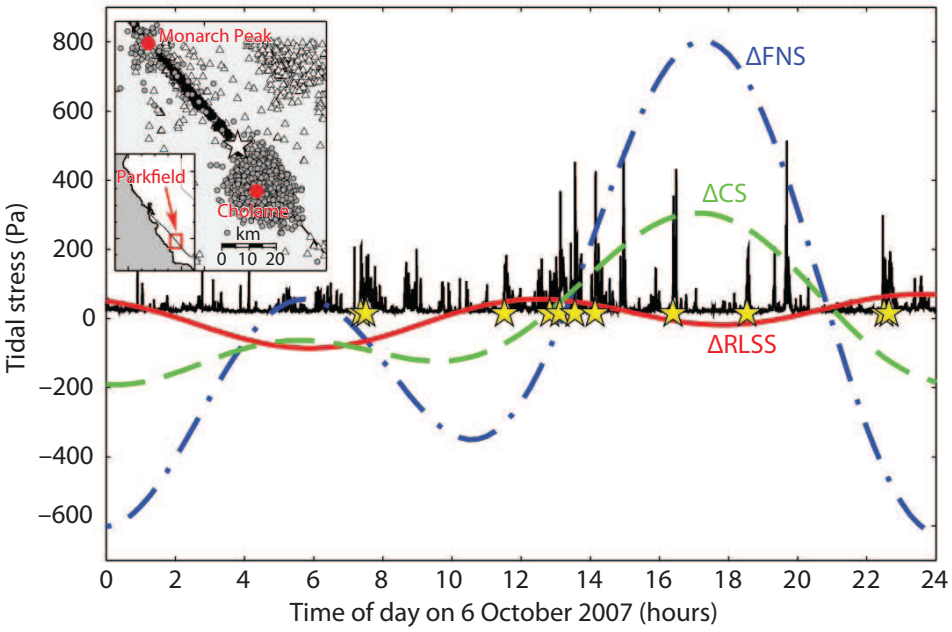

Figure 2.1: Example one-day tremor time series with superimposed tidal stresses. Black represents root-mean-square envelope of tremor activity in Cholame. Blue, red and green curves represent the tidally induced fault-normal stress (Δ FNS), right-lateral shear stress (Δ RLSS), and Coulomb stress (Δ CS) for $\mu = 0.4$. Yellow stars mark tremor start times. Some short spikes in the root-mean-square envelope are due to micro-earthquakes. The inset map shows tremor locations as grey circles, locations of regional earthquakes as white triangles, and part of the repeating earthquake catalogue as black squares. Not all repeating events are shown, because they continue further to the northwest along the creeping San Andreas section. The white star indicates the epicentre of the 2004 Parkfield earthquake.

2.4 Tidal Correlation

To investigate the influence of both the stress magnitude and rate on tremor and earthquake occurrence we divide the catalogue events into quadrants depending on the sign of the loading condition under which they occur (Figure 2.2, inset). If tremor and tides are uncorrelated, the number of events that occur under a particular tidal loading condition will be proportional to the amount of time that particular condition exists. Assuming each tremor event is independent, we use the chi-square statistic to test the null hypothesis that event times are randomly distributed with respect to tidal influence. Pearsons chi-square test is designed to test the similarity between two frequency distributions. The measure of similarity is known as the chi-squared statistic and is defined as

$$\chi^2 = \sum_{i=1}^{n} \frac{(O_i - E_i)^2}{E_i} \tag{2.1}$$

where n is the total number of potential outcomes, O_i is the observed frequency for a particular outcome i, and E_i is the expected frequency for a particular outcome. In the case of non-volcanic tremor, the total number of tremors are each assigned to one of four possible categories or quadrants (positive and decreasing, negative and decreasing, and so on) depending on the behaviour of the tidally induced stress under consideration at the time the tremor occurred. The expected number is computed by taking the entire eight-year tidal time series and determining what fraction of time was spent in each group, then multiplying by the total number of tremors in the catalogue. In this way we account for the fact that the time distribution is not equivalent between quadrants. The grey dashed line in Figure 2.2 is the critical value (99% significance level) for an upper one-sided test with three degrees of freedom.

The results for the tremor and earthquake catalogues are shown in Figure 2.2. For the tremor catalogue, the levels of correlation of the normal, shear and Coulomb stresses exceed the 99% significance level while the correlation levels for the other catalogues are statistically insignificant. The lack of correlation in the regional and repeating earthquake catalogues is not surprising given the size of the catalogues and results from previous efforts to establish a significant tidal triggering of earthquakes(*Lockner and Beeler*, 1999; *Beeler and Lockner*, 2003; *Vidale et al.*, 1998).

We further explore the apparent correlation between tremor and tidally induced stresses by comparing tremor times with the loading conditions under which they occur. Figure 2.3 shows tremor rate distributions with respect to tidally induced shear, normal and Coulomb stress magnitudes and rates at the time of the events. Correlation between tremor occurrence and tidal stressing rate is insignificant for all stress components. Induced right-lateral shear stresses (ΔRLSS) demonstrates the most compelling correlation, with distinct increases in tremor activity that correspond to positive (right-lateral) shear stresses parallel to the San Andreas fault and equally apparent decreases when values are negative. Additionally, the tremor surpluses and deficits become more pronounced as Δ RLSS increases to values of $\pm$

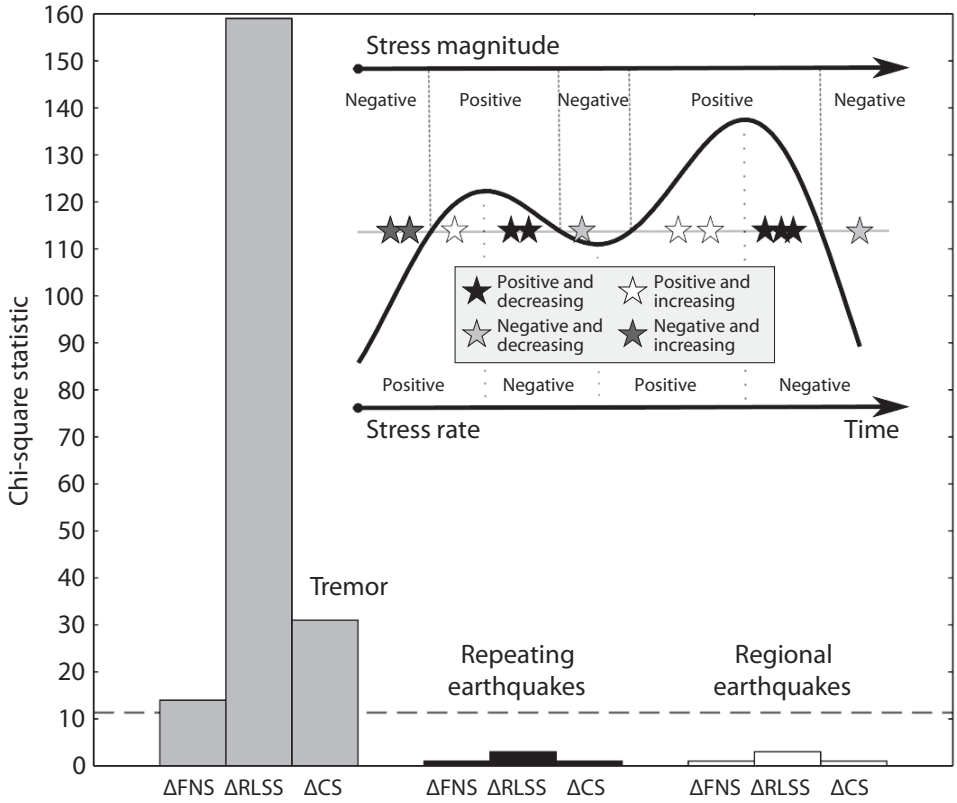

Figure 2.2: Results of chi-square significance tests. The chi-square test results correlate the tremor, regional and repeating earthquake catalogues with tidally induced FNS, RLSS, and CS. The dashed line shows the 99% confidence level, where larger values indicate that the hypothesis of random event occurrence can be rejected. The inset shows how tremor start times were separated into four quadrants based on both the magnitude and rate of change of the stresses.

150Pa. Although fault-normal stress changes (ΔFNS) are much larger, they only exhibit a weak correlation at large, positive (tensile) values of $> 1,000$Pa. Coulomb stresses ($\Delta\text{CS} = \mu\Delta\text{FNS}+\Delta\text{RLSS}$, $\mu = 0.4$) exhibit less correlation than the shear stress alone.

Two-standard-deviation error estimates in Figure 2.3 are determined using a bootstrap method. The method randomly selects an individual tremor from the original tremor catalogue of 1,777 tremors. This process is repeated 1,777 times to yield a randomly sampled catalogue (with replacement) of 1,777 events. The above process is repeated 50 times, giving 50 randomly sampled versions of the original catalogue. The tremor rate distributions as a function of the tidally induced stresses are then calculated for each of the 50 randomly sampled catalogues. For each stress bin, the standard deviation of tremor rates of the 50 catalogue values are then computed and multiplied by 2, giving the 2 rate uncertainties

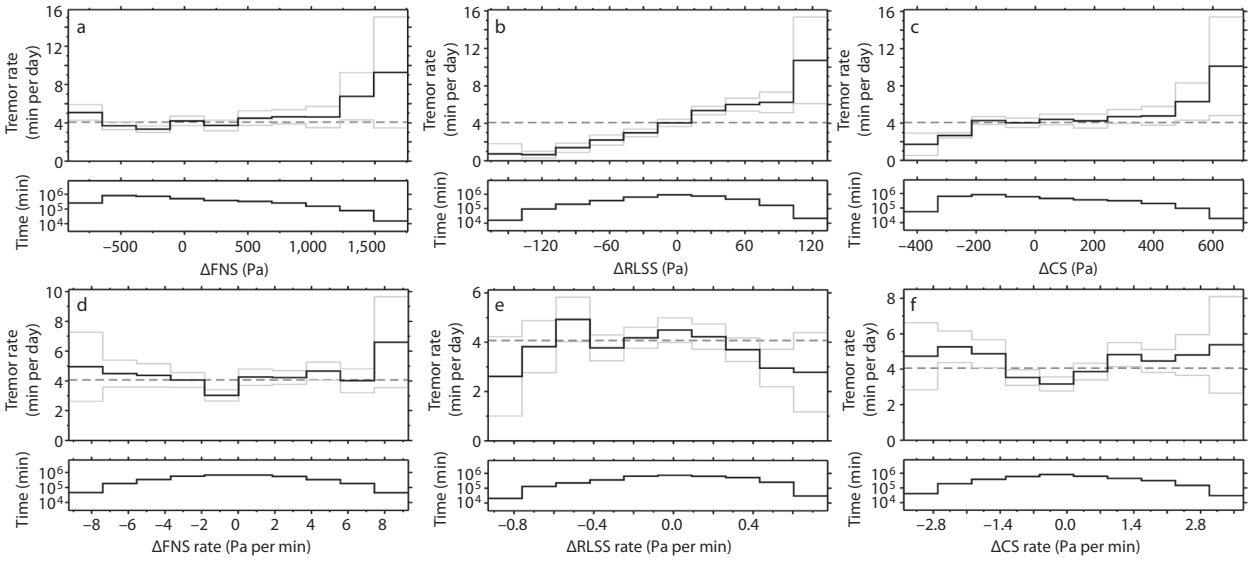

Figure 2.3: Tidal stress magnitude (panels a, b and c) and rate (panels d, e and f) distributions for the ΔFNS, ΔRLSS and ΔCS ($\mu = 0.4$). Volumetric stresses are not shown because they are strongly coupled with normal stresses. Solid black lines show tremor rates computed by dividing the number of tremors within the respective stress interval by the total amount of time spent in that interval. The time distribution for each bin is shown below each histogram. The average tremor rate (dashed line) corresponds to the rate expected if there were no correlation between tremor and tides. Grey lines are 2σ error bars.

for each bin that are shown by the grey bars in Figure 2.3. Tremor rate errors arise from variability in tremor detection sensitivity. More details on the detection methodology can be found in *Nadeau and Guilhem* (2009).

2.5 Optimal friction coefficient

Assuming a frictional Coulomb failure process is an appropriate model for non-volcanic tremor, the optimal friction coefficient μ is the value that maximizes the number of events that occur during times of encouraged failure stress (Figure 2.4). Tremors show a marked increase for friction values of $\mu < 0.1$ with a peak of over 31% above the long-term average number of events (excess) for $\mu = 0.02$. The percentage excess for both the regional and repeating earthquake catalogues does not exceed 6%. This demonstrates that tidally induced shear stress parallel to the San Andreas fault, although of much smaller magnitude than normal stress changes, has the most robust correlation with non-volcanic tremor near Parkfield. The dominant role of small shear stress perturbations in stimulating the tremor, despite much larger normal stress perturbations, is indicative of a very weak fault zone with

low effective normal stress, probably due to near-lithostatic pore pressures at the depth of the tremor source region. As a test of our assumption of San Andreas fault alignment in the stress calculations, we perform the same analysis to determine the percentage excess tremor with respect to a range of vertical fault plane azimuths (Figure 2.4, inset). The peak percentage excess occurs at N44°W, nearly parallel to the local strike of the San Andreas fault (N45°W). This result serves as an independent piece of evidence to show that tremor represents a mode of fault-parallel shear failure in the lower crust.

2.6 Near-lithostatic pore fluid pressure

If non-volcanic tremor simply represents a different class of earthquakes that still involves failure on a fault surface (*Shelly et al.*, 2007b; *Ide et al.*, 2007) it is unclear why tremor is modulated by tides but regional earthquakes are not. Careful statistical analyses of tidal influence on earthquake populations find the correlation to be extremely weak ($\sim 13,000$ events are needed to establish a 1% increase)(*Lockner and Beeler*, 1999; *Beeler and Lockner*, 2003; *Vidale et al.*, 1998; *Cochran et al.*, 2004). *Lockner and Beeler* (1999) and *Beeler and Lockner* (2003) conducted a series of laboratory tests simulating tidal loading conditions on active faults and found that the absence of strong tidal triggering can be reconciled with rate-state frictional models that involve delayed slip nucleation (for example, by time-dependent failure or static fatigue). If tremor can also be described in a rate-state friction framework then we can derive a quantitative estimate of effective normal stress in the tremor source region from the observed tidal correlations (*Dieterich*, 1987). *Dieterich* (1987) found a simple scaling relationship between earthquake rate fluctuations and the amplitude of the periodic shear stress divided by the normal stress:

$$\sigma = \frac{2\Delta\tau}{aR_a} \tag{2.2}$$

where R_a is the total rate variation divided by the average rate, $R_a = (R_{max} - R_{min})/R_{avg}$, σ is the effective normal stress, $\Delta\tau$ is the amplitude of the tidally induced shear stress, and a is the rate constitutive parameter. Using the maximum and minimum rates for $\mu = 0.02$, the value of friction that maximizes the percentage excess, a stressing amplitude of 177Pa (the maximum value of the tidally induced shear stress) and experimentally derived values of 0.005 to 0.02 for the fault constitutive parameter a (*Blanpied et al.*, 1995), we find effective normal stresses of 0.035 to 0.009MPa. These values are orders of magnitude lower than the lithostatic overburden pressure at this depth (∼700MPa), suggesting that effectively lithostatic pore fluids are present in the tremor source region. Additionally, this estimate is consistent with the low friction coefficient reflected in the lack of correlation with larger normal stress fluctuations. Potential sources of fluids at mid-crustal depths beneath the San Andreas fault are less well documented than slab dehydration in subduction zones, but previous studies have suggested the presence of fluids and processes to explain their introduction(*Becken et al.*, 2008).

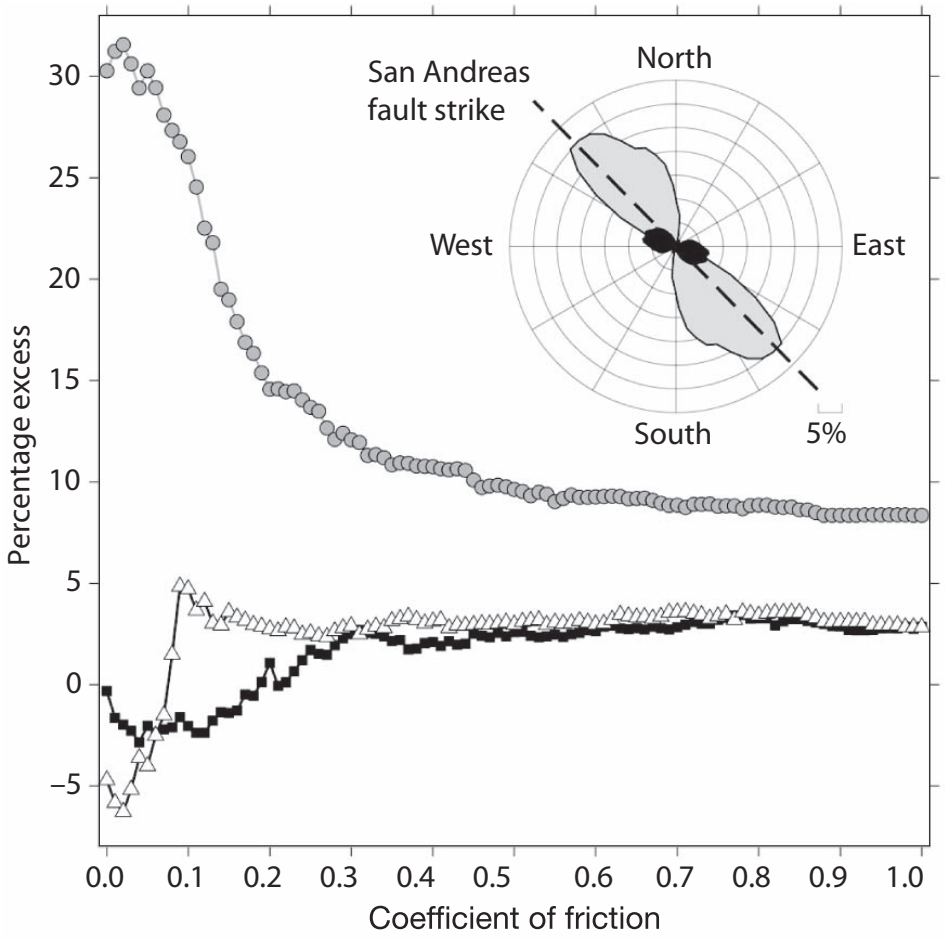

Figure 2.4: Percentage of excess events (that is, above long-term average) during times of positive CS versus effective coefficient of friction. Values for the tremor, regional and repeating earthquake catalogues are shown as grey circles, white triangles and black squares respectively. Standard deviations (2σ) were computed using a bootstrap procedure on each friction value for each catalogue. Maximum 2σ errors over all possible friction values are 5.66%, 5.80% and 4.66% for the tremor, regional and repeating earthquake catalogues respectively. The inset displays the positive percentage excess tremor for ΔFNS (black) and ΔRLSS (grey) as a function of the fault azimuth.

The similarities (or differences) in non-volcanic tremor properties with respect to tectonic environment warrant further discussion. *Nakata et al.* (2008) suggest correlation with ΔCS (assuming $\mu = 0.2$) and ΔCS rate in Shikoku, Japan, while *Lambert et al.* (2009) find that peak tremor activity occurs at times of maximum tidal shear stress in the thrust direction and with ΔCS (assuming $\mu = 0.4$) in Cascadia. One possible reason for the different results is that both in Japan (R. Nakata, personal communication, 2009) and Cascadia (*Lambert et al.*, 2009) times of increased shear stress are highly correlated with compressive (clamping) normal stresses of comparable magnitude. This makes it difficult to separate the individual contributions of the normal and shear stresses, especially for the short time periods (a few weeks) considered by these two studies. The results for Parkfield are not subject to this limitation and we find that very small shear stresses, but not the larger normal stress changes, modulate tremor. It is likely that tremor modulation is affected by frictional strength, the relative magnitude of tectonic and tidal loading rates (*Lockner and Beeler*, 1999; *Beeler and Lockner*, 2003), material properties (*Audet et al.*, 2009), and other factors that vary with respect to tectonic environment. One finding common to all three localities is that tremor appears to be associated with the presence of fluids at near-lithostatic pressures, and given similar observations in variable tectonic environments (*Shelly et al.*, 2006; *Rubinstein et al.*, 2008; *Audet et al.*, 2009; *Nakata et al.*, 2008), the same mechanism is probably responsible for non-volcanic tremor elsewhere.

2.7 Conclusion

We find that tremor occurs preferentially when subjected to tidal shear stresses that promote right-lateral failure along the San Andreas fault, very small stress perturbations from solid-Earth tides are responsible for significant tremor rate increases, and extremely low effective normal stress in the tremor source region is required to explain the apparent tidal triggering. Tremor appears to be shear failure capable of producing seismic radiation, so a brittle failure model seems appropriate. These results present a rheological paradox, because ductile rheologies, which may be expected at depths of more than 20km and temperatures over 500°C, generally have no normal-stress dependence. It is possible that very high fluid pressures on discrete fault patches facilitate slip in an otherwise ductile-deforming regime. Coupling these observations with the location of the tremor on deep, roughly planar zones(*Shelly et al.*, 2009), we favour the conjecture that tremor at Cholame represents shear failure within a weak, critically stressed San Andreas fault zone extending to the base of the crust. Finally, given that earthquakes and non-volcanic tremor are both manifestations of slip on a fault surface, further constraining the properties and processes that control tremor generation may facilitate a better understanding of fault mechanics, lithospheric structure and tectonic deformation in the deep crust.

Chapter 3

Tidal triggering of low frequency earthquakes near Parkfield, CA

3.1 Introduction

Large slow-slip events in deep subduction zone environments are recorded geodetically, as periodic transient reversals of long term GPS velocities or tilt measurements, and seismically, as long duration, low frequency seismic signals, dubbed non-volcanic tremor (NVT) due to their similarity to volcanic tremor (*Obara*, 2002). Though slow-slip and NVT occur simultaneously, inversions of GPS displacements during slip events in the Cascadia subduction zone result in strain release equivalent to M_w ~6 events (*Schmidt and Gao*, 2010), while the total seismic moment of NVT are orders of magnitude smaller (*Kao et al.*, 2010). Slip and tremor in subduction zone environments reflect slow-slip events (SSEs) that propagate along the subduction interface at velocities of ~10 km/day and are largely confined to the region downdip of the locked subduction thrust (*Obara et al.*, 2004; *Dragert et al.*, 2004). As these SSEs propagate, small on-fault asperities capable of generating seismic radiation fail in earthquake-like events or low-frequency earthquakes (LFEs). The collocated, coeval evolution of NVT, SSEs, and LFEs led *Shelly et al.* (2007a) to suggest that part if not all of the seismic signature of NVT could represent a superposition of multiple LFEs. Focal mechanism inversions of LFEs in Shikoku indicate that LFEs are a manifestation of shear slip located largely on the plate boundary (*Ide et al.*, 2007); however other studies have reported intraplate NVT locations which may suggest they can take place on any localized slip surface if source region conditions are agreeable (*Kao et al.*, 2005). Application of matched filter techniques to other subduction zones and tremor on the deep San Andreas fault (SAF) indicate that global observations of NVT can be explained as a superposition of many LFEs (*Shelly et al.*, 2007a; *Brown et al.*, 2009; *Shelly and Hardebeck*, 2010). The similarities between LFEs in different tectonic settings suggests that the same slip phenomena that take place in subduction zone environments such as Cascadia and Shikoku may also occur on transform systems such as the SAF.

In idealized models of deformation in fault zones, slip is accommodated in one of two ways: seismically, in earthquakes that occur in the shallow, brittle regions of the crust, or aseismically, in deep shear zones where pressure and temperature conditions are more amenable to ductile deformation. Shallow aseismic slip also occurs on some faults, however the mechanisms for this shallow creep may not be the same as those in deep faults (*Marone*, 1998). The identification of highly episodic, non-volcanic tremor and slow slip below the seismogenic zone (*Hirose et al.*, 1999; *Dragert et al.*, 2001; *Obara*, 2002; *Miller et al.*, 2002) has modified our notion of seismic coupling and the relative partitioning between seismic and aseismic deformation. While aseismic slip is not explicitly hazardous there are implicit or indirect implications for hazard; deformation in deep fault zones transfers stress to shallow faults where large, devastating earthquakes can occur. Since shallow and deep slip are potentially related, developing a comprehensive understanding of fault zone anatomy, meaning where and how different slip mechanisms operate, the physics that governs deformation style, and stress transfer between the deep and shallow crust may mitigate seismic hazard.

One characteristic common to global observations of NVT and LFEs is extreme sensitivity to small stress perturbations. Studies of static stress changes from regional earthquakes report both an aftershock-like response of deep NVT on the SAF to increases of 6 and 10 kPa in shear stress from the 2003 M_w 6.5 San Simeon and the 2004 M_w 6.0 Parkfield earthquakes respectively, and quiescent response to decreases in failure stress (*Nadeau and Guilhem*, 2009; *Shelly and Johnson*, 2011). Several studies report triggering of NVT by teleseismic surface and body waves that imposed stress transients as small as a few kilopascals (*Gomberg et al.*, 2008; *Miyazawa and Brodsky*, 2008; *Peng et al.*, 2009; *Hill*, 2010; *Ghosh et al.*, 2009; *Shelly et al.*, 2011). Additionally, studies of tidal stress perturbations conclude that NVT are sensitive to stress changes as small as fractions of a kilopascal (*Rubinstein et al.*, 2008; *Nakata et al.*, 2008; *Lambert et al.*, 2009; *Thomas et al.*, 2009; *Hawthorne and Rubin*, 2010). While these stress changes are exceedingly small, a number of other geological phenomena including volcanoes, landslides, and glaciers are influenced by kPa-level stress changes caused by the tides (*McNutt and Beavan*, 1984; *Schulz et al.*, 2009; *de Juan et al.*, 2010).

Early investigations of tidal triggering of earthquakes find no relationship between earthquakes and tidal forcing (*Heaton*, 1982; *Vidale et al.*, 1998). *Lockner and Beeler* (1999) and *Beeler and Lockner* (2003) used laboratory friction experiments and rate and state dependent friction theory to argue tides and earthquakes are correlated but catalogs with large event numbers are required to detect a very modest correlation and the degree of correlation increases as the ratio of the amplitude of the tidal shear stress to the effective confining stress increases. A number of later studies substantiate the latter point, most notably *Cochran et al.* (2004) find a robust correlation between tidal stress and earthquakes in shallow subduction environments (i.e. where the ocean tidal loads can be as large as 10 kPa and the confining stress is relatively low). High fluid pressures in both Nankai and Cascadia are inferred from the high V_p/V_s ratios in the NVT source region documented by *Shelly et al.* (2006) and *Audet et al.* (2009) which may explain the robust correlation of NVT to small stress perturbations. *Thomas et al.* (2009) show that NVT rates on the Parkfield section of the SAF vary substantially in response to small fault-parallel shear stresses induced by the

solid Earth tides and were only modestly influenced by the much larger fault-normal and confining stress cycles. *Thomas et al.* (2009) appeal to the presence of pressurized pore fluids in the NVT source region to explain their observations. They calculated effective normal stresses between 1 and 10 kPa suggesting that pore fluid pressures in the NVT source region are very near lithostatic.

In this study we use the response of LFEs near Parkfield to tidally induced stress perturbations to infer mechanical properties of the LFE source region on the deep SAF. Previous studies of tidal modulation of NVT in Parkfield used start times and durations of NVT events in the catalog described by (*Nadeau and Guilhem*, 2009). The present study utilizes the added spatial and temporal resolution gained in using matched filter and stacking techniques to identify and locate LFE families (*Shelly and Hardebeck*, 2010) to map the spatial variability of sensitivity to tidally induced stresses and effective stress. We present observations of the tidal influence on slip on the central SAF, inferences about properties of the LFE source region informed by those observations, and when possible, comparisons between our findings and relevant observations in other tectonic environments.

3.2 Data and Methods

Low Frequency Earthquake Catalog

The 2001-January 2010 low-frequency earthquake catalog of *Shelly and Hardebeck* (2010) is composed of ∼550,000 LFEs grouped into 88 different families based on waveform similarity. Locations of LFE families in Parkfield are tightly constrained by numerous P- and S-wave arrival times at densely distributed stations. The location procedure involves visually identifying individual LFE template event candidates and then cross-correlating and stacking those waveforms with continuous seismic data to detect other LFEs in the same family. The most similar events are stacked at all regional stations, and P- and S-wave arrivals are identified on these stacked waveforms. LFEs are located by minimizing travel time residuals in the 3D velocity model of *Thurber et al.* (2006) with estimated location uncertainties of 1-2 km (for further details see *Shelly and Hardebeck* (2010)). Hypocenters of LFE families, shown in Figure 3.1, are distributed along ∼150 km of the SAF from Bitterwater to south of Cholame. Estimated source depths extend from just below the base of the seismogenic zone to the Moho (16-30 km depth) on the deep extension of the SAF, a zone previously thought incapable of radiating seismic waves.

Locations separate into two distinct groups: one to the northwest below the creeping section of the SAF, and one extending to the southeast from below the rupture area of the 2004 M_w 6.0 earthquake into the locked section of the fault that last ruptured in the 1857 Fort Tejon earthquake. These groups are separated by a 15 km gap beneath the town of Parkfield, where no tremor has yet been detected. The presence of a gap in the locations is not a product of station coverage or the location procedure. Very low tremor amplitudes on each side of this gap suggest that tremor amplitudes in this zone may simply fall below

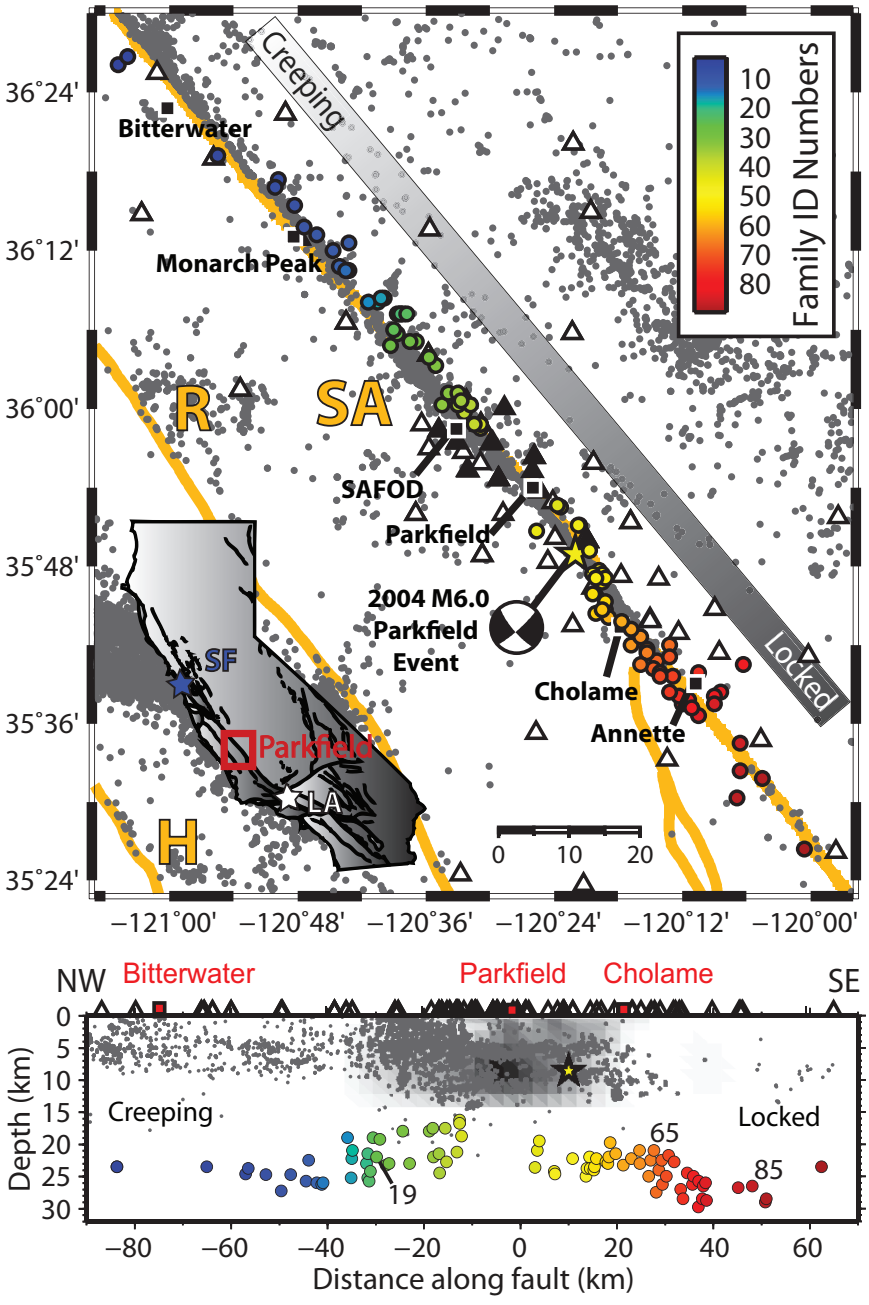
Creeping
Locked
Family ID Numbers
10
20
30
40
50
60
70
80
Bitterwater
Monarch Peak
SAFOD
Parkfield
2004 M6.0
Parkfield
Event
Cholame
Annette
SF
Parkfield
LA
R
SA
H
0
10
20
36°24'
36°12'
36°00'
35°48'
35°36'
35°24'
−121°00'
−120°48'
−120°36'
−120°24'
−120°12'
−120°00'
NW
Bitterwater
Parkfield
Cholame
SE
Depth (km)
0
5
10
15
20
25
30
Creeping
Locked
19
65
85
−80
−60
−40
−20
0
20
40
60
Distance along fault (km)

Figure 3.1: Top panel: Parkfield area location map with LFE locations are plotted as circles color-coded by family ID numbers organized from northwest to southeast along the fault. Relocated earthquakes (post 2001) from the catalog of *Waldhauser and Schaff* (2008) are shown as gray dots. The Hosgri (H), Rinconada (R), and San Andreas (SA) faults are shown in orange. Surface seismic stations used for detection and borehole stations used for location are shown by white and black triangles respectively. The September 28, 2004 M_w 6.0 Parkfield earthquake epicenter is indicated by the yellow star. Inset map shows area of map view marked in red and locations of San Francisco (SF) and Los Angeles (LA). Bottom panel: along fault cross section of the San Andreas viewed from the southwest (vertical exaggeration is 4:3) showing locations of LFE families shown in top panel and color coded by their family ID number. Families that are highlighted in the text are labeled by their ID numbers. Relocated earthquakes shown in top panel within 10 km of the fault are plotted as gray dots. The slip distribution of the 2004 M6.0 Parkfield earthquake from *Murray and Langbein* (2006) is shown in shades of gray. Stations shown in top panel and relevant landmarks are indicated by triangles and red squares respectively.

current detection thresholds (*Shelly and Hardebeck*, 2010).

Tremor amplitudes (maximum recorded ground velocities) and recurrence patterns vary considerably, and semi-coherently, along fault strike and with depth. The strongest tremor is consistently generated along a ∼25 km section of the fault south of Parkfield, near Cholame (*Shelly and Hardebeck*, 2010). Activity in some families is highly episodic, with episodes of very high activity concentrated within a few days, followed by 2-4 months of quiescence. An example of highly episodic behavior is shown in Figure 3.2, family 65, where individual slip events can host over 200 LFEs in a five day period. These punctuated episodes concentrate in several relatively shallow neighboring families whereas the deepest families (e.g. family 85 in Figure 3.2) recur frequently, with small episodes of activity as often as every 2 days with few intermittent periods of increased activity (*Shelly and Johnson*, 2011).

Oftentimes adjacent or nearby LFE families have nearly identical event histories suggesting that they fail together and experience very similar stressing histories. Neighboring, highly-episodic families generally produce bursts of activity almost simultaneously (*Shelly et al.*, 2009). In Parkfield, this observation is most robust in the shallowest families; however there is also evidence for interaction in deeper families that still occur episodically. If LFE recurrences track the rate of dominantly aseismic fault slip, then these episodes likely represent propagating slip fronts, analogous to slow slip events in subduction zone settings. No geodetic manifestation of deep slow slip episodes has yet been observed in Parkfield, and slow slip events on the deep San Andreas probably produce surface deformation that falls below the detection threshold for borehole strain, GPS or laser strainmeter instrumentation (*Smith and Gomberg*, 2009).

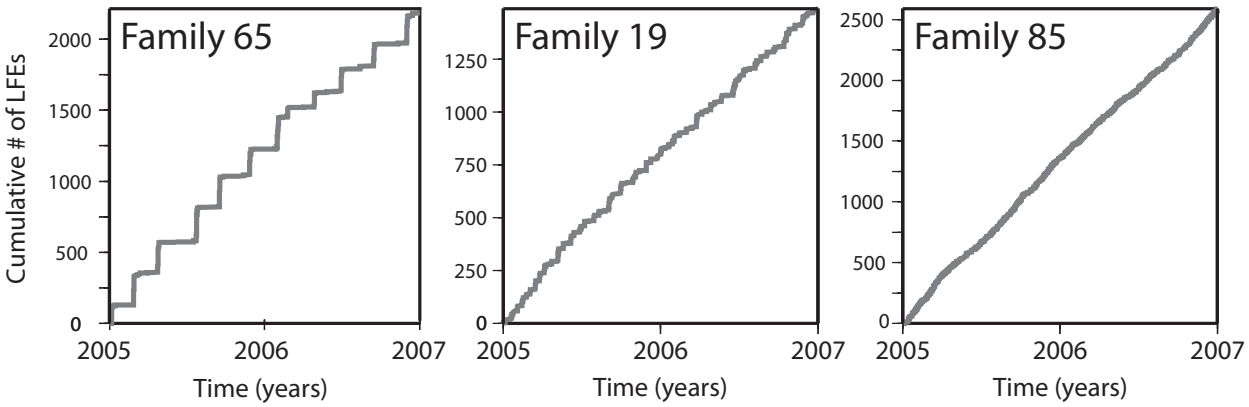

Figure 3.2: Example timeseries of cumulative number of LFEs over a two year time period for three LFE families (65, 19, and 85, see Figure 3.1 for locations in cross section). Family 65 is highly episodic with 2-4 month quiescent periods punctuated by few-day periods with extremely high LFE rates. In contrast, family 85 recurs frequently, with a general absence of quiescence and a few intermittent episodes of much smaller magnitude than family 65. Family 19 is an example of transitional behavior between the two end member cases.

Tidal Model

We compute tidally-induced strains at the centroid of the tremor source region (-120.525, 35.935, 25 km depth) using the tidal loading package Some Programs for Ocean Tide Loading, which considers both solid Earth and ocean load tides (*Agnew*, 1997). For the solid Earth contribution, displacements are very long wavelength compared to the source region depth, thus we assume that the strains modeled at the surface are not significantly different from those at 25 km depth. Unlike the body tides, the strain field computed at the surface cannot be applied at depth, as the magnitude of the ocean loading component may change significantly between the surface and 25 km. To resolve this potential issue, we calculate depth dependent, spherical Green's functions using a finite element model of the layered Earth model of *Harkrider* (1970) which we then use to compute the strains from only the ocean loading component at depth. A comparison of the load tides reveals that there are small amplitude and phase shifts between the load tides at zero and 25 km depth. However, once the load tides are superimposed on the solid Earth tides, which are roughly an order of magnitude larger, the differences between the two become negligibly different.

Given the degree two pattern of the tides, we assume that tidal stress changes are small over the $\sim$140 km section of the SAF under consideration and that a single tidal time series computed at the centroid of the LFE source region can be applied to all 88 hypocentral locations. To validate this assumption, we computed and compared volumetric strain timeseries at the center and ends of the LFE source region and found that the difference between the two time series has average and maximum values of 1% and 5% respectively.

We compute the shear and normal stresses on the SAF by converting strain to stress using a linear elastic constitutive equation and resolving those stresses onto a vertical plane striking N42°W. The relevant elastic parameters were chosen to be equivalent to those in the top layer of the continental shield model of (*Harkrider*, 1970). A representative 14-day time series of the fault-normal and right-lateral shear stresses, FNS and RLSS respectively, are shown in Figure 3.3. The vast majority of the stress amplitudes are due to only the body tides, as the ocean loading contribution diminishes with distance inland. The solid Earth tides induce largely volumetric stresses thus the resulting shear stress on the SAF is approximately an order of magnitude smaller than the normal stress. We also note that while the shear and normal stress components are due to a common forcing function, they are not directly correlated (see Section 2.4).

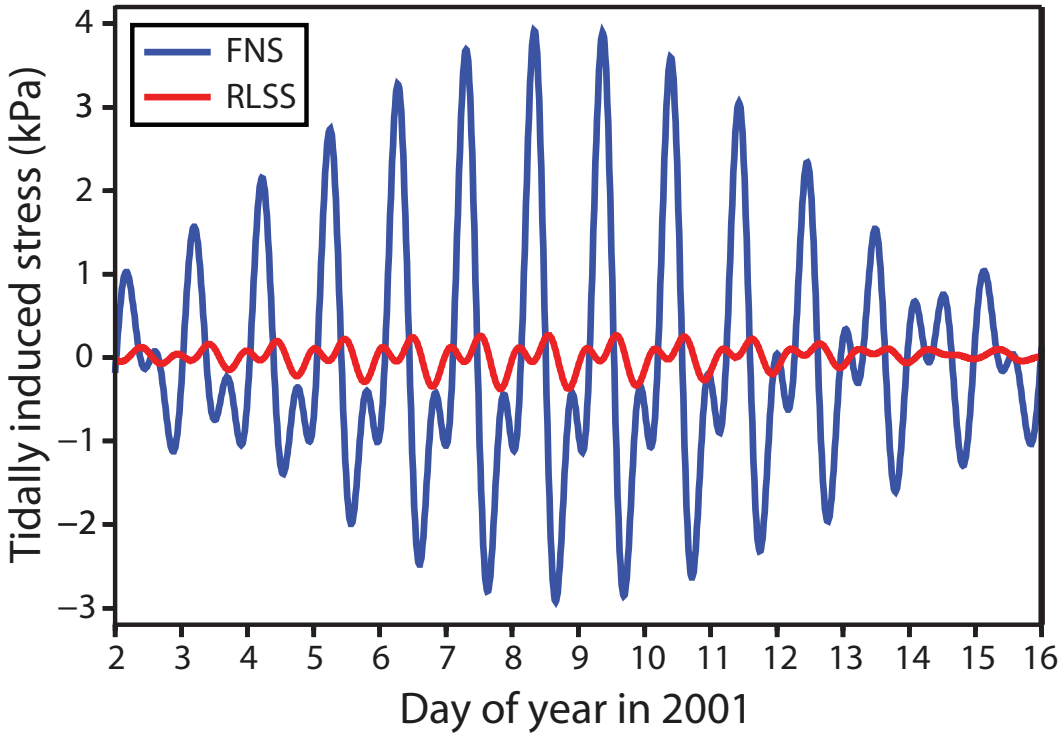

Figure 3.3: A representative 14 day time series of tidally induced shear (red) and normal (blue) stresses resolved onto the SAF striking N42°W.

LFE Correlation with Tidal Stress

For each LFE we can compute the tidally induced stresses at the time of the event, as event durations of ∼10 s are short relative to tidal periods (*Shelly and Hardebeck*, 2010). To quantify the overall correlation with tidal loading, we first define the"expected number of events",

or the number of events that occur under a particular loading condition assuming that LFEs occurrence times are randomly distributed with respect to the time. The degree of correlation is defined by the percent excess value (N_{ex}) defined as the difference between the actual and expected number of events divided by the expected number of events (*Cochran et al.*, 2004; *Thomas et al.*, 2009). Positive N_{ex} values indicate a surplus of events and negative values, a deficit. Loading condition can refer to the sign of a given stress component or to a particular stress-magnitude range. The load components we consider for the remainder of this manuscript are the tidally induced fault normal stress (FNS), fault normal stress rate (dFNS), right-lateral shear stress (RLSS), and right-lateral shear stress rate (dRLSS). We compute N_{ex} values for all families relative to the sign of FNS, RLSS, dFNS, and dRLSS (shown in Figure 3.4). N_{ex} values corresponding to 99% confidence intervals are indicated in the lower left of each panel in Figure 3.4. Confidence intervals are computed by randomly selecting N times (where N corresponds to the number of LFEs in an LFE family) from the tidal timeseries to represent times of LFEs making up a synthetic catalog. FNS, RLSS, dFNS, and dRLSS N_{ex} values are then computed from the synthetically generated catalog. This process is repeated 25,000 times to construct N_{ex} distributions for each of the four stress components, which are then used to construct the two-sided 95% and 99% confidence intervals. The values reported at the 99% confidence intervals in Figure 3.4 correspond to the LFE family with the fewest number of LFEs. N_{ex} values different from zero by more than the 99% confidence level are less than 1% likely to occur by random chance assuming that tides and LFEs are not correlated.

Hypothesis Testing for Spurious Correlations

One caveat of the aforementioned analysis is that each of the tidally induced stresses and stressing rates observed arises from a common forcing and thus they are inevitably related to one another (non-zero mutual information). However, the relationship between components cannot be characterized as a simple phase shift or amplitude scaling (Figure 3.3). Before interpreting the observed LFE sensitivities to tidal stress components we first address the potential for spurious correlations that have no physical meaning to arise due to the inherent correlation of the stressing functions. Artifacts can arise when one tidal component induces LFE occurrence due to some physical process and a second tidal component, which has no effect on LFE occurrence, is correlated with the first. In our interpretation of correlations of LFE timing to tidal stresses, we want to avoid interpreting spurious correlations in light of physical processes, which requires determining the sensitivity of tidal stressing components to one another.

To test for spurious correlations, we use a bootstrap methodology to generate a large number of synthetic LFE catalogs based on the observed distribution of LFEs relative to a particular primary stressing function. These synthetic catalogs are then used to calculate confidence intervals for the expected N_{ex} values of the secondary stressing functions. To construct synthetic catalogs, we consider one stressing function (or null hypothesis) and one LFE family at a time. Instead of assuming LFEs are randomly distributed with respect to

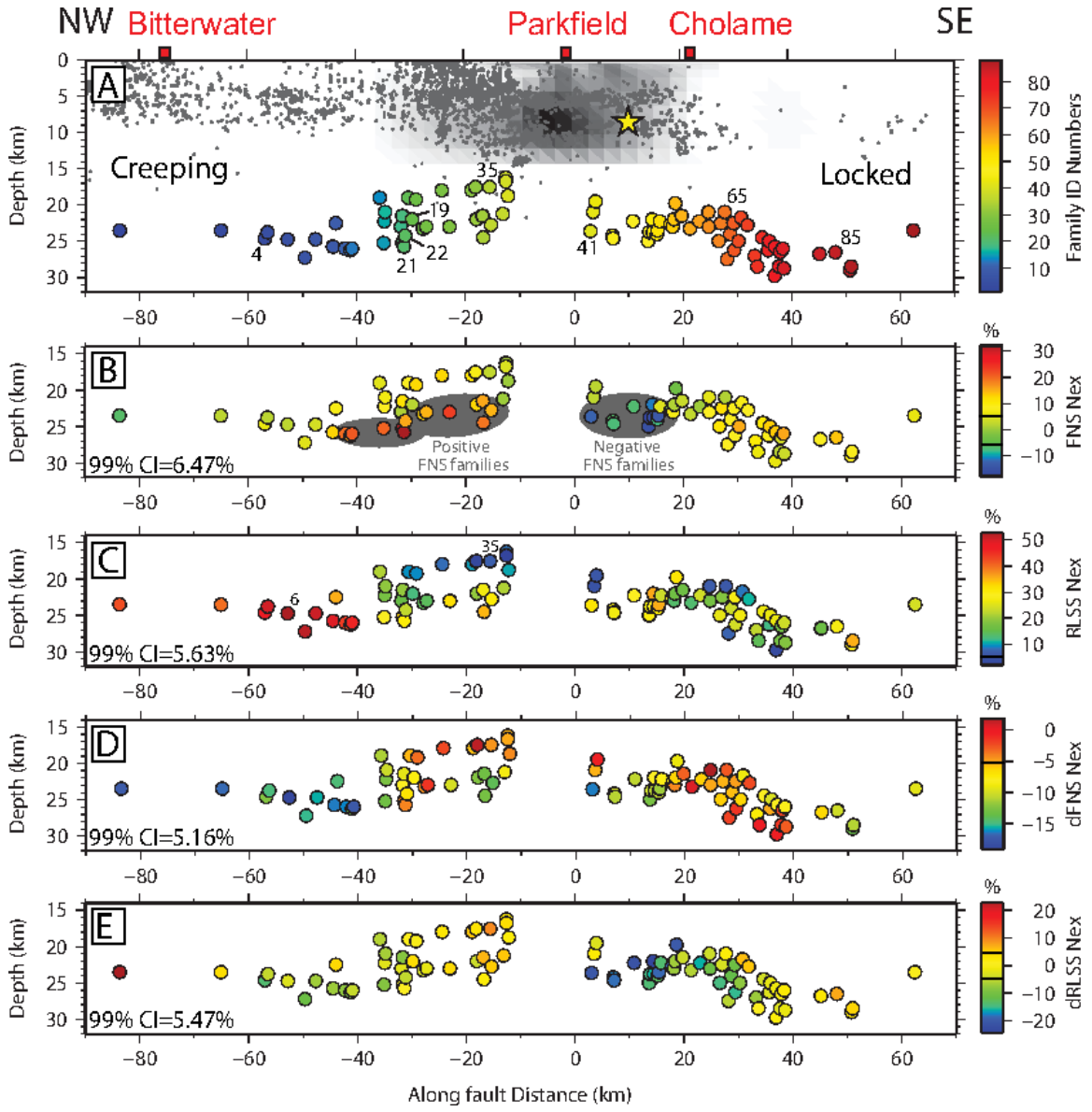

Figure 3.4: NW-SE cross-section of LFE locations together with shallow microseismicity and slip distribution of the 2004 Parkfield earthquake from *Murray and Langbein* (2006). Panels B-E show the locations of LFEs color-coded by the N_{ex} values corresponding to the tidal FNS, RLSS, dFNS, and dRLSS components calculated for the average fault strike of N42°W. 99% confidence intervals calculated for the family with the fewest events (largest uncertainty) are reported in the bottom left of each panel.

time as in the N_{ex} calculation, we assume (1) they are distributed in the way we observe for that particular component and (2) they are randomly distributed with respect to all other components. To construct the synthetic catalogs, we use the frequency distribution of LFEs relative to the primary stressing function, so each bin represents some range of stress and has a corresponding number of LFEs. For each bin, we randomly select an equal number of times out of the tidal timeseries that have stress values within the corresponding stress interval meant to represent times of LFEs in the synthetic catalog. We then compute the N_{ex} values for each of the secondary stressing functions based on this synthetic catalog of LFEs. We repeat this procedure 1000 times and use the resulting values to construct 95% and 99% confidence intervals. Finally, these confidence intervals are compared to the observed N_{ex} values for the secondary components.

Models of frictional strength of faults depend on more than a single loading function, for example Coulomb failure strength is a function of both shear and normal stress. To test for this type of dependence, we also explore distributing synthetic catalog events randomly with respect to two different primary stressing components for a total of eleven different null hypotheses: one considering no correlation between LFEs and tides, four for each stressing component, and six for all possible combinations of two stressing components. The two component case is implemented with the same procedure as described above, except events are distributed relative to the joint frequency distributions of the two components. To quantify how well the null hypotheses characterize the remaining components, we define a misfit by determining the average number of standard deviations between the observed N_{ex} and 50th percentile of the synthetically derived N_{ex} values. For each family, the null hypothesis that best characterizes the event times of that family is the one with the smallest misfit.

3.3 Results

Spatial Distribution of Sensitivity of LFEs to Tidal Stresses

Since each family has more than 2,000 LFEs, we can calculate their sensitivity to tidal stresses at each location, which allows for a detailed view of the variability of tidal correlation with distance along the fault and depth. Figure 3.4 shows the along-fault cross sections of the locations of the 88 LFE families identified by *Shelly and Hardebeck* (2010) viewed from the southwest. Each family is color-coded by its sensitivity to the respective stressing condition (N_{ex} value). Sensitivities to all stressing components vary in a spatially coherent way, with nearby families often having similar triggering characteristics, along both strike and dip. To the northwest, within the creeping segment of the San Andreas, all but families 1 and 2 are either uncorrelated with the FNS or correlate with tensile FNS at a significance level of 99% or greater (panel B). The families with the highest FNS N_{ex} values are the deepest families that locate between -15 and -45 km along-fault distance from Parkfield (labeled Positive FNS families in Figure 3.4). The majority of families to the southeast of

Parkfield are either not significantly correlated with the FNS or correlate in a less robust way than the highly correlated families within the creeping section (10% vs. 30% N_{ex}). The notable exception to the overall correlation with tensile FNS is the localized group of families characterized by negative FNS N_{ex} values located along a 15 km-long stretch of fault beneath Parkfield. The results of the statistical analysis presented in the next section indicate that the correlation with clamping is authentic as none of the null hypotheses are capable of explaining the observed deviation from zero as being due to inherent correlations with other stress components (see families 45-52 in Figure 3.5). These events are located along a releasing right bend of the SAF and variation in fault orientation provides a potential explanation for this correlation with clamping, which we discuss in Section 4.6 (*Shelly and Hardebeck*, 2010).

Correlation with positive, right-lateral shear stress (Figure 3.4C), is ubiquitous with all families correlating with shear stresses, which are an order of magnitude smaller than associated normal stresses, at a confidence level of 99% or greater. Again, triggering sensitivities vary in a systematic way, with the families that are most sensitive to shear-stress fluctuations locating to the northwest below the creeping section. RLSS sensitivity in the families to the northwest of Parkfield appears to correlate with depth (Figure 3.4C). RLSS N_{ex} values transition smoothly from approximately 10% in the families between 16 and 20 km depth to values of 30% below, and reach nearly 50% in families further to the northwest at depths of up to ∼28 km. The spatial pattern of RLSS N_{ex} values to the southeast of Parkfield appears to be more complex. The magnitudes of the dFNS sensitivity are about a factor of three smaller than the RLSS N_{ex} values. The spatial variation in dFNS mirrors that of the RLSS as families with significantly positive RLSS values also have significantly negative dFNS correlations (Figure 3.3D). The significance associated with the dFNS values is largely due to spurious correlation with RLSS as discussed in Section 3.2 and 4.5.

Of the 88 LFE families, only five have statistically significant values of positive dRLSS at 99% confidence. Most dRLSS N_{ex} values are negative; that is, LFE are correlated with times of decreasing right-lateral stress. As shown in Figure 3.5, the correlation of LFEs with FNS may be partially responsible for the magnitude of the dRLSS N_{ex} values; however most of the correlation cannot be explained as a product of aliasing. Within the creeping section of the fault, dRLSS values transition between statistically insignificant to around -10% N_{ex} values with depth/along strike from Parkfield to the northwest. Many of the most robustly correlated families are those within the fault-bend region to the southeast of Parkfield. However, several of the southeastern most families (along-fault distance of 20 km or greater) have significant negative values that are not associated with the bend.

Hypothesis Tests

The hypothesis testing results for the one-component case of the RLSS are shown in Figure 3.5. Observed N_{ex} values for each of the four stressing components are indicated as black dots, while the 95% and 99% confidence intervals derived by creating synthetic catalogs matching the RLSS distribution are shown in light and dark gray bars respectively. Figures

3.5 contains information about the relationship between the observed N_{ex} values and the tidal model, which can help to distinguish spurious and authentic correlations by minimizing the misfit between the observed N_{ex} values (black dots in Figure 3.5) and the 50th percentile of the confidence intervals generated from the synthetic populations for the eleven different null hypotheses. One principal result of the hypothesis testing procedure described above is that of the 88 LFE families, none is best described by the null hypothesis that LFEs are randomly distributed with respect to tides, meaning that at 99% confidence or greater one or more tidally induced stressing component is modulating LFE occurrence.

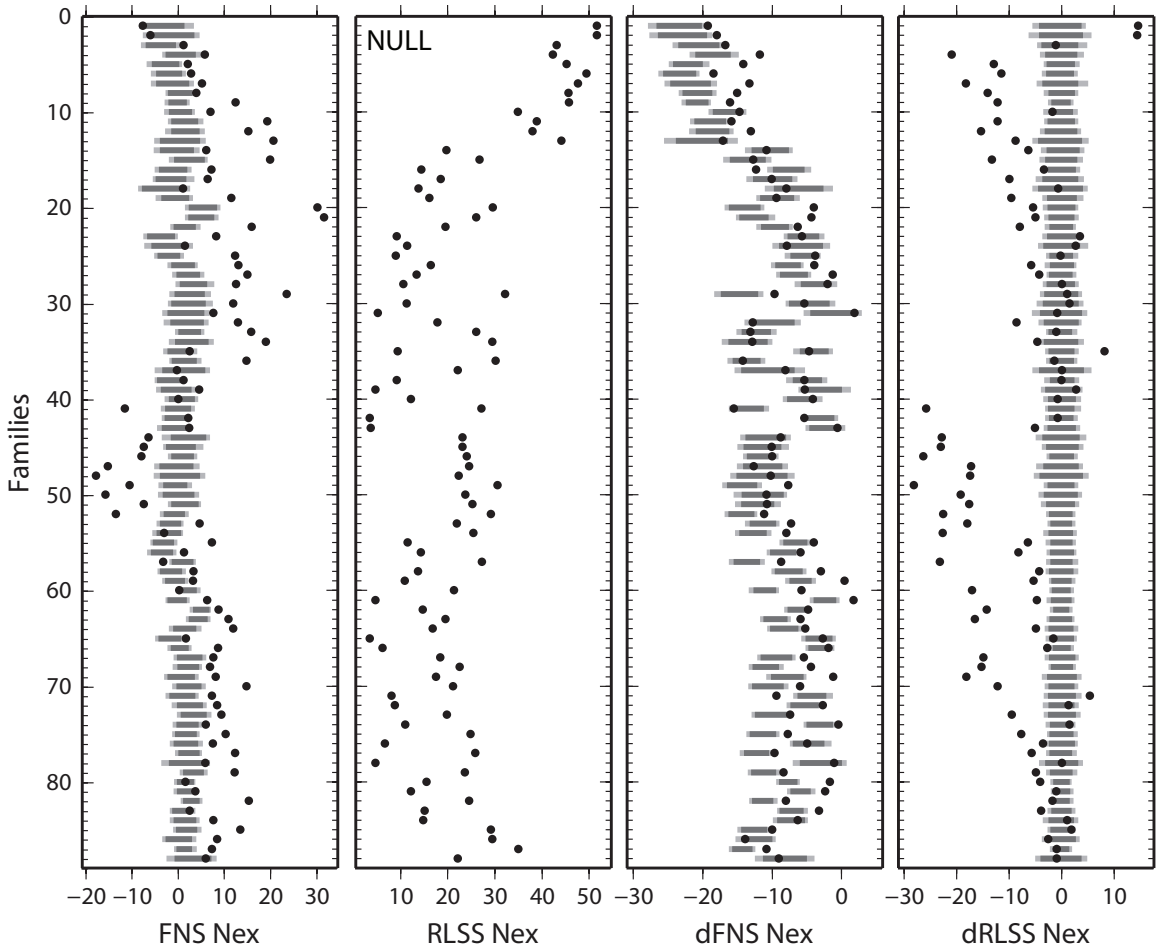

Figure 3.5: Results of bootstrap analysis with the null hypothesis that LFEs event times are influenced by the RLSS only. FNS, RLSS, dFNS, and dRLSS N_{ex} values for 88 LFE families are shown as black dots. Light and dark gray bars represent 95 and 99% confidence intervals derived from synthetic populations. The RLSS N_{ex} observations (marked NULL) have no confidence intervals because the synthetic catalogs are generated to match the RLSS N_{ex} values. Misfits are listed in Table S1.

A second important result is that LFE occurrence is most strongly associated with the RLSS. We come to this conclusion by considering that 73 of the 88 families are best characterized (lowest misfit) by the null hypotheses that either the LFE family members are preferentially triggered by the RLSS alone or that two components play a role in triggering, one of which is the RLSS. Of the 66 families that are best described by a two-component null hypothesis, 26 families are best described by the FNS-RLSS null hypothesis. These families preferentially trigger in response to a tidal stressing function that incorporates some normal-stress dependence. The second and third most abundant groups of 17 and 15 families are best described by the RLSS-dFNS and the RLSS-dRLSS respectively. The dRLSS dependence of some families may be related to factors we will discuss in Sections 3.6 and 4.6.

The correlation of 17 families with both RLSS and dFNS is likely a spurious correlation. In Figures 3.5 and S1, the deviation of the computed confidence intervals from zero is a measure of how sensitive each component is to the null hypothesis in the tidal model, independent of the observations and the sign of the deviation relative to the value of the primary component from which the distributions were generated. If the observed N_{ex} values fall within the bounds of the computed confidence intervals then the correlation between the LFEs and the secondary stressing functions may be an artifact. If, on the other hand, the observed N_{ex} values fall outside the computed confidence interval, then they cannot be explained as a spurious correlation, or aliasing resulting from the component or components used as the null hypothesis. In Figure 3.5, confidence intervals for the FNS and dRLSS are mostly centered on zero suggesting little to no correlation with the RLSS. This is to be expected for the dRLSS, as when the RLSS is positive, half the time the dRLSS is also positive and half the time its negative which should result in a distribution centered on zero. However, this is not the case for the dFNS, as almost none of the confidence intervals are centered on zero, indicating that the value of the dFNS is quite sensitive to the RLSS value. The extreme sensitivity of the dFNS values to the RLSS null hypothesis suggests that while the dFNS N_{ex} values for many LFE families are statistically significant relevant to the null hypothesis that there is no correlation between LFEs and tides, this significance is likely a spurious correlation caused by the robust correlation of those families with the RLSS. Hence, many of the observed dFNS N_{ex} values can be explained by accounting for this sensitivity (in Figure 3.5, observed dFNS N_{ex} falls within the 99% confidence range). The correlation between the RLSS and the dFNS is also evident in the observed N_{ex} values (Figure 3.6). The coefficient of determination, R^2, resulting from a linear regression of the RLSS and dFNS N_{ex} values is 0.66 indicating a robust correlation between the two (see Table S2 in the Supplemental Material for associated significance values).

While Figures 3.5 and 3.6 clearly demonstrate the sensitivity of dFNS to RLSS in the tidal model, there are significant correlations of some LFE families that cannot be explained by matching only the RLSS. Even the best fitting one or two-component hypotheses may have observations that lie outside of the generated confidence intervals. This discrepancy could be due a number of factors including unmodeled stress influences and assumptions such as fault orientation that go into our model of tidal stresses on the SAF. For these reasons, we do

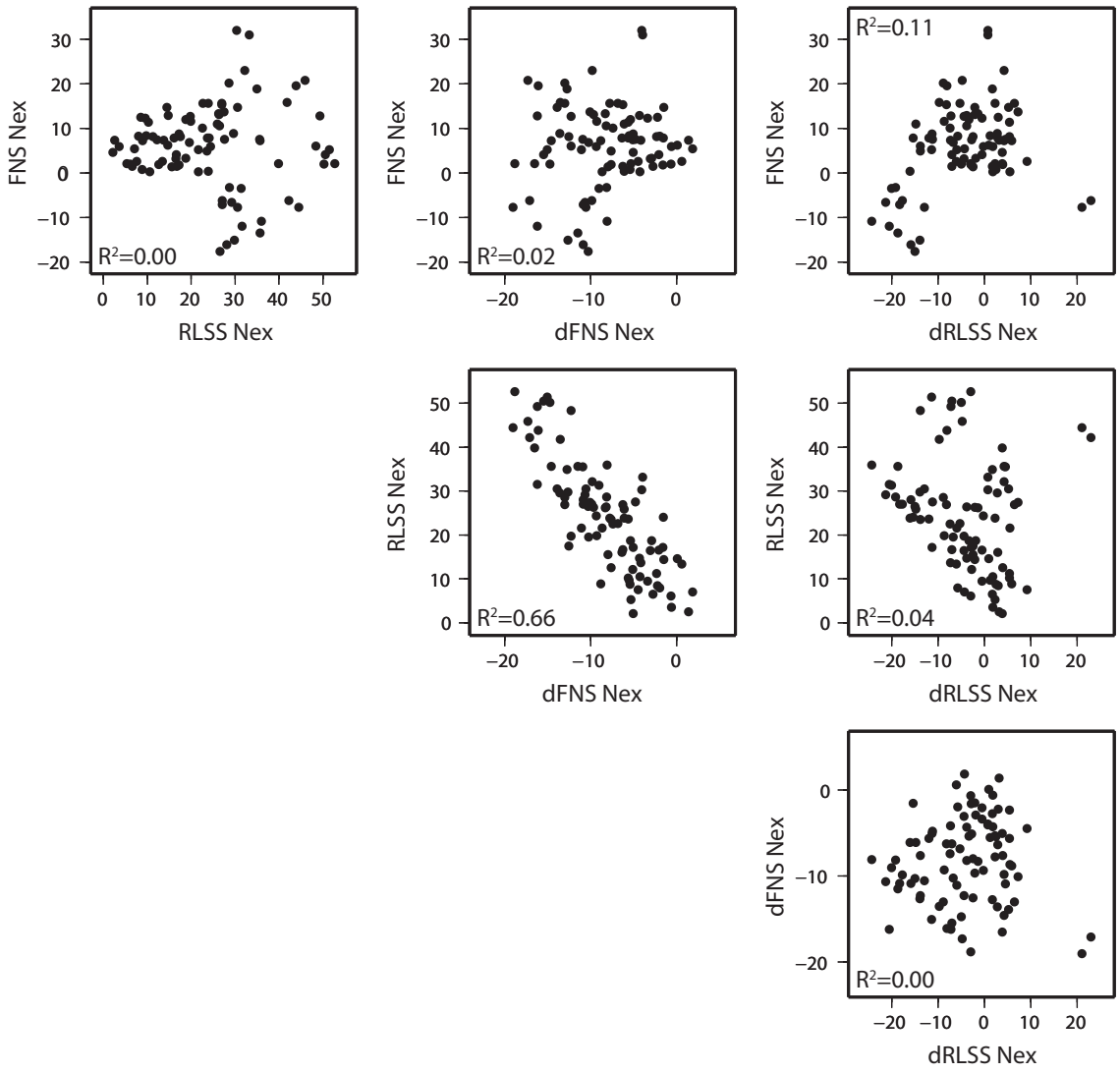

Figure 3.6: All possible combinations of N_{ex} values plotted against one another. Associated R^2 values are shown on each plot. The highest R^2 value, 0.66, suggests a spurious correlation may exist between the RLSS and dFNS components.

not require that the observed N_{ex} values for all families fall within the generated confidence intervals from a given hypothesis, but we simply consider the best-fitting hypothesis the one that minimizes the misfit between the data and the models (or hypotheses). For the remainder of this analysis, N_{ex} values are reported with respect to the null hypothesis that LFEs have no correlation with tidally induced stress, as they are a good metric for reporting the sensitivity of LFEs to tidally induced stresses and can be compared between components.

Tidal Sensitivity as a Function of Recurrence Interval

Hawthorne and Rubin (2010) document the contemporaneous increase of tidal stresses on the plate interface and measured surface strain rates due to accelerated slip in the Cascadia subduction zone. Using this result, they inferred that tides are capable of modulating the slip rate of SSEs (*Hawthorne and Rubin*, 2010). More recent studies of spatio-temporal characteristics of slow-slip fronts find that in addition to quasi-continual slip front advance, rapid back-propagating slip pulses, called rapid tremor reversals, are also apparent (*Houston et al.*, 2011). Rapid tremor reversals may also be tidally correlated (*Houston et al.*, 2011), which suggests that tidally correlated strain rates could be caused by tidal influence on the slip velocity, slip front advance, or both. Recent studies of slip in Cascadia argue that slip and tremor are spatially and temporally coincident; hence NVT can be considered a proxy for the location of deep fault slip (*Bartlow et al.*, 2011). If we extend this result to Parkfield, we may be able to gain additional insight into the mechanics of slow-slip fronts by using the recurrence times within respective families to separate the catalog into two end-member groups: LFEs that represent the initiation of slip on a particular asperity following a slip hiatus, and those that occur either as part of an ongoing episode (intra-event LFEs) or between episodes. We then examine the tidal correlation of these different populations which allows us to assess whether tides modulate the slip rate and/or the slip front velocity.

The majority of LFE families have average recurrence intervals less than three days, including both the deep, constant rate families with repeat times averaging two to three days and intra-event LFEs that occur in the shallow episodic families with repeat times of much less than one day. We can distinguish initiating LFEs, or those that signal when a creep pulse arrives at an LFE hypocenter, from those that take place either as part of a creep event or those that occur in more continuous families (e.g. family 85 in Figure 3.2) by filtering LFEs as a function of the duration of the preceding recurrence interval, t_r. The population of LFEs with large values of t_r, should largely consist of initiating LFEs. A small fraction of events within the most episodic families do occur between large creep events so to further distinguish initiating events, we also require that the time between a particular LFE and the subsequent LFE be less than one day to exclude such events.

The results of this analysis are shown in Figure 3.7, which plots the FNS and RLSS N_{ex} values for each population of events with recurrence intervals greater than t_r. For small values of t_r (minute timescales) nearly all events in the catalog are included, as indicated by the y-axis in Figure 3.7. As t_r increases, first the events with very short recurrence intervals, such as those that within the slip episodes experienced by families 19 and 65 (Figure 3.2)

are filtered followed by events that take place as part of the deep, continuous families such as family 85 (Figure 3.2) which correspond to multiday t_r values. Finally, at many day timescales, initiating LFEs in families of intermediate episodicity are also filtered out leaving only the initiating LFEs in the highly episodic families. The corresponding RLSS N_{ex} values appear to decrease systematically with increasing t_r but remain significant over a wide range of interval durations. As the size of each population of events decreases with increasing t_r, the N_{ex} confidence intervals associated with each population shown in panels A and B grow wider. The FNS and RLSS N_{ex} values fall above the 99% confidence intervals for correlation until 43 and 25 days respectively. Slip events in Parkfield appear to vary in size, pattern, and duration, so it is difficult to place a definitive t_r cutoff to differentiate initiating events from all others. The most episodic families have average inter-episode periods of ∼60 days and episodes at a given family typically last ∼5 days. While the 43 and 25 day values are less than the average inter-episode period, they are much greater than the average duration of a creep event in a highly episodic family. This result indicates that the population of LFEs that occur when a creep event arrives at an LFE hypocenter is correlated with both positive RLSS and tensile FNS. We discuss the implications of this finding in Section 4.2.

LFE Rate Variation as a Function of Tidal Stress Magnitude

In addition to quantifying the influence of tidal stresses on LFEs in the binary sense (Figure 3.4), we further explore how specific stress levels influence LFE production by computing LFE rates as a function of the magnitude of the applied stress. Figure 3.8 is constructed by dividing the observed number of LFEs for a particular family that fall within a given stress range for the stress component under consideration by the expected value based on the null hypothesis that LFEs and tides are randomly correlated. The resulting quantity is equivalent to $1 + N_{ex}$ for each stress bin. This process is repeated for each stress range of a given stress component and for all families. In Figure 3.8, the ratios of actual to expected number of LFEs are color-coded so values above one (warm colors), indicate a surplus of LFEs in that particular stress range and ratios below one (cool colors) indicate a deficit relative to the expected value. The abundance of values near one for the FNS plots confirms most families are generally not strongly influenced by the fault normal stress (or at least not to the degree of the RLSS). A few notable exceptions include families 19-22 and 26-29 which have LFE surpluses that correlate with peak tensile FNS. In addition, families 41, 44, 45, and 49-57 correlate with fault-normal clamping. In contrast to the FNS, substantial modulation of LFEs by the RLSS is almost ubiquitous for all 88 LFE families and well correlated with the stress magnitudes. Correlation between the stress amplitude and LFE rates is strongest in families 1-13, with a smooth rise of LFE rates with increasing RLSS. For families with strong RLSS correlation, LFE families are nearly quiescent when tidal stress is negative, with ratios near zero for RLSS less than -100 Pa.

The results of the hypothesis testing analysis reported in Section 3.2 indicate that the majority of the deviation of the dFNS N_{ex} values from zero is a spurious product of the robust correlation with RLSS. The correlation between triggering patterns of RLSS and

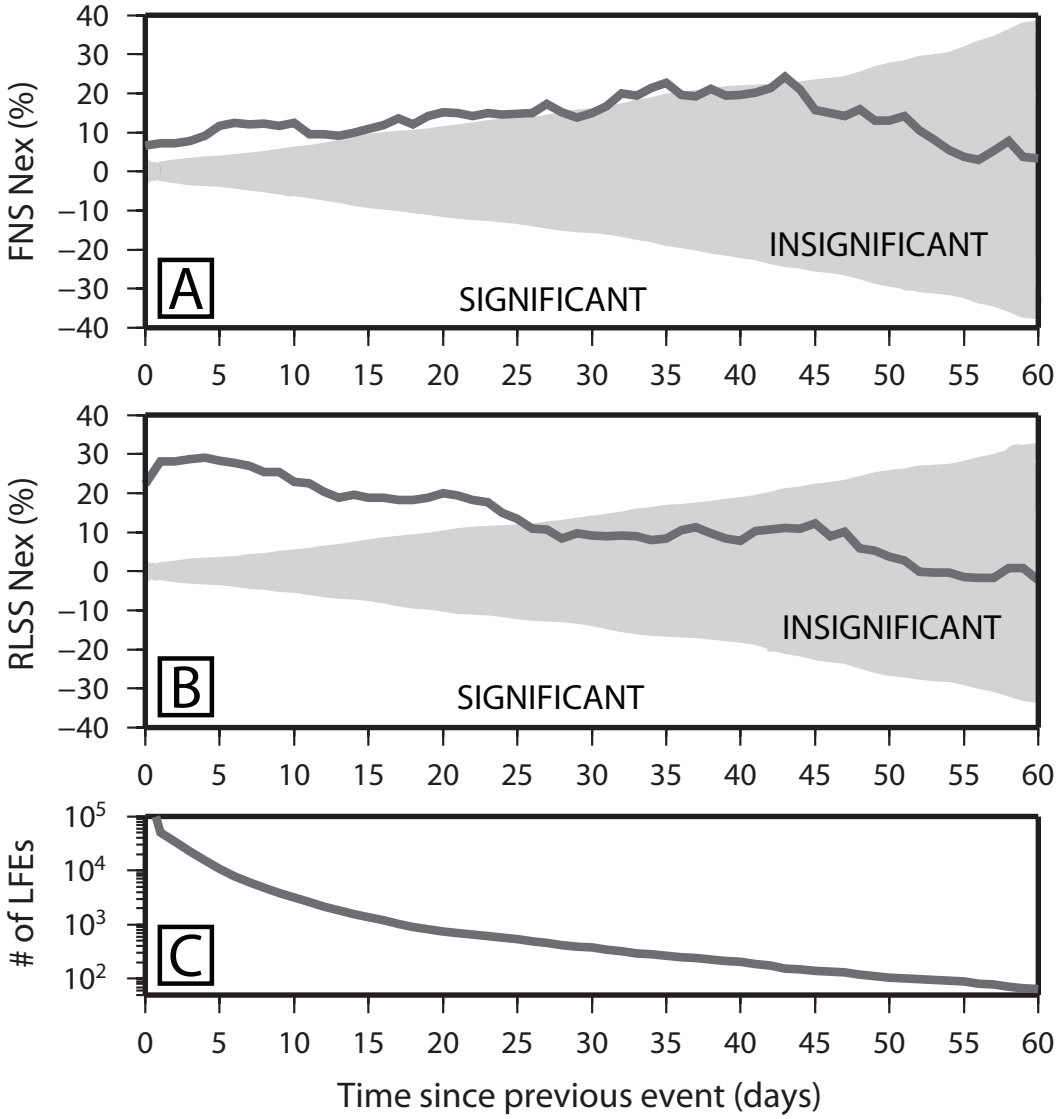

Figure 3.7: Panels A and B show the FNS and RLSS N_{ex} values (dark gray lines) calculated for all LFE events whose preceding recurrence interval is longer than the respective x-axis value (t_r). White background color represents N_{ex} values that are statistically significant at the 99% confidence level while values in the gray region are statistically insignificant. Panel C shows the number of events in each population; since population size rapidly decreases with t_r, 99% confidence regions in panels A and B grow larger. Note that the ∼450,000 LFEs corresponding to the shortest time intervals are not shown.

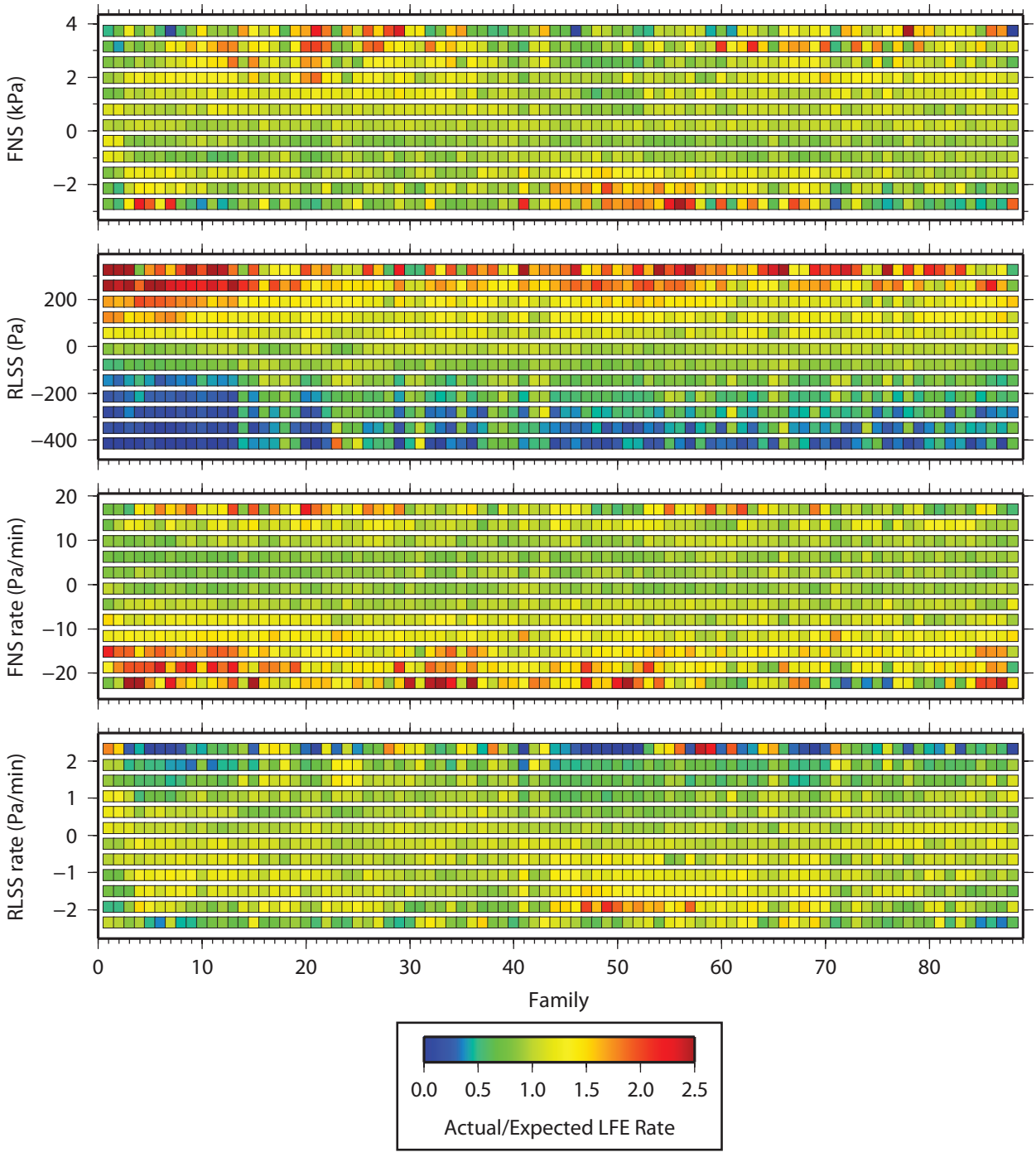

Figure 3.8: LFE rate plots for each tidally induced stressing component. Panels correspond to fault-normal stress, right-lateral shear stress, and their respective rates. Each column corresponds to an individual LFE family and each row, a stress interval. Each square is color-coded by the ratio of the actual number of LFEs within a given stress range over the expected number of LFEs that should occur within that range if tides and LFEs are uncorrelated (this reflects the amount of time the tides spend in the given range assuming a constant rate of LFE production). Cool colors represent a deficit of LFEs in the respective bin while warm colors indicate a surplus.

dFNS are fairly evident in the 2nd and 3rd panels of Figure 3.8 with families with rate ratios that systematically increase as a function of the RLSS (gradual transition from blue to red) having a large excess number of events at negative values of dFNS (transition from tension to clamping). This is most evident in families 1-13, 32-36, and 47-54 however there are counterexamples, such as 69-74, that have LFE deficits at low dFNS values, despite robust correlation with RLSS.

We reserve the detailed analysis of the dRLSS dependence for Section 3.6, however, to first order an excess number of LFEs occur when dRLSS values are negative (i.e. with decreasing stress magnitude). For most families with significant dRLSS dependence, the highest ratios of actual to expected number of LFEs occur at negative but not extreme rate values.

Optimal Fault Azimuth for Tidal Correlation and the Role of Friction

Tidal stresses are largely volumetric with a very small deviatoric contribution. For this reason, the FNS and dFNS N_{ex} values are relatively insensitive to the choice of fault azimuth, while the RLSS and dRLSS substantially change as a function of the assumed strike of the fault. *Thomas et al.* (2009) found that when the azimuth of the plane onto which the tidal stresses were resolved was allowed to vary, the orientation that maximized the excess percentage of NVT relative to the expected number of events was W44°N, parallel to the SAF strike. To further explore azimuthal dependence, we determine the optimal azimuth for each LFE family by finding the fault orientation that maximizes the number of LFEs that occur when tidally induced stresses promote slip in a right-lateral sense. To characterize the stressing function we consider two different friction coefficients: $\mu = 0.1$ and $\mu = 0$ or purely right-lateral shear stress dependence. Low friction values are suggested by the strong dependence on RLSS and optimal correlation of tidal stress and tremor at $\mu = 0.02$ found by *Thomas et al.* (2009). If we consider μ values greater than 0.1, the order-of-magnitude higher FNS stresses dominate the change in Coulomb failure stress, resulting in substantially reduced N_{ex} values and sometimes spurious orientations of peak correlation azimuths. Figure 3.9 illustrates the dependence of N_{ex} on fault azimuth and μ for four example families. Family 4 located along the creeping SAF shows maximum correlation ($N_{ex} = 48\%$) at $\mu = 0$ and azimuth of N40°W. As the assumed friction value increases above 0.2 N_{ex} values drop to less than 20% with the optimal azimuth remaining roughly aligned with the SAF. Family 21 is part of a deep-seated group of sequences with significant correlation with RLSS and with tensile FNS. Peak correlation occurs at low friction values but N_{ex} values remain significant at greater values of μ for all orientations due to the small variation of FNS with azimuth. The shallow family 65 shows peak correlation ($N_{ex} = 10$ %) for fault azimuths of N30-40°W and $\mu = 0$. However, when higher contributions of FNS are considered, the orientation of peak correlation becomes highly variable and N_{ex} values fall to below 5% and are not statistically significant. Family 41 is located along a right bend in the SAF and belongs to a group that

exhibits pronounced correlation with compressional FNS. We again find peak correlation at zero friction along N40°W. As the contribution of FNS to the failure function is increased, N_{ex} values decrease but do not show a strong change in their spatial distribution. Peak N_{ex} values are generally found at very low or zero μ values. As tidal FNS is about an order of magnitude greater than RLSS, the correlation rapidly decreases with increasing μ.

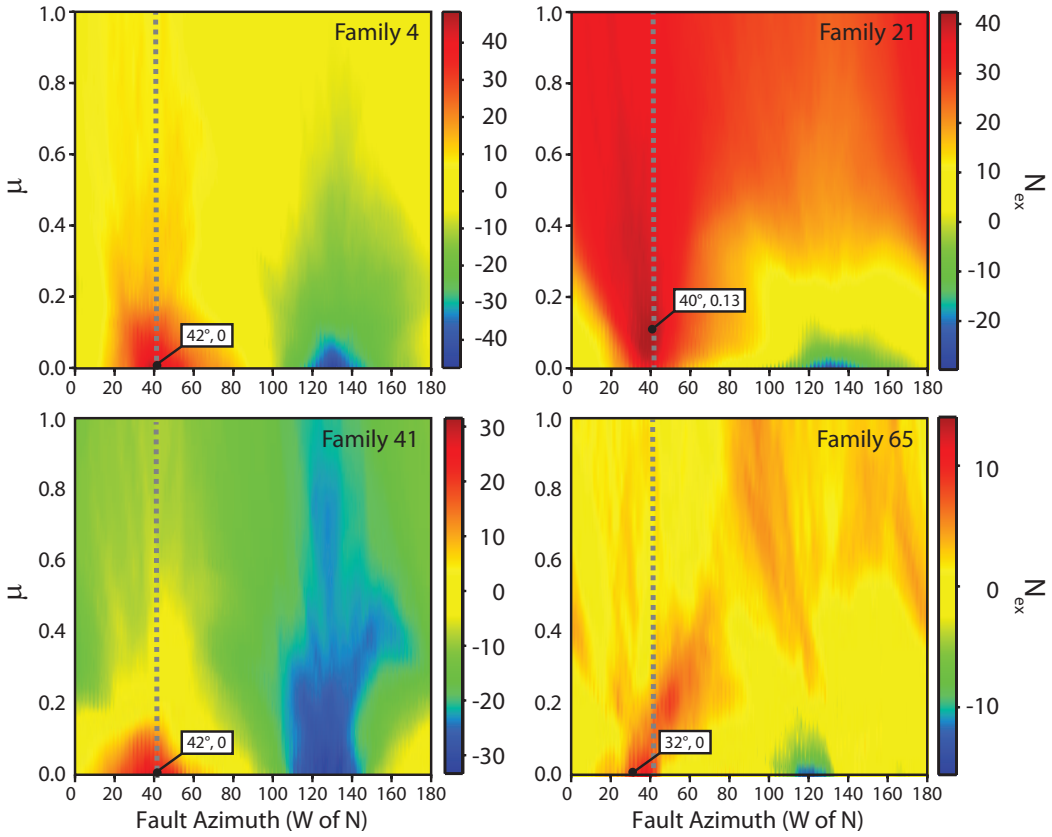

Figure 3.9: N_{ex} values as a function of azimuth and friction coefficient, μ, used to calculate tidal Coulomb stress (CFF = RLSS + μFNS) for four families (4, 21, 65 and 41 see Figure 3.4 A for locations). Vertical line indicates the average local strike of the SAF (N42°W) and a black dot indicates peak N_{ex} for Coulomb stressing.

Figure 3.10 shows the optimal orientation and corresponding Coulomb stress N_{ex} values for $\mu = 0$ and $\mu = 0.1$ showing lines aligned with the optimal orientation centered on the respective LFE hypocenter and circle colors indicating the corresponding N_{ex} values. The mean and standard deviations for both populations are reported in the bottom left of Figure 3.10 A and B. One immediately obvious feature for both friction coefficients is the tight clustering of the axes around the average orientation of the San Andreas (N42°W). A few families peak-correlation orientation diverges from the fault strike by as much as 30°

counterclockwise. The optimal orientation for these families more closely aligns with the San Andreas when we consider the modestly raised friction coefficient.

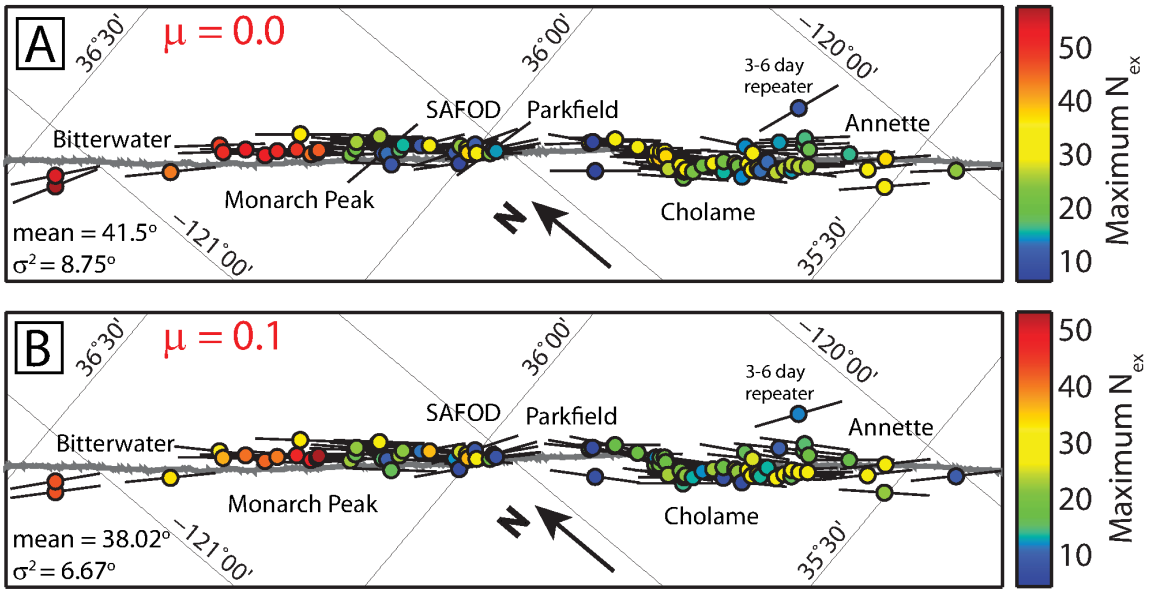

Figure 3.10: Rotated map view of SAF with LFE hypocenters color-coded with respect to N_{ex} value corresponding to the optimal orientation. Optimal orientations, defined as the orientation that maximizes the N_{ex} value, for each family are shown as black lines centered on the respective LFE hypocenter. Panels A and B use friction coefficients of 0 and 0.1 to demonstrate the sensitivity of the optimal orientation to choice of friction coefficient. Mean orientations in degrees west of north and standard deviations for all families are shown in bottom left corner.

Phase of LFE Failure Times Relative to Tidal Load

An effective tidal phase is assigned to each LFE by normalizing the magnitude and rate of the FNS and the RLSS at the time of the event by the absolute value of the most positive (or negative depending on the sign) value the stress or stressing rate can attain. In this way, x-(magnitude) and y-values (rate) range between -1 and 1 and a phase value can be obtained for each event. A phase of zero (up) corresponds to the maximum rate and zero magnitude, a phase of 90 corresponds to maximum magnitude and zero rate, etc. Polar histograms are constructed by grouping the phases of all LFEs within a particular family in 10 degree bins and then normalizing each bin by the number of events expected to occur in that range based on the tidal stress distribution. Thus, the radial dimension of the histogram is the actual over the expected number (N_{ex} + 1) of events for that particular range of phases (expressed as a percentage in Figure 3.11A). A bin that contains the number of LFEs expected based

on the tidal distribution has a radius of one (i.e. the expected 100% value assuming no tidal triggering). The full radial dimension of the phase plots corresponds to double the expected number of events.

Results for example families 4, 22, 35, 41 (locations labeled in Figure 3.4A), and the complete catalog are shown in Figure 3.11. Family 4 generally shows very weak FNS dependence and extreme sensitivity to tidally induced RLSS (RLSS N_{ex} value of 48%), which is evident from the phase plots in Figure 3.11B. Radial values on the right half of the diagram corresponding to positive magnitude are almost entirely above the expected value, with a corresponding depletion of LFEs during negative magnitude RLSS on the left half of the plot. The event excess also seems to be rate dependent as evidenced by the post-maximum magnitude RLSS peak which indicates preferential failure during times of moderate negative dRLSS.

Family 22 is an example from the cluster of deeper families with moderate to strong RLSS correlation (23% RLSS N_{ex}) also characterized by preferential failure during times of extensional normal stress (16% FNS N_{ex}). The FNS phase plot for family 22 shows preferential failure during times of peak-positive FNS. Family 22 also has a substantial positive RLSS dependence which may explain why there are sometimes more events than expected during times of negative (compressive), decreasing FNS. The correlation with decreasing FNS is likely due to the aliasing effect between the RLSS and dFNS mentioned in Section 3.2. Family 35 is shallow and less sensitive to tidally induced stresses as evidenced by the majority of bins within the phase plot falling near the expected value, within the 99% confidence bins. Family 41 (-12% FNS N_{ex}, 32% RLSS N_{ex}) is a member of the anomalous group of families that fail preferentially during times of negative FNS. The correlation with negative, decreasing FNS is apparent in the phase plot of family 41. In family 41 events cluster with broad peak in the positive, decaying RLSS and strong FNS peak in the quadrant of increasing compression.

Families 4 and 35 represent two end-member types of behavior; however, some families have patterns that are not as readily interpretable. The general correlation of all families within the catalog to RLSS is apparent in the stacked phase plot of all LFEs within the catalog. The large number of events (N=544,369) reduces the confidence intervals to very near the expected value, hence any deviations from that value are highly significant. If LFEs correlated with only RLSS magnitude, then we would expect the region that exceeds the expected value to be symmetric about the magnitude axis. However, the phasing of failure times with respect to RLSS seem to be phase dependent, as the majority of LFEs fail during times of large, positive RLSS magnitude and small, negative dRLSS which produces an $\sim$30 minute phase shift in the time of the peak radial value with respect to the peak RLSS. This effect is also apparent in the dRLSS N_{ex} values reported above and shown in Figure 3.4E. Families that are highly sensitive to negative FNS are generally most robustly correlated with negative dRLSS. However, these families are not solely responsible for the apparent phase shift as the same dRLSS dependence is still present when we iterate the analysis while excluding families correlated with negative FNS. We discuss the possible causes of this apparent phase shift in the correlation with tidal RLSS in Section 4.5.

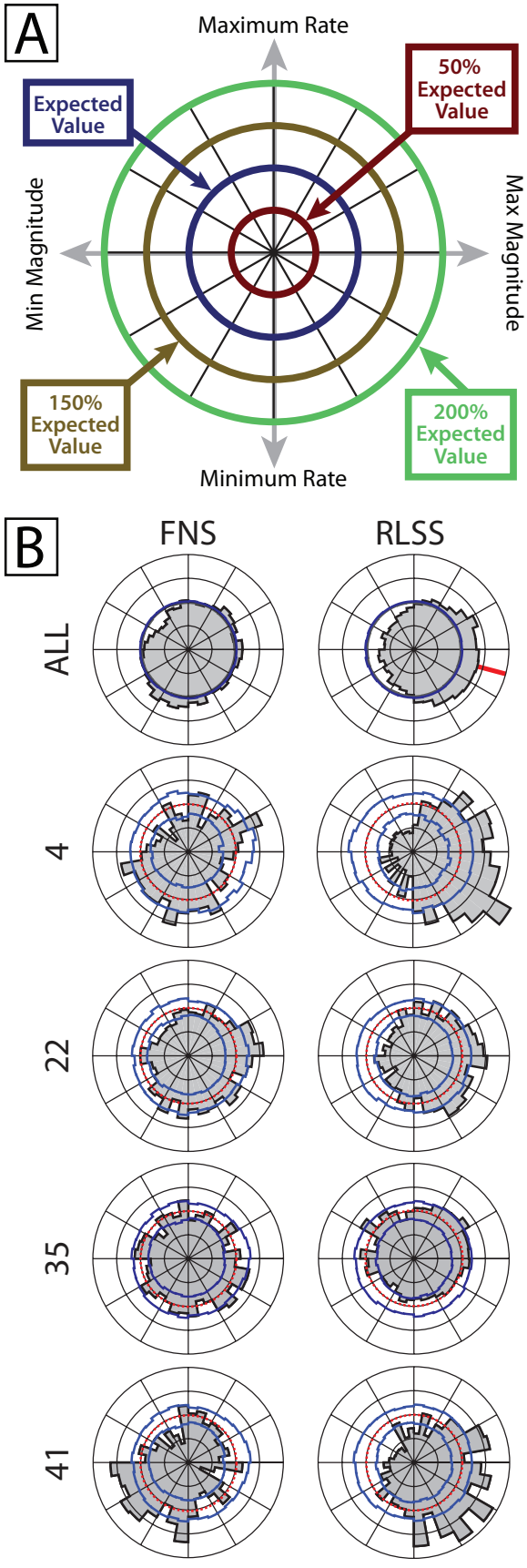
A
Maximum Rate
50% Expected Value
Expected Value
Min Magnitude
Max Magnitude
150% Expected Value
200% Expected Value
Minimum Rate
B
FNS
RLSS
ALL
4
22
35
41

Figure 3.11: Panel A shows a schematic phase plot labeling the 50%, 100%, 150% and 200% expected value contours. FNS (left) and RLSS (right) phase plots for a stack of all events in the catalog and four example families (4, 22, 35, and 41) are displayed in panel B. Gray shaded areas indicate ratio of observed to expected number of events in each 10 degree phase bin. Thin dark blue lines are 99% confidence intervals for each population. Thin dashed red lines are 100% expected value contours. The solid red line in the RLSS phase plot for the bulk catalog marks the half hour phase shift discussed in the text.

3.4 Discussion

As the most studied continental transform environment known to host tremor and transient fault slip, diagnostic observations of slow slip in Parkfield complement those in subduction zones providing additional information about the mechanics of slip in deep fault zones. Full azimuthal station coverage, a high-resolution seismic network, and detailed waveform analysis help us better constrain the location and timing of individual LFEs in Parkfield. If the same underlying physics for slow-slip generation applies to both subduction zone environments and continental settings, then the observations of LFEs in Parkfield may aid in developing generally applicable models of SSEs not limited to tectonic environment. In the following sections we discuss the implications of the results presented in Section 3.

Spatial Distribution of Tidal Sensitivity and LFE Episodicity

Our observations of tidal modulation of LFEs in Parkfield is generally consistent with previous studies that report statistically significant influence of the ocean and solid Earth tides on slow slip and NVT in subduction zones (*Rubinstein et al.*, 2008; *Nakata et al.*, 2008; *Lambert et al.*, 2009; *Hawthorne and Rubin*, 2010; *Ide*, 2010). The enhanced spatial and temporal resolution afforded by studying LFEs allows us to map the spatial variability of tidal influence and infer from those observations the spatial heterogeneity of fault mechanical properties. We are able to separate the contribution of shear and normal stress components and their rates to the triggering.

The majority of LFE families are highly correlated with RLSS, however the spatial variability of tidal correlation below the creeping and locked sections of the SAF has different characteristics. Along the creeping section of the SAF to the northwest of Parkfield, the correlation systematically increases from less than 10% N_{ex}, below the Parkfield earthquake at 16 km depth, to above 50% N_{ex} with both distance to the northwest and depth. To the southeast of Parkfield RLSS N_{ex} values continue to be high, but their spatial distribution is more complex with substantial along-fault changes and lack of a consistent change with depth (Figure 3.4 C). A number of factors can influence the sensitivity of LFE sources to small stress perturbations, however, the magnitudes of the RLSS sensitivity in nearly all

families require that elevated pore fluid pressures be present on the deep SAF (Section 4.3). Most families are weakly correlated with positive FNS, however there are two groups of families that correlate with positive and negative FNS (labeled in Figure 3.4 B). From the analysis presented in the next section, and due to the spatially localized nature of these groups, we believe these correlations are not artifacts. We discuss potential causes of the negative and positive FNS N_{ex} values in Sections 4.6 and 4.7 respectively.

Study of LFEs also allows for a more detailed assessment of the relationship between the distribution of LFEs in time (i.e. episodic vs. continuous) and tidal influence. To quantify the episodicity of individual LFE families, *Shelly and Johnson* (2011) used the minimum fraction of days required to contain 75% of all events within a family (MFD75). Highly episodic families (e.g., 65 in Figure 3.2) are characterized by MFD75 values around zero while continuous families (e.g. family 85 in Figure 3.2) have values around 0.25. The relationship between episodicity, depth, and tidal modulation is shown in Figure 3.12. We find that highly episodic families with bursts of LFEs interspersed with episodes of quiescence are less tidally influenced than the deeper, continuously deforming families. Families with low MFD75 values tend to be shallower and have either insignificant or small N_{ex} values when compared with the rest of the catalog. If we consider the fault essentially locked during quiescent periods with the punctuated LFE bursts representing times when the fault is slipping at the particular hypocenter, then weaker tidal modulation may suggest the magnitude of tidal correlation decreases during strongly accelerated fault slip, as the stress applied to any asperity due to an accelerated background slip rate is likely much larger than the tidal stress contribution. More continuously active LFE families (high MFD75 values in Figure 3.12) show a wide range of N_{ex} values in both FNS and RLSS components that suggest that other factors can dominate the degree of tidal correlation.

There are similarities and differences with the temporal and spatial patterns of tremor found in subduction zones. *Ide* (2010) explored the relationship between tremor and tidal sensitivity in Shikoku, and found a correlation between deformation style, depth, and tidal influence. At Shikoku, the longer-lasting tremor events occur at greater depths in small and frequent episodes while the duration of shallow NVT events are shorter and occur primarily during large and infrequent tremor episodes, two or three times per year (*Obara*, 2010; *Ide*, 2010). However, to first order the sensitivity to tidal stress appears to be strongest in the shallow portions of the tremor region at Shikoku, in contrast to our results (*Ide*, 2010). *Ide* (2010) did not explicitly model the distribution of tidal stresses in space and time so it is difficult to ascertain if the distribution in tidal sensitivity reflects differences in tidal stress or source region behavior. Further comparisons are difficult to make due to the application of different detection and location methodologies. Smaller tremor episodes without geodetically detectable slow slip identified in Cascadia (*Wech et al.*, 2009; *Wech and Creager*, 2011), Mexico (*Brudzinski et al.*, 2010), and Oregon (*Boyarko and Brudzinski*, 2010) also occur downdip of the section of the megathrust that hosts larger SSEs. This suggests a transition from highly episodic to continuous deformation with depth in those locations, which is qualitatively consistent with Parkfield. Correlation with tidal stress has so far only been documented during large and shallow SSEs in Cascadia (*Rubinstein et al.*,

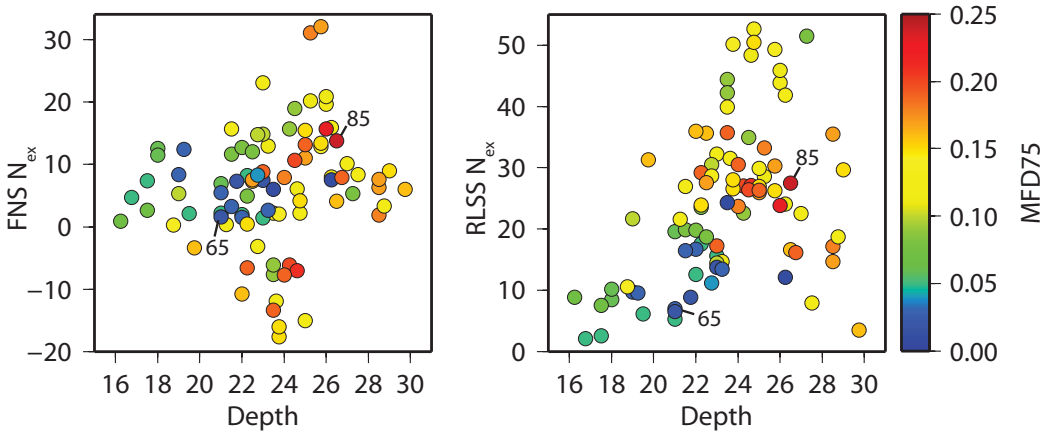

Figure 3.12: Variation in FNS and RLSS N_{ex} values for all LFE families plotted as a function of depth. Families are color-coded by their MFD75 value from *Shelly and Johnson* (2011). Lower MFD75 values correspond to highly episodic families while higher values correspond to more continuous families. The shallow and episodic family 65 and deep and continuous family 85 shown in Figure 3.2 are labeled.

2008; *Lambert et al.*, 2009; *Hawthorne and Rubin*, 2010). Future work should evaluate to what degree tidal sensitivity of tremor changes with depth and/or size and recurrence interval of NVT episodes in these areas.

Slip Front Propagation and Slip Velocity

We motivated Section 3.3 by asking if increased strain rates during periods when tides are encouraging slip were due to tidal modulation of slip velocity or tidal influence on slip front velocity (*Hawthorne and Rubin*, 2010). Since most of the very episodic LFE families have statistically significant RLSS N_{ex} values, and the vast majority of LFEs within these families occur during slip events, we can confirm that slip rates are tidally modulated during an ongoing slip episode. The modulation of LFE rates in the presence of an ongoing slip episode suggests that the slip velocity is tidally modulated, consistent with the findings of *Hawthorne and Rubin* (2010) for the Cascadia SSEs.

To address whether tides also control slip front or propagation velocity we analyzed the tidal correlation of LFE populations filtered by the duration of the preceding recurrence interval t_r (Figure 3.7). The majority of LFEs with large prior recurrence intervals represent the first event in an episode at a family location, and thus may indicate when a creep front arrives at the location of a particular LFE hypocenter. From our analysis in Section 3.3, we find that the population of LFEs following a quiescence of several days are still strongly tidally correlated. So why should the first seismic signature of a slip pulse at an LFE family hypocenter correlate with the tides? One possibility is that creep front propagation

is tidally controlled; meaning the shear and normal stress perturbations are of sufficient magnitude to accelerate or decelerate the advance of the slipping region of a fault. If is were true, slip fronts may advance faster during times when tides are inducing stresses favoring slip front propagation. At present, geodetic studies of the spatio-temporal progression of slip in Cascadia are not of sufficient precision to resolve if slip front propagation speeds are tidally controlled (*Hawthorne and Rubin*, 2010; *Bartlow et al.*, 2011). The tremor locations in *Houston et al.* (2011) do provide the required temporal resolution however, to our knowledge, time-dependent changes in slip front advance have not been explored.

A second cause of this apparent correlation could be that the onset of a slow slip front occurs on time scales that are either equivalent to, or greater than tidal timescales. If slip were to nucleate and accelerate to slow slip speeds on timescales much shorter than tidal periods, we would expect to see no tidal dependence of slip nucleation, as LFEs should behave in an aftershock-like manner to the near-instantaneous application of stress. For example, *Shelly and Johnson* (2011) show that LFEs respond to stress transfer from the Parkfield and San Simeon earthquakes with a near-instantaneous increase in event rate. However, if the duration of onset is greater or equal to tidal periods then LFEs may preferentially trigger at times that are tidally favorable. Many slip episodes, like those shown in Figure 3.2 Familiy 65, do appear to onset gradually with several hours between the first event within an episode and sustained elevated event rates. This gradual onset of slip events qualitatively supports this hypothesis, as LFE rates during some slip episodes accelerate between the first discernable onset of slip and peak event rate over hourly timescales.

Tidal Sensitivity and LFE Source Properties

What do the spatial variations in tidal sensitivity reveal about underlying changes in source properties or conditions? Multiple studies have inferred high pore fluid pressures in the tremor source region of subduction zones from high V_p/V_s ratios and the influence of small stress perturbations on tremor rates (*Audet et al.*, 2009; *Shelly et al.*, 2007b). Laboratory experiments and numerical models of faults with rate and state dependent strength suggest earthquakes have a greater probability of being triggered as the ratio of the oscillatory stress amplitude, τ, to the effective fault-normal stress, σ_n, increases (*Lockner and Beeler*, 1999; *Beeler and Lockner*, 2003). Since the ratio τ/σ_n for a fixed amplitude perturbation is greater in regions with high pore fluid pressure, low effective stress also provides a potential explanation for the sensitivity of LFEs to extremely small stress changes. We can quantify the effective normal stress required to produce the observed rates of LFE occurrence for each family using the equation

$$R(\tau) = r \exp(\frac{\tau}{a\sigma_n}) \tag{3.1}$$

where $R(\tau)$ is the rate of occurrence of LFEs in response to the tidally induced shear stress τ, r is the average rate of LFE occurrence based on the null hypothesis that LFEs and tides are randomly distributed, a is the rate parameter, and σ_n is the effective normal stress in the LFE source region (*Dieterich*, 2007). To determine the effective normal stress for each

family, we fit Equation 1 to the RLSS rate plots discussed in Section 3.4 and find the value of $a\sigma_n$ that best describes the data in the least squares sense. We assume a value of 0.02 for a, appropriate for granite at hydrothermal conditions (*Blanpied et al.*, 1995), to produce the effective normal stresses shown in Figure 3.13. One caveat to this analysis is the constant normal stress assumption. If pore fluid pressures are indeed near lithostatic, fluctuations in tidally induced FNS may be a significant fraction of the effective normal stress in the LFE source region. We discuss the constant normal stress assumption in this calculation in detail in Section 4.5, however, considering that most families have significant values of FNS N_{ex}, those correlations are induced by stresses an order of magnitude higher than tidally induced shear stresses suggesting the overall effect of FNS is modest relative to the RLSS.

For the majority of families, our estimates of effective normal stresses are extremely small, averaging around 30 kPa, compared to the ambient lithostatic pressure of 500-700 MPa. The distribution of pore-fluid pressure largely reflects that of the RLSS N_{ex} values shown in Figure 3.4 C. Families with the highest RLSS N_{ex} values and lowest effective normal stress estimates cluster to the northwest within the creeping section of the SAF and at greater depths. Values of σ_n gradually increase to near 70 kPa in the shallower families near the Parkfield hypocenter. The average σ_n value from Figure 3.13 is five orders of magnitude smaller than values assuming lithostatic overburden and hydrostatic pore fluid pressure. The only parameter in Equation 1 capable of varying over multiple orders of magnitude is σ_n, as the tidal stresses and event rates are well constrained and laboratory experiments performed under hydrothermal conditions appropriate for the LFE source region indicate a can vary by at most an order of magnitude between 10^{-2} and 10^{-3} (*Blanpied et al.*, 1995). This suggests generating LFE rates equivalent to those observed requires near-lithostatic pore fluid pressure to produce effective normal stress values of 10-100 kPa.

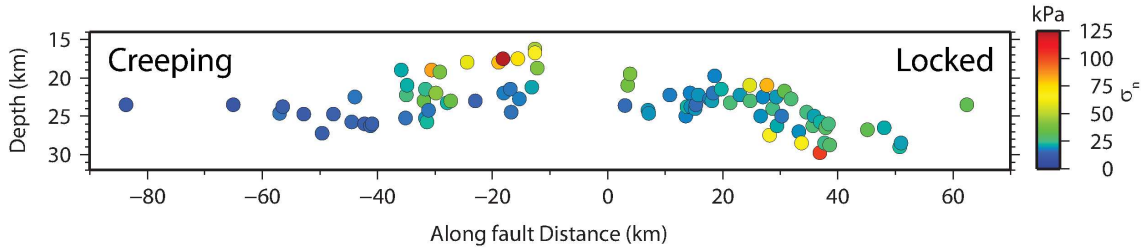

Figure 3.13: Along fault cross section (identical to Figure 3.4) with family hypocenters color-coded by effective normal stress derived from Equation 1.

Most modeling efforts of transient fault slip focus on SSEs instead of accompanying tremor that represents a small fraction of the total moment released in an episodic tremor and slip event (*Kao et al.*, 2010). For a synopsis of models explaining slow slip and associated caveats see *Segall et al.* (2010), *Rubin* (2011), and references therein. While the specific model features that give rise to slow slip vary, the common goals of each modeling effort are

to (1) nucleate slip without allowing it to accelerate to seismic slip speeds, (2) match, with reasonable variability, the observations associated with SSEs (e.g. slip front propagation speeds, recurrence intervals, size of slipping area, etc.) and (3) not require excessive fine-tuning of initial conditions. High pore fluid pressure is not necessarily required to produce slow slip, however, it is a common feature in models of SSEs as it provides a physical basis for the large dimension of the slipping region and can increase the efficiency of the slip quenching mechanism as in *Segall et al.* (2010). The relationship between slow-slip and tremor has not been fully explored, and developing quantitative frameworks that explain characteristics of both phenomena are candidate problems for future research efforts (*Beroza and Ide*, 2011).

Conceptual models of slow slip and LFEs generally involve multiple small asperities capable of generating seismic radiation in a region that is otherwise slipping aseismically (e.g. *Ando et al.* (2010)). Numerical models of slow slip necessitate velocity weakening frictional parameters at large length scales to produce slow slip (*Liu and Rice*, 2005, 2007; *Rubin*, 2008; *Segall et al.*, 2010). One way to produce aseismic (or not detectably seismic) slip on a velocity weakening fault is through the stiffness. In fault-rock systems the stiffness is a proxy for the size of an asperity. When compared to a reference value, the stiffness determines if an asperity will fail via stick-slip or stable sliding (*Ruina*, 1983; *Rice and Ruina*, 1983). *Ruina* (1983) defined the critical stiffness or the boundary between these two end member behaviors as

$$K_{crit} = \frac{(b-a)\sigma_n}{d_c} \tag{3.2}$$

Where a and b are the rate and state parameters, σ_n is the effective normal stress, and d_c is a characteristic dimension over which slip evolves. For an asperity with stiffness above this critical value, slip will be stable even with velocity weakening frictional parameters. The actual stiffness of an asperity is

$$K = \frac{CG}{(1-\nu)L} \tag{3.3}$$

where G is the shear modulus, ν is the Poisson ratio, L is a characteristic slip dimension, and C is a coefficient close to one assuming a uniform stress drop. Equating the critical stiffness with the stiffness (Equations 2 and 3 above) gives a formulation for critical slip dimension, above which slip will be unstable. It is worth noting that high pore fluid pressure does not promote slip on small patches, as the minimum slip dimension is inversely proportional to σ_n, so lower effective stress calls for larger slip dimensions. The effective normal stress is, however, the most flexible parameter capable of varying by multiple orders of magnitude.

Unstable slip on small asperities in the presence of substantially elevated pore fluid pressure is still possible, but requires $\mathrm{K}_{crit} > \mathrm{K}$. While detailed source studies of LFE waveforms have not yet been performed, *Shelly* (2010) estimated between 0.25 and 0.5 mm of slip per episode in one particular family. If we assume average slip of 0.25 mm and a characteristic M_w of 1.6, then for a circular asperity we would expect a typical rupture dimension of ∼200 m, corresponding to a stiffness of 180 MPa/m assuming $\nu = 0.25$ and $G = 3 * 10^{10}$ Pa. For the critical stiffness, we fix $b-a$ to be 0.004, take a d_c value of 1 μm from *Marone and Kilgore* (1993), and use an effective normal stress value of 10^5 Pa, we find a critical stiffness value of

400 MPa/m which would allow unstable slip to occur on a typical LFE patch. If instead we use an effective normal stress of 10^4 Pa consistent with average values from Figure 3.13, then the patch stiffness is greater than the critical stiffness and unstable slip should not occur.

This back-of-the-envelope calculation could be improved in several ways, which may reconcile theory and observation. *Fletcher and McGarr* (2011) estimated moment magnitudes between 1.6 and 1.9 for eleven tremor events. If the larger magnitudes are representative, they would perhaps correspond to a larger slip dimension, reducing the patch stiffness to values below the critical value for our estimated normal stress values in Figure 3.13. Second, it is possible that LFEs within the same family actually correspond to slip on multiple asperities separated by distances below the spatial resolution of the location procedure. If this were true, the analysis related to Figure 3.13 may overestimate the pore fluid pressure. However, pore fluid pressure is likely still close to lithostatic as *Thomas et al.* (2009) analyzed a catalog of tremor envelopes made up of many constituent LFEs and still found near-lithostatic pore fluid pressure. Third, while variations in stiffness can be responsible for LFE production, it is worth noting that other factors can influence the transition between stable and unstable sliding. For example, *Gu et al.* (1984) point out that nominally stable regions can have unstable slip if loading rates are high. Finally, Equation 1 was derived using a model that considers the effect of sustained periodic loads on a stuck asperity on a slipping fault (*Dieterich*, 1987; *Beeler and Lockner*, 2003). We use this relationship because it seems to do well in describing tidal triggering of regular earthquakes (e.g. *Cochran et al.* (2004)) and it provides a means of estimating effective normal stress using seismicity rate variations. However, this model may not be applicable to many LFE families or to LFEs in general because it neglects the important effect of coupling between the tides and surrounding fault creep. If the effect of fault creep were considered, the effective normal stress values presented in Figure 3.13 could be revised upwards and hence represent a lower bound. While the specific values of effective normal stress are model dependent, high pore fluid pressure is one of the only mechanisms capable of explaining the extreme sensitivity of LFEs to small tidally-induced shear stresses and are likely present on the deep SAF. In the next two sections, we continue to discuss the application of the model behind Equation 1 to LFEs noting both when it succeeds and fails to predict our observations. In ongoing work, we are pursuing more detailed models of the influence of fault creep on LFE nucleation.

To summarize, we find effective normal stresses of $\sim$30 kPa near Parkfield using the response of LFEs to tidal stress perturbations. Elevated pore fluid pressures seem to be an omnipresent characteristic of NVT/LFE source regions, but low effective normal stress does not facilitate unstable slip on small asperities as reduction in effective stress can reduce the critical stiffness for seismic slip to below the asperity stiffness. Low effective stress may promote slow slip, however, which would generally explain why slow slip has been observed without NVT, but NVT has not been observed without slow slip. Parkfield is the notable exception as no surface deformation signal associated with tremor activity has been detected with existing instrumentation. However, *Smith and Gomberg* (2009) found that even M5 events at 15 km depth may not produce a geodetically detectable strain signal at the surface. Additionally, the correlated slip histories of a number of shallow families strongly suggests

that slow slip occurs in Parkfield (*Shelly*, 2009).

Implications for Frequency Dependent Response of LFEs

Why are LFEs so strongly correlated with tidal stresses while earthquakes are not? Theoretical and laboratory studies on tidal modulation of earthquakes were able to explain the weak, oftentimes ambiguous correlation of earthquakes with tides as resulting from the inherent time dependence of earthquake nucleation (*Lockner and Beeler*, 1999; *Beeler and Lockner*, 2003). *Beeler and Lockner* (2003) found that the amplitude of a given periodic stress, and its period relative to the nucleation timescale, governed by the in situ properties of the earthquake source region, dictate whether the stress perturbation is capable of modulating event occurrence. The duration of nucleation is defined as, $t_n = 2\pi a\sigma_n/\dot{\tau}$, where $\dot{\tau}$ is the stressing rate (*Beeler and Lockner*, 2003). The nucleation timescale represents the amount of time required for the slip velocity to evolve to seismic slip speeds and also defines the boundary between two frequency-dependent regimes of how earthquake failure time is influenced by sustained periodic stressing such as due to the solid Earth tides. In the low-frequency, long period regime (i.e., oscillatory stress period $> t_n$), events are effectively characterized by threshold failure because the nucleation timescale is much shorter than the period. Once the stress threshold is breached, earthquakes nucleate and occur immediately (with respect to the period of the loading function) and fault strength is effectively constant throughout the nucleation process. Events preferentially correlate with peak loading rates in this regime, as the greatest probability of being triggered occurs at times when stress is increasing fastest. In the high-frequency regime, nucleation times are long with respect to the period of the load, and the loading function controls the evolution of fault strength. Fault strength depends positively on slip rate, resulting in a higher probability of failure when stressing amplitude is positive. Laboratory experiments exploring the effect of increasing fluid pressure on t_n validate the proportionality between the two (*Bartlow et al.*, 2010).

Our observations of a first-order correlation with stress amplitude (high frequency regime) suggest tidal periods are shorter than the nucleation timescale for LFEs. Additionally, the effective stress calculation (Equation 1) inherently assumes a t_n greater than tidal periods (*Beeler and Lockner*, 2003). We determine if the observed correlation with amplitude is consistent with the Beeler and Lockner framework by computing the nucleation timescale for LFEs in Parkfield. We again let $a = 0.02$, relevant for hydrothermal conditions in the deep crust (*Blanpied et al.*, 1995), and use an effective normal stress of 10^5 Pa. We calculate a stressing rate by taking the product of the stiffness of a characteristic LFE asperity and the background fault slip rate V_l. Combining the 180 MPa/m stiffness calculated in Section 4.3 with the 33 mm/yr average deep slip rate estimate of *Ryder and Bürgmann* (2008), we find a value of t_n=$\sim$18 hours. Since this timescale is longer than the predominant 12.4 hour tidal period, the *Beeler and Lockner* (2003) model predicts that tidal stressing magnitude should modulate LFE rate consistent with our observations. It is worth noting that this value is much smaller than the nucleation time of > 1 year calculated by *Beeler and Lockner* (2003) for shallow earthquakes, which may be important for explaining the observed differences in

tidal triggering between earthquakes and LFEs.

While the *Beeler and Lockner* (2003) model is seemingly appropriate, there are a few additional factors that limit its general applicability to LFEs. First, while the above calculation is consistent with effective normal stresses of 10^5 Pa, using the average effective normal stress of 10^4 Pa from Figure 3.13 yields a t_n of ∼1.8 hours which would put LFEs into the threshold regime where a correlation with peak stressing rate, not stress amplitude, should be observed. One possible explanation for this contradiction is that effective normal stress estimates in Figure 3.13 are underestimates, as discussed in the previous section. Second, many LFEs, in particular those in the highly episodic families, have recurrence intervals less than the calculated nucleation time. This is likely due to the assumption that the stressing rate is constant and proportional to the plate velocity which is almost certainly untrue for the most episodic families as the highly variable inter-episode event rates suggest that the stressing rate is orders of magnitude higher during episodes than between episodes.

In summary, we find that previously theorized frameworks for earthquake nucleation in response to periodic loads are consistent with our primary findings that LFEs correlate with stress amplitude if the duration of slip nucleation for tremor is slightly larger than the tidal period. However, they may not be capable of explaining all of the observations associated with tidal triggering of LFEs, such as the weaker rate dependences and LFE repeat times that fall well below the calculated nucleation timescale.

Negative Shear-Stress Rate Dependence of Failure Times

There are multiple potential explanations for the approximately half hour phase shift in the distribution of failure times relative to the peak tidal shear stress described in Section 3.6. The majority of LFE families exhibit a correlation with negative dRLSS (Figure 3.4E) that does not appear to be due to correlation with other stress components (Figure 3.5). One possible source of this time delay is the tendency for LFEs to occur in multi-event episodes sometimes involving hundreds of events. Such episodes, if generally initiated at peak shear stress, may cause LFE activity initiated at a tidally optimal time to continue into a time that is less tidally favorable. However, if clustering is responsible for the bulk phase shift we would also expect a correlation between the tendency of an LFE family to cluster and phase shift. We note that the highly episodic, shallow families with relatively low RLSS N_{ex} values generally have insignificant correlation with dRLSS. Qualitatively there does not seem to be any correlation between the existence/magnitude of a phase shift and episodicity so clustering cannot be solely responsible for the observed phasing in all families.

Alternatively, the phase shift in Figure 3.11 may partially reflect how the background loading rate influences the timing of LFEs in response to the cyclical tidal load. We consider a simple threshold failure model for asperity strength with a stressing function consisting of a superposition of the background plate velocity plus a periodic load

$$\tau(t) = kV_l t + A\sin(2\pi t/t_w) \tag{3.4}$$

Where τ is the stress, and A is a constant amplitude and t_w the period of the cyclical load. In this failure model, LFEs can only occur when the stressing function exceeds some stress threshold. If the background stressing rate is larger than the maximum tidal stressing rate, the stressing function is monotonically increasing and LFEs can occur during all times of the tidal cycle. If the background loading rate and the peak tidal stressing rate are of comparable magnitude, LFEs can only occur once the stressing function has emerged from the stress shadow of the previous cycle during which the net loading rate becomes negative. In this case, for a constant background loading rate, the peak in the stressing function occurs slightly after the peak in the tidal stressing function alone (*Lockner and Beeler*, 1999). Since we measure LFE rates relative to only the tidal component, and not the overall loading function, it is possible that the slight phase delay is a manifestation of the magnitude of the background loading rate. If we let $A = 100$ Pa, the mean tidal shear stress amplitude, $t_w = 12.4$ hours, stiffness $k = 180$ MPa/m, and assume that the peak loading amplitude should correspond to peak LFE rate, we find that a loading velocity, V_l, three orders of magnitude smaller than the 33 mm/yr deep slip rate reported by *Ryder and Bürgmann* (2008) is required to match the half hour phase shift. Additionally, for constant V_l and tidal amplitude A, this model predicts that no LFEs should occur while the net loading rate is negative following each cyclical load peak, which directly contradicts our observations. However, tidal amplitudes are not constant and the episodic nature of most LFE families suggests that fault slip rates are highly variable. If these additional complexities were incorporated into Equation 4 above, then the model may be able to reproduce the observed phase delays (Figure 3.11), while also producing failure times at all phases but predominantly correlated with amplitude.

A third potential cause of the phase shift in Figure 3.11 could be fluctuations in tidally-induced normal stress. Our findings indicate that LFEs are most sensitive to RLSS however most families have a weaker, yet still significant correlation with FNS. Despite the fact that tides are primarily volumetric stresses and cause normal stress changes nearly an order of magnitude larger than shear stresses, neither of the studies that explore the dependence of earthquake failure times on periodic stress consider variations in normal stress (*Dieterich*, 1987; *Beeler and Lockner*, 2003). While constant normal stress is likely a reasonable assumption for shallow faults, the environments that are most likely to experience tidal modulation of earthquakes (i.e. where the effective confining stress is low) are also those where the fluctuations in normal stress induced by the tides are likely to have the greatest impact. An exploration of the characteristics of a model like that of *Beeler and Lockner* (2003) incorporating normal-stress fluctuations is beyond the scope of the current study. However, we speculate that normal stress oscillations may play an increasingly important role in the timing of slip in environments with substantially elevated pore fluid pressures.

Fault Geometry at Depth and Correlation of Tremor with Fault-normal Compression

While the 88 hypocentral locations are too sparse to map details of fault geometry to depth over the 160 km section of the SAF, the majority of locations seem to lie on one coherent fault strand with very few events deviating substantially from the mapped trace (Figures 3.1 and 3.10). The locations of the LFEs between Parkfield and Cholame closely follow a bend in the SAF surface trace suggesting a similar first-order geometry from the surface to near the base of the crust. This observation suggests that while some small amount of the total slip budget may be accommodated off-fault, tremor-producing deformation largely remains localized at depths up to 25 km, and the geometry of closely spaced hypocenters may reflect the geometry of the SAF at depth. If the majority of LFE hypocenters are on the fault, the similar morphology of both the LFE hypocentral locations and the mapped fault trace within the surface fault-bend region (Figure 3.10) suggests that the bend is preserved at depth.

The SAF fault geometry and localized deformation continue to depths well below the base of the seismogenic zone at temperatures and pressures that suggest that deformation should be by distributed ductile deformation (*Bürgmann and Dresen*, 2008). If near lithostatic pore fluid pressures are present in the LFE source region, they provide a potential mechanism for sustaining localized slip in the lower crust. Typically, deformation transitions between brittle and ductile at the depth that strength (differential stress) derived from Byerlee's law exceeds the strength from an Arrhenius-type flow law with parameters appropriate for the region of interest. If pore fluid pressure increases dramatically below the brittle-ductile transition, then brittle failure would remain the preferred mode of deformation as increased fluid pressures dramatically reduce the effective friction coefficient, lowering the differential stress required for brittle failure, and increasing the depth of the transition between brittle and fully ductile deformation.

Conventional models of crustal rheology suggest that below the brittle-ductile transition deformation delocalizes from a narrow fault zone to a wider zone of more distributed shear due to the onset of plasticity in the mineral constituents of the host rock (*Bürgmann and Dresen*, 2008). Exhumed mid-crustal shear zones along the Alpine fault in New Zealand (e.g. *Little et al.* (2002)) and the Liquine-Ofqui fault in Chile (e.g. *Cembrano et al.* (2002)) provide structural evidence of ductile flow between 20-30 km depth under pressure and temperature conditions that are likely similar to those on the deep SAF. These deep shear zones are generally characterized by mylonitic fabrics that are progressively overprinted by more localized regions of ductile shear, and then brittle faulting during exhumation. While exhumed faults do display evidence of ductile flow, one striking observation common to both of the examples is that the zone of distributed shear is relatively narrow: less than 5 km on the Liquine-Ofqui fault and 1-2 km on the Alpine fault and much of the deformation appears highly localized in even narrower ultra-mylonitic shear zones. These observations also suggest that deep, yet localized deformation on continental transforms may be more common than previously thought.

Local fault geometry may also provide a potential explanation for the correlation of a cluster of families with negative FNS (Figure 3.4 B). Figure 3.14 compares the strike of the SAF to the FNS N_{ex} values for all families. The dramatic change in strike between N43°W and N30°W occurs over a distance of ∼10 km on a section of the SAF in the Gold Hill region between Parkfield and Cholame (*Simpson et al.*, 2006; *Bilham and King*, 1989). The location of this releasing right bend, indicated in red, correlates well with the locations of negative FNS N_{ex} values. Further evidence for the bend at depth can be found in the optimal orientations for tidal correlation shown in Figure 3.11. If we compare the mean orientations for families with statistically significant negative values of FNS to those of the entire population we find that for both the $\mu = 0.0$ and $\mu = 0.1$ cases, orientations that maximize N_{ex} are rotated clockwise by an average of 4° and 8° respectively.

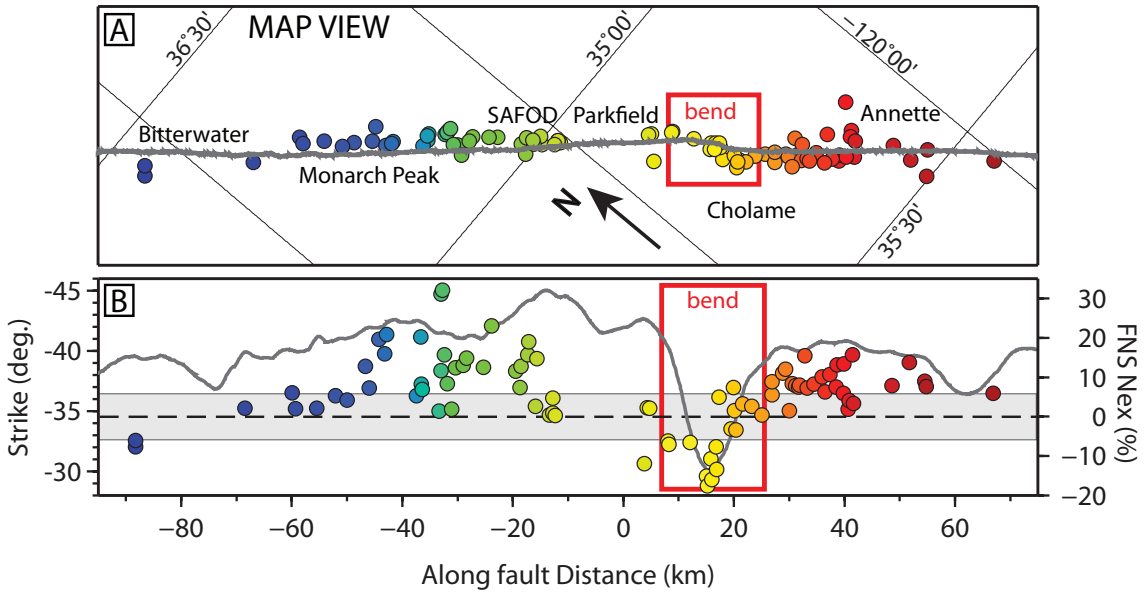

Figure 3.14: Panel A shows a rotated map view of LFE locations color-coded by family ID number as in Figure 3.1. The fault bend region is outlined in red to highlight the common morphology of the surface fault strike and the LFE hypocentral locations at depth. Panel B shows the mapped fault strike, dark gray solid line, in degrees west of north (left axis) derived from the strike in panel A as a function of distance along the fault. Colored circles correspond to families in panel A. Their vertical position, measured relative to the right axis, is their FNS N_{ex} value. Dark gray dashed line marks the zero FNS N_{ex} value with 99% confidence intervals indicated in light gray.

The presence of the fault bend at depth may also relate to the mechanically implausible correlation with clamping of a number LFE families (Figure 3.4B, negative FNS families). In conventional frictional failure models, earthquakes should preferentially occur during times of reduced fault-normal stress making this a surprising finding. The hypothesis testing

results discussed in Section 3.2 indicate that the significant negative FNS values are not an artifact of correlation with another stressing function (see families 41, 44, 45, and 49-57 in Figure 3.5). As each LFE family is analyzed as an independent data set and all families are compared to the same stressing functions the spatial concentration of the families with negative N_{ex} values also supports the hypothesis testing results.

Evidence for Evolution of Effective Contact Area

In Section 4.3, we appealed to near-lithostatic values of pore fluid pressure to explain the robust sensitivity of LFEs to tidally-induced RLSS and the relatively low to insignificant FNS N_{ex} values. While this framework is consistent with our observations of tidal triggering in most families, it cannot explain the robust correlation of several families with both tensile FNS and RLSS. These families, labeled positive FNS families in Figure 3.4 B, are somewhat paradoxical in that they have RLSS N_{ex} values of $\sim$30% indicative of elevated pore fluid pressures, yet they also have FNS N_{ex} values of $\sim$25%, suggesting that the fault may no longer be desensitized to normal-stress changes. However, if the fault is once again sensitive to normal stress, then how is it possible for it to feel the effect of small RLSS changes in the presence of an overburden pressure of hundreds of megapascals?

One potential mechanism for this may be the evolution of the real area of contact across the fault with depth. *Scholz* (2002) suggested an effective stress law for friction of the form

$$\sigma_n = \sigma - (1 - A_r/A)p \tag{3.5}$$

where A_r is the area of contact in the fault zone, A is the total area of the fault, σ is the applied normal stress, and p is the pore fluid pressure. The $\alpha = 1 - A_r/A$ factor measures the sensitivity of effective stress to pore pressure and reflects the influence of fault topography. When two surfaces with roughness are put in contact, they physically touch on contact points known as asperities. At low normal stress such as for shallow fault zones, the sum of the areas of all these asperities (A_r) is generally only a very small fraction of the total fault area (A), so if $A_r << A$, the effective normal stress can be approximated as the normal stress minus the pore fluid pressure. As depth increases, the real area of contact increases, and asperities within the fault zone bear a progressively larger fraction of the load. Thus for shallow faulting α is near one and the effective stress is determined by how effectively changes in pore fluid pressure can buffer changes in applied stress. In a similar model, *Hawthorne and Rubin* (2010) found that for reasonable choices of parameters, the change in pore fluid pressure was greater than 90% the change in applied normal stress. At great depths where rocks begin to deform ductily, α tends toward zero, and effective stress becomes insensitive to the absolute level of pore pressure. Accordingly, if the pore pressure between the base of the seismogenic zone and the Moho is nearly lithostatic, as suggested by the dramatic effect small magnitude shear stresses have on LFE occurrence, families that correlate with FNS at depth would be those in regions where the real area of contact approaches the entire fault area.

Figure 3.15 is a schematic diagram showing the influence of both near-lithostatic pore fluid pressure and changes in effective contact area on crustal strength. The colors correspond to different layers representing the brittle section of the crust which extends between the surface and 15 km, the transition zone between 15 and 30 km depth, and a nominally ductile region below the Moho at ∼30 km depth. We have no direct constraints about the nature or degree of localization of deformation in the upper mantle below Parkfield, but postseismic deformation studies across the western US suggest that upper mantle deformation is by distributed ductile flow in a hot and hydrated asthenosphere (*Bürgmann and Dresen*, 2008). In the left panel in Figure 3.15, we specify a pore fluid pressure profile that transitions from hydrostatic to near-lithostatic at the top of the transition zone, consistent with our inferences in Section 4.3. On the basis of laboratory experiments *Dieterich and Kilgore* (1996) argue that A_r/A increases linearly and is approximately equal to the effective normal stress divided by the indentation hardness of the material. If we assume a quartz indentation hardness of 12,000 MPa (*Dieterich and Kilgore*, 1994), α should decrease linearly between one at the surface to around 0.97 at the top of the transition zone as shown in the central panel of Figure 3.15. The shape of the α curve within the transition zone is largely speculative, as there are few laboratory studies of frictional behavior or effective contact area under pressure and temperature conditions approaching those in the environments that host LFEs. However, we expect that as temperature increases contact area will rapidly increase as thermally activated creep mechanisms increasingly help accommodate rock deformation.

The right panel in Figure 3.15 shows a hypothetical crustal strength profile incorporating near-lithostatic pore fluid pressures and changes in effective contact area shown in the left and central panels. Frictional strength within the brittle, seismogenic zone increases with pressure and depth in accordance with Byerlees law. At the top of the transition zone, pore fluid pressures transition between hydro-and lithostatic causing a drastic reduction in strength. While brittle failure is the preferred mode of deformation within the transition zone, as evidenced by the existence of LFEs, the specific deformation mechanism at the top of the transition zone is determined by the depth and degree of pressurization. If the transition between hydro and lithostatic pore pressure takes place above the intersection between the frictional strength envelope and the flow law derived using appropriate parameters (strain rate, material properties, etc.) then frictional failure, rather than flow, is likely the dominant deformation mechanism between the surface and the deep transition zone. Within the transition zone near-lithostatic pore fluid pressures make frictional failure dominant until changes in α become significant. As α approaches zero, the fault becomes sensitive to progressively larger fractions of the applied normal stress until the frictional failure is no longer preferred as frictional strength exceeds that of an olivine flow law for the upper mantle. Considering the effects of both near-lithostatic pore fluid pressures and increases in contact area with depth can potentially explain both the statistically significant RLSS N_{ex} values in all families and the subset of deep families that robustly correlate with both shear and normal stresses. High pore fluid pressure also provides a mechanism for sustaining localized, rather than distributed, deformation down to 30 km depth consistent with the discussion in Section 4.6.

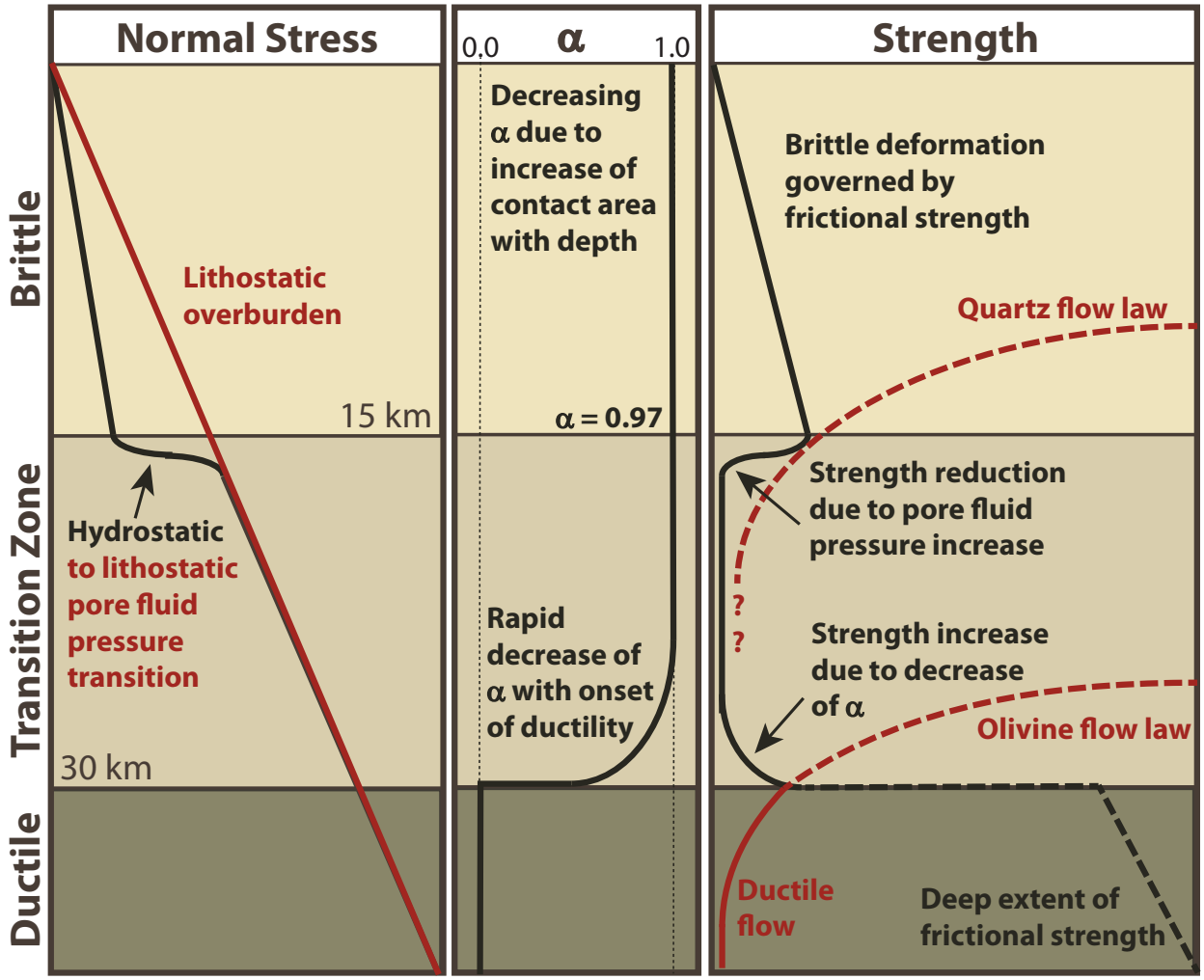

Figure 3.15: A schematic diagram of normal stress, effective contact area, and strength as a function of depth.

3.5 Conclusions

The suite of recently identified fault slip behaviors such as episodic slip, slow slip, non-volcanic tremor (NVT), and low frequency earthquakes (LFEs) complicate idealized models of how faults accommodate deformation (*Ide et al.*, 2007; *Peng and Gomberg*, 2010). We exploit the extreme sensitivity of LFEs to small stress perturbations to elicit information about the in-situ properties of LFE source regions within the brittle-to-ductile transition.

We map the spatially heterogeneous sensitivity of LFEs to tidally induced fault-normal stress, right-lateral shear stress, and their time derivatives along a 160 km span of the SAF near Parkfield, CA extending from 16 to 30 km depth. We find that LFEs are most strongly influenced by RLSS with a surplus of LFEs occurring when the tides are promoting slip on the fault. Some families also have significant sensitivity to both positive and negative FNS. The families that correlate with extension generally occur deep in the creeping section, and their correlation may be a manifestation of the increase in effective contact area with depth. Families that correlate with fault normal clamping are spatially localized and coincide with a right-stepping fault bend evident in the surface fault trace. If the change in fault geometry is responsible for the anomalous correlations, it would argue that the San Andreas remains localized to depths near the Moho and that large scale ($\sim$10 km) fault morphology present at the surface is also preserved at depth.

The incontrovertible correlation of high pore fluid pressures and slow slip across tectonic environments suggests a causative relationship between the two. Our analysis suggests low effective stress is required to produce the robust response of LFEs to the tides. It is worth noting, however, that high pore fluid pressures do not facilitate LFE production as decreasing effective stress requires increasing source dimensions to host unstable slip, making unstable slip on small asperities more difficult. The recurrence characteristics of LFEs are some of the few observational constraints illuminating the style of deformation in deep fault zones. We also find a first-order correlation between deformation style and tidally induced RLSS, as highly episodic, shallow families generally have smaller RLSS N_{ex} values than the deeper, continuously deforming families.

The duration and style of loading, and the timing of earthquakes relative to the application of a load is of considerable interest to those studying the roles of static and dynamic stresses in earthquake triggering and the mechanical implications of those observations. We find that the timing of LFEs with respect to tidally induced stresses is consistent with some aspects of a previously proposed model of earthquake triggering in response to tidal loading (*Beeler and Lockner*, 2003). There are, however, some inconsistencies such as recurrence times less than the computed LFE nucleation time, failure times that correlate with stressing rate, and the neglected effect of fault creep that limit general applicability of the *Beeler and Lockner* (2003) model.

A second order dependence on dRLSS is also present in the phases of triggering times relative to the tidal load. A statistically significant number of LFEs trigger preferentially when RLSS magnitude is positive but decreasing. A number of possible causes could potentially explain the phase shift, including clustering, superposition of the background plate

rate and the tidal load, or the weak influence of normal stresses that were not considered in previous models. While our data cannot resolve if slip events in Parkfield are triggered by the tides, the population of events that initiate a slip episode on a particular asperity are tidally correlated, suggesting that tidal forces play a role in slip front propagation speeds, and/or the onset of slow slip pulses is comparable to tidal timescales.

Chapter 4

Inferring fault rheology from low frequency earthquakes on the San Andreas fault

4.1 Introduction

Deep slip in some subduction zones is accompanied by long duration seismic signals with highest signal-to-noise ratios in the ∼2-8 Hz band similar frequency to volcanic tremor. Being associated with plate boundary faults, this seismicity is often referred to as tectonic or non-volcanic tremor (NVT) (*Obara*, 2002). The seismic moment of the tremor is a tiny fraction of the total moment of the deep slip (*Kao et al.*, 2010). In Japan and elsewhere some of the tremor is located very near the inferred position of the subduction megathrust fault that is assumed to be the locus of slip. *Shelly et al.* (2007a) argued that at least part of the tremor signal is generated by slip on small on-fault asperities and showed that individual repeating low-frequency earthquakes (LFE) make up a portion of the tremor. Focal mechanism inversions of LFEs in Shikoku Japan indicate that they are generated by shear slip in an orientation consistent with the plate boundary (*Ide et al.*, 2007). Other studies elsewhere have reported intraplate NVT locations (*Kao et al.*, 2005), and tremor location relative to the presumed fault plane remains somewhat controversial. Nevertheless, a simple and popular conceptual model for LFEs is that they represent radiation emanating from small, persistent regions that repeatedly fail during aseismic shear of the larger-scale surrounding fault zone *Shelly et al.* (2007a). In the present paper we implement a quantitative version of this model to study the sensitivity of NVT to imposed changes in stress.

Non-volcanic tremor *Nadeau and Guilhem* (2009) and LFEs extracted from the tremor (*Shelly and Hardebeck*, 2010) also occur on the deep San Andreas fault (SAF). It is these LFEs that are the topic of the present paper, and we use aspects of their occurrence and rate of occurrence to constrain the rheology that controls aseismic fault slip in the source region. The LFEs locate between 16 and 29 km depth. Unlike in subduction zones, NVT and

associated LFEs on the San Andreas are not associated with geodetically detectable episodes of transient rapid fault creep. However, tremor on the SAF is episodic at shorter recurrence intervals and is distributed over smaller regions. SAF tremor recurrences range from days to months, compared with 6-15 months for subduction zones with geodetically detectible slip. Furthermore NVT / LFE rates show other evidence of being associated with deep slip such as spatio-temporal propagation (*Shelly*, 2009), narrow alignment (*Shelly and Hardebeck*, 2010) and accelerated occurrence rates from the 2004 Parkfield earthquake (*Shelly and Johnson*, 2011). Thus, despite a lack of geodetically detectable transient slip, NVT and LFEs on the SAF are thought to be the seismic manifestation of deep, largely aseismic slip in the region (*Thomas et al.*, 2009).

One characteristic common to observations of NVT and LFEs in subduction zones and on the SAF that distinguishes them from shallow seismicity is sensitivity to small stress perturbations. Studies of static stress changes from regional earthquakes report both an aftershock-like response of deep NVT and LFEs on the SAF to increases of 6 and 10 kPa in shear stress from the 2003 M_w 6.5 San Simeon and the 2004 M_w 6.0 Parkfield earthquakes respectively, and quiescent response to decreases in failure stress (*Nadeau and Guilhem*, 2009; *Shelly and Johnson*, 2011). Several studies report triggering of NVT and LFEs on the SAF and elsewhere by teleseismic surface and body waves that imposed stress transients as small as a few kilopascals (*Gomberg et al.*, 2008; *Miyazawa and Brodsky*, 2008; *Peng et al.*, 2009; *Hill*, 2010; *Ghosh et al.*, 2009; *Shelly et al.*, 2011). Additionally, studies of tidal stress perturbations conclude that NVT and slow slip itself are sensitive to stress changes as small as fractions of a kilopascal (*Rubinstein et al.*, 2008; *Nakata et al.*, 2008; *Lambert et al.*, 2009; *Thomas et al.*, 2009; *Hawthorne and Rubin*, 2010).

4.2 Laboratory models of tidal triggering

Unlike NVT, many large, shallow earthquake catalogs have little or no statistically significant relationship between earthquake occurrence and tidal forcing *Knopoff* (1964); *Heaton* (1982); *Vidale et al.* (1998); *Métivier et al.* (2009). To explain this relation between the solid earth tides and earthquake occurrence, following *Dieterich* (1987), *Lockner and Beeler* (1999) and *Beeler and Lockner* (2003) conducted a series of laboratory friction experiments, extrapolated those to natural conditions and argued that the tides and earthquakes are correlated but at a very low level, thus, providing an explanation why catalogs with very large event numbers are required to detect the correlation. The essential physical property of rock failure and friction that will prevent strong correlation between the tides and earthquakes is that the onset of rapid slip follows a long characteristic delay time. As a result, small amplitude stress changes that are much shorter duration than the delay time have essentially no effect on the time of failure. This connection between delayed failure in rock mechanics tests and earthquake occurrence was first recognized by *Knopoff* (1964).

There are three predictions of this lab-based failure model that can be tested for earthquakes, including NVT and LFEs:

1. Events are expected to occur at all phases of the tides with maximum rate of occurrence coincident with maximum in the tidal stress (*Dieterich*, 1987; *Lockner and Beeler*, 1999), and therefore can the thought of as in phase with the tidal stress.

2. For the tides resolved onto a fault as shear stress in the direction of slip, the degree of correlation with continuous periodic stressing increases non-linearly as the ratio of the amplitude of the tidal shear stress to the effective normal stress increases (*Dieterich*, 1987; *Beeler and Lockner*, 2003).

3. The characteristic delay time of failure is proportional to the effective normal stress and inversely proportional to the stressing rate (*Dieterich*, 1987; *Beeler and Lockner*, 2003).

With regard to prediction 1, in a normal faulting environment, the Endeavour segment of the Juan de Fuca mid ocean ridge, *Wilcock* (2001) found the maximum earthquake occurrence rate coincident with the maximum extensional tidal stress. Similarly, *Cochran et al.* (2004) examined the relation between earthquake occurrence and phase of the tidal stress and found the maximum rate of occurrence of shallow subduction thrust events coincided with the tidal maximum. NVT or LFEs in the Nankai and Cascadia subduction zones and on the SAF occur at all phases of the tides (*Rubinstein et al.*, 2008). Furthermore, *Lambert et al.* (2009) found that the peak tremor activity coincides with maximum tidal shear stress resolved onto the subduction interface in Cascadia. Slow slip in Cascadia is also in phase with the NVT (*Hawthorne and Rubin*, 2010) but the relation to tidal stress is ambiguous due to uncertainty in the location of deep slip; their comparison between slip and the tides concludes that the phase of maximum strain rate in daily tidal period may occur at the maximum shear stress or up to 90° before it.

Similar modulation occurs in the Shikoku subduction zone of southwest Japan (*Shelly et al.*, 2007b; *Nakata et al.*, 2008) and tremor occurs at all phases of the tides. (*Nakata et al.*, 2008) found that the tremor occurrence rate is well represented by a delayed failure model they compared tremor with predictions using the seismicity rate equations from *Dieterich* (1994), given calculated theoretical tides in Shikoku. In both Nankai and Cascadia high fluid pressures are inferred from the high V_p/V_s ratios in the NVT source region, as documented by *Shelly et al.* (2006) and *Audet et al.* (2009), and have been invoked to explain correlation of NVT with small stress perturbations. On the San Andreas fault in California NVT and LFEs (*Thomas et al.*, 2009, 2012) occur at all phases of the tides and the rate of occurrence coincides with the maximum tidal shear stress, as discussed in greater detail below.

Observational studies substantiate prediction 2) that in regions of especially high tidal stress amplitude a correlation of earthquakes with the tides is easier to detect, most notably *Wilcock* (2001) and later *Cochran et al.* (2004). *Wilcock* (2001) was motivated to look for tidal triggering of earthquakes in a mid-ocean ridge environment because ocean tidal stress can reach 10s of kPa as opposed the solid earth tides which are limited to a few kPa. *Wilcock* (2001) found a strong tidal correlation in a data set with only ∼1500 events whereas in typical seismic catalogs of this size and much larger, there is no statistical correlation between the

solid tides and earthquakes *Vidale et al.* (1998); *Métivier et al.* (2009). *Wilcock* (2001) idea was later exploited by *Cochran et al.* (2004) who found a robust correlation between tidal stress and earthquakes in shallow subduction environments where the ocean tidal loads can be as large as 10 kPa and the confining stress is relatively low.

4.3 Tidal modulation of tremor on the San Andreas

In contrast to shallow earthquakes which, to reiterate, are quite insensitive to the tides except in cases of high tidal amplitude, NVT and LFEs on the San Andreas are extremely sensitive to tidally induced shear-stress changes with peak-to-peak amplitudes less than 0.5 kPa (*Thomas et al.*, 2009, 2012). In Figure 4.1A, LFEs from 4/2001 to 2/2012 are binned according to the tidal right lateral shear stress on the SAF at the time of occurrence. The number of events in each bin (N_{obs}) are normalized by the expected number of events (N_{exp}) assuming LFEs are randomly distributed in time. The expected number is the total number of events in the catalog divided by the total amount of catalog time at that bins range of tidal stress. Thus, values of $N_{obs}/N_{exp} > 1$ denote an excess of LFEs at that stress level, and values < 1 indicate a deficit. There is a clear systematic variation of event occurrence rate from low but non-zero at the lowest tidal stresses to high at the highest stress. NVT on the SAF shows the same relationship (*Thomas et al.* (2012, Figure 3)). In contrast, NVT shows no strong or systematic relationship with the tides resolved as normal stress on the SAF (Figure 4.1B). Because the solid earth tidal strains are largely volumetric, the amplitude of the normal stress tide is more than ten times larger than the shear stress. That there is no strong normal stress effect is surprising but the absence may provide an additional constraint on faulting rheology.

Because NVT and LFEs at Parkfield occur at all shear stress levels, are in phase with the tidal shear stress, the degree of correlation is high and the triggering shear stresses are very low, for these collective observations to be explained by the lab-based model described above requires low effective stress. However, calling upon arbitrarily low effective stress presents a problem for this model and it fails in a rigorous application to LFEs on the SAF (*Thomas et al.*, 2011, 2012). The problem arises from satisfying both predictions 2 and 3 at low effective stress. Since the delay time decreases with effective normal stress there is a limit to how low the effective pressure can be for failure to be delayed. To produce the strong correlation seen on the deep SAF at 0.4 kPa shear stress, the effective stress has to be so low that the delay time constant is of the order of the tidal period or shorter. Under those circumstances and natural rates of tectonic loading, earthquake occurrence is not delayed, will not occur at all phases of the tides, correlates with stressing rate rather than stress and therefore is not in phase with the tidal stress *Beeler and Lockner* (2003). It is unknown at present whether this lab model also fails to explain tidal modulation of NVT in Cascadia and elsewhere.

In this study we develop an alternative model to quantitatively explain the correlation between LFEs and NVT and the very low amplitude shear tides resolved onto the SAF

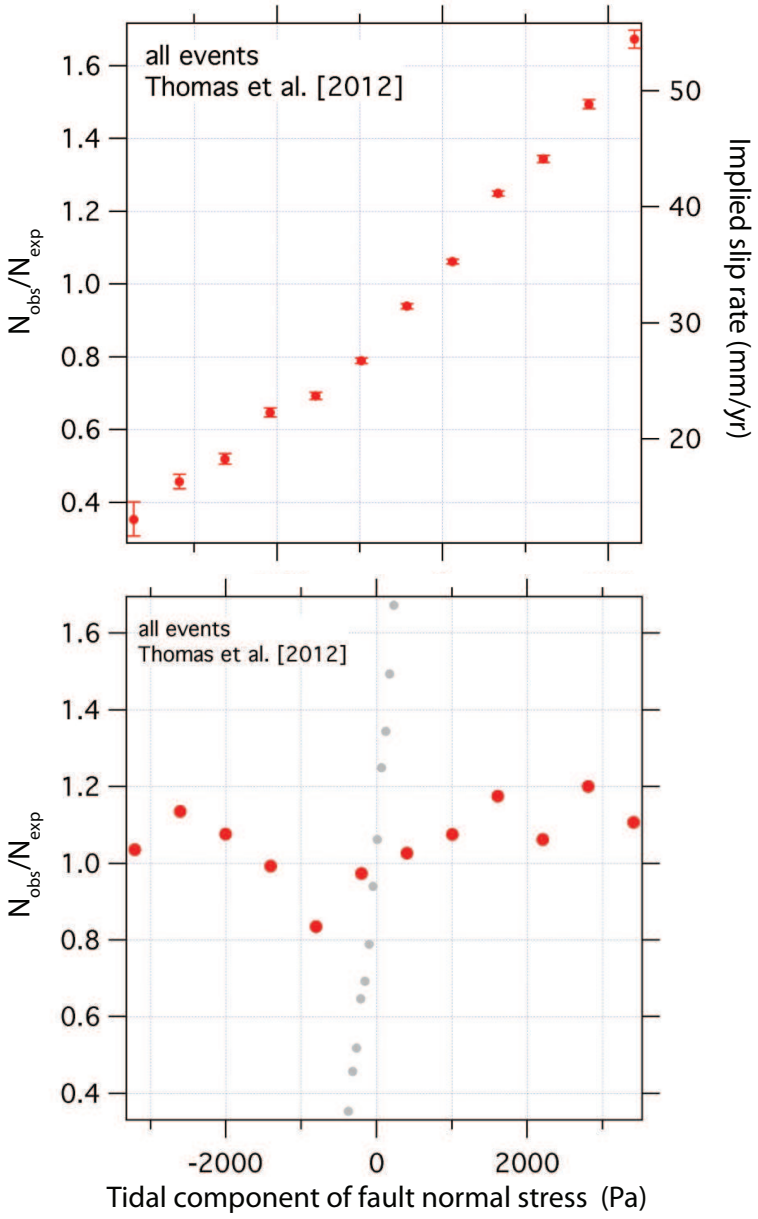

Figure 4.1: Relationship between earthquake occurrence and the tidal shear stress from *Thomas et al.* (2012) for ∼500,000 events in 88 LFE families. In panel A the left vertical axis is the observed number of events normalized by the expected number. The error bars are the 99% bootstrap confidence intervals. Horizontal axis is the tidal shear stress. The right axis shows the implied slip rate provided equation 4.5d is appropriate and that the nominal creep rate is the plate motion rate, 33 mm/year. Panel B is similar to panel A for fault normal stress. The shear stress data from panel A are shown as small grey symbols.

at Parkfield and to determine the rheology of fault slip in the source. We use a version of the model of *Shelly et al.* (2007a) described in the first paragraph of the Introduction above. This model has a history in earthquake fault mechanics that precedes the discovery of non-volcanic tremor, in particular, application to repeating earthquakes in the shallower creeping section of the San Andreas near Parkfield (*Nadeau and Johnson*, 1998). For this model it has been shown that earthquake rates (e.g., recurrence intervals, aftershock rates), rather than reflecting some intrinsic property of the earthquake source, can instead reflect the rate of aseismic creep of the surrounding fault (*Nadeau and Johnson*, 1998; *Perfettini and Avouac*, 2004). As we show in a quantitative implementation in the following section, if LFE sources cover a small fraction of the otherwise aseismically creeping deep SAF, then their tidal modulation measures the modulation of the surrounding creep rate and, given knowledge of the driving tidal stress changes, can be used to determine whether particular mechanisms of fault creep (e.g., dislocation creep, low temperature plasticity) are physically plausible. What we find is that for all possible creep mechanisms for fault slip rate to be significantly altered by small shear stress perturbations, the ambient shear resistance has to be of similar magnitude as the perturbation this finding precludes a majority of the possible mechanisms as their creep strengths are much higher than kPa or 10s of kPa.

While the model explains the relationship between the tidal shear stresses and LFE occurrence on the San Andreas, that explanation is limited to the average behavior of LFEs and NVT depicted in Figure 4.1A and in Figure 4.3 of *Thomas et al.* (2009). That is, Figure 4.1B is a histogram of ∼550,000 individual events from 88 different families. Single families show behaviors that can be significantly different than the average, notably, a phase lag between the peak tidal shear stress and the maximum rate of occurrence *Thomas et al.* (2012) that may be process symptomatic [e.g., *Ader et al.* (2012)]. There are also spatial variations in tidal sensitivity. These and other differences from the average sensitivity are not addressed in the present study. We also attempt to use the model to qualitatively explain why the average LFE and NVT occurrence (Figure 4.1B) are not strongly influenced by the much larger tidal normal stress resolved onto the SAF. Again, there are some LFE families that show systematic correlation with normal stress not evident in the collective, and not addressed in the present study.

4.4 Model of deep fault slip and NVT

According to *Shelly et al.* (2007a) model an LFE is a brittle patch on a fault plane that is elsewhere and otherwise creeping (Figure 4.2). This representation has been used previously to formally relate how fault creep might trigger earthquakes in a number of settings, e.g., shallow earthquake recurrence (*Bufe et al.*, 1977; *Nadeau and Johnson*, 1998) and aftershocks (*Perfettini and Avouac*, 2004), as well as non-volcanic tremor in subduction zones in Japan (*Shelly et al.*, 2007a) and in California (*Ader et al.*, 2012). As shear stress has the strongest influence we consider it in the greatest detail in this section. Constraints from normal stress are discussed briefly and separately in a subsequent section.

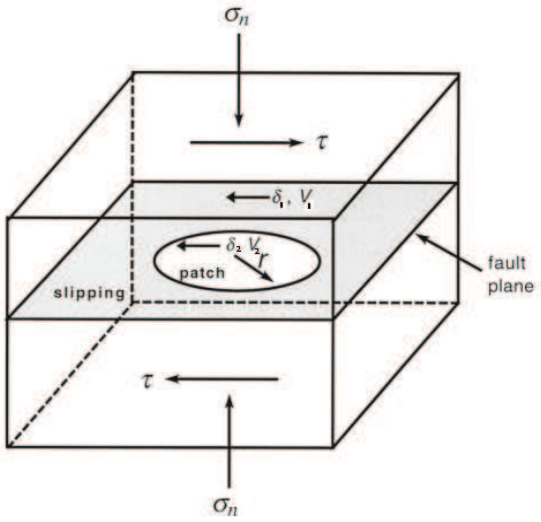

Figure 4.2: Assumed geometry of a low frequency earthquake source: a circular seismic patch of radius r embedded in an elsewhere aseismically creeping fault plane. Slip and slip velocity of the creeping fault surrounding the patch are δ_1 and V_1 , respectively. The slip and slip velocity of the patch are δ_2 and V_2, respectively.

Tidal shear stress

The fault plane surrounding the patch is subject to tectonic loading and stress from other sources, in this case from the tides,

$$\tau = \tau_{tectonic} + \tau_{tides} \tag{4.1a}$$

where we have assumed constant normal stress. Throughout we use a slider block model where shear stress on the fault plane from tectonic loading is

$$\tau_{tectonic} = k(\delta_L - \delta_1) \tag{4.1b}$$

k is the stiffness (MPa/micron) of the entire fault that surrounds and includes the patch, δ_L is the loading displacement, and δ_1 is slip of the fault plane. The tectonic loading displacement accrues following the nominal plate rate $\delta_L = V_L t$. We use a simple oscillating component intended to represent the solid earth tides, the oceanic tides or some other periodic source with shear stress amplitude $\Delta\tau$ and period t_w,

$$\tau_{tides} = \Delta\tau \sin\left(\frac{2\pi t}{t_w}\right) \tag{4.1c}$$

Accordingly, the total shear stress on the fault plane is

$$\tau = k(\delta_L - \delta_1) + \Delta\tau \sin\left(\frac{2\pi t}{t_w}\right) \tag{4.1d}$$

Here δ_1 is slip on the fault plane.

We are unsure whether fault creep at these depths is controlled by rate dependent friction, by crystal plasticity, pressure solution, or some combination of processes, and we look to the observations for constraints on the rheology. Thus, for the time being we consider a non-specific viscous fault zone, meaning, one whose strength increases with increasing strain rate or slip speed; equivalently one whose strain rate or slip speed increases if the ambient stress or the tidal component of shear stress increases,

$$V = f(\tau, \sigma). \tag{4.2}$$

Patch failure criteria

A simple implementation of a brittle patch rheology is to assume that it has a completely passive response to the imposed stresses and its failure strength has no dependence of any kind, in particular, no rate, time or slip dependencies. For laboratory-based models this is expected at high stressing rates where it has been shown that the characteristic delay time of rock friction (*Dieterich*, 1992, 1994) is short relative to the tidal period [e.g., *Beeler and Lockner* (2003)]. We use a threshold failure relationship, that is, the patch is completely locked until it fails at a particular level of stress. The patch is loaded by tectonic loading, by slip of the surrounding portion of the fault and by the imposed oscillating stress representing the tides

$$\tau_2 = k\delta_L + k_2\delta_1 + \Delta\tau \sin\left(\frac{2\pi t}{t_w}\right), \tag{4.3}$$

where k_2 is the patch stiffness. For a circular patch, $k_2 = 7\pi G/16r$, where G is the shear modulus. τ_2 and δ_2 are the stress on the patch and patch slip, respectively. Equivalently the stressing rate for the patch is

$$\frac{d\tau_2}{dt} = kV_L + k_2 V + \frac{2\pi\Delta\tau}{t_w} \cos\left(\frac{2\pi t}{t_w}\right). \tag{4.4}$$

Contrasting the two velocities in (4), V_L is plate rate, which is specified, whereas V is the slip rate of the fault surrounding the patch. V is stress dependent and will depend on the particular creep rheology assumed. Because there are three sources of stress loading the patch, it is not a passive meter of the slip rate of the surrounding fault as has been tacitly assumed [e.g., *Shelly et al.* (2007a) and *Ader et al.* (2012)], except under special circumstances, as follows.

Tremor rate

For threshold failure at constant normal stress the failure rate is proportional to the shear stressing rate, provided the stressing rate is positive (*Lockner and Beeler*, 1999). For convenience and following ideas from *Dieterich* (1987), *Dieterich* (1994), and *Lockner and Beeler* (1999), here, the seismicity rate R is defined relative to the background rate and for our model, the stressing rate

$$\frac{R}{R_L} = \frac{\dot{\tau}}{\dot{\tau_L}} = \frac{k}{k+k_2} + \frac{k_2 V}{(k+k_2)V_L} + \frac{2\pi\Delta\tau}{t_w(k+k_2)V_L}\cos\left(\frac{2\pi t}{t_w}\right). \tag{4.5a}$$

Here, we have defined a reference "background seismicity rate" R_L as associated with the constant stressing rate from tectonic loading the patch and driving creep of the surrounding fault at the plate rate. With reference to the normalized rate defined by (5a), recall that the data shown in Figure 4.1 define a histogram of earthquake occurrence for all events within all 88 LFE families identified on the deep SAF by *Thomas et al.* (2012). The Figure 4.1 vertical axis is N_{obs}/N_{exp}, the actual number of events observed over the corresponding range of $\Delta\tau$, normalized by the expected number. Given that there is a particular duration of time spent at each stress range, the ratio of number of events N_{obs}/N_{exp} is equivalent to the corresponding ratio of earthquake rates R/R_L over the time same range. Thus, $N_{obs}/N_{exp} = R/R_L$ as given by equation 4.5a.

To determine the relative sizes of the three terms on the right hand side of (5a), first consider the case where the surrounding fault is creeping at the plate rate V_L

$$\frac{R}{R_L} = \frac{\dot{\tau}}{\dot{\tau_L}} = 1 + \frac{2\pi\Delta\tau}{t_w(k+K_2)V_L}\cos\left(\frac{2\pi t}{t_w}\right) \tag{4.5b}$$

.

The maximum contribution to the earthquake rate from the direct tidal stress, the second term on the right-hand side (RHS) of (5b), is the coefficient of that term. A requirement for the observed tremor occurrence to predominantly reflect the rate of fault creep and tectonic stressing, rather than those components and direct stressing from the tides is then

$$V_L \gg \frac{2\pi\Delta\tau}{t_w(k+k_2)} \tag{4.5c}$$

.

The observations suggest the above requirement is met for LFEs on the deep SAF. NVT *Thomas et al.* (2009) and LFE occurrence *Thomas et al.* (2012) are in-phase with the tides for the shear stress resolved onto the SAF (Figure 4.1), meaning that for the shear stress component of the tides, the highest stresses are associated with the highest rates of earthquake occurrence. Because earthquake occurrence from the direct stressing from the tides themselves for a threshold failure model should follow the stressing rate and be 90° out of phase with the tidal stress (*Lockner and Beeler*, 1999), the observations suggest that direct stressing is not important.

That direct stressing from the tides is not an important LFE trigger is consistent with tremor source dimensions estimated by *Kao et al.* (2010) in Cascadia, as follows. In equation 4.5c, the RHS becomes larger as the sum of stiffnesses, of the surrounding fault and the fault patch, $k + k_2$, decreases. As $k_2 > k$, we can estimate the upper bound on the patch size that satisfies (5c) by ignoring k. *Kao et al.* (2010) found a radius of 13-30 m for M_w 2 and 1.5 tremor sources in Cascadia using a method that matches tremor amplitude to the amplitude of synthetic S-waves, calibrated using local earthquakes. For a patch radius of 50 m and a tidal shear stress of 0.4 kPa the quantity on the RHS of (5c) is ∼2.2 mm/yr. Since that is less than one tenth of the long-term SAF slip rate (30-35 mm/yr) implies that (5c) is an appropriate approximation. However, using a more traditional method to determine earthquake source properties, *Fletcher and McGarr* (2011) estimate the radius of NVT sources on the SAF to be 200 to 560 meters, in which case (5c) would not be met. Note that both *Fletcher and McGarr* (2011) and *Kao et al.* (2010) estimates are for tremor bursts rather than individual LFEs, and presently the validity of assumptions (5c) for LFEs is not constrained by data.

Similarly, whether or not tectonic loading or fault creep dominates LFE stressing depends on the stiffness (size) of the patch relative to the surrounding fault. If we assume that each of the 88 LFE sources are isolated then the representative stiffness, $k_2 = 7\pi G/16r$, for r = 50 m is 27.5 G/km. The LFEs are distributed within a region 140 x 15 km. Using a representative length of 46 km and dividing that by 88 we find a representative stiffness $k = G/(1-\nu)L$ for the fault surrounding each patch of 2.6 G/km. We therefore expect that even for patches as large as 100 m diameter that fault slip rather than tectonic loading dominates the stressing rate. Indeed, then we have one of the principal implications of this model as applied to small LFEs on the deep SAF,

$$\frac{R}{R_L} = \frac{\dot{\tau}}{\dot{\tau_L}} = \frac{N_{obs}}{N_{exp}} \approx \frac{V}{V_L} \tag{4.5d}$$

[also see *Ader et al.* (2012)], and Figure 4.1 can equivalently be expressed as a plot of the fault creep rate. For this special case of equation 4.5a, the fault patches that produce seismicity have an occurrence rate that directly reflects the rheological properties of the surrounding fault that determines its response to stress changes.

If this is an appropriate model for deep LFEs on the SAF, we find that the tides seem to modulate the plate rate by approximately 75%. Inherent in this model-dependent inference based on our interpretation of the earthquake rate is that the LFE patch size is 100 meters or less, on the low end of prior estimates from tremor bursts on the SAF and elsewhere (*Fletcher and McGarr*, 2011; *Kao et al.*, 2010). Also, while equation 4.5d was derived from consideration of a perfectly periodic tidal stress, so long as (5c) and $k_2 \gg k$ are met, (5d) is general and can be applied regardless of the complexity of the tides.

4.5 Fault rheologies

Candidate rheologies for shearing of fault zones in the deep crust include rate dependent friction, dislocation glide, pressure solution, and dislocation creep. Rate dependent friction is the most often invoked mechanism of fault creep in the crust due to lab-demonstrated creep properties [e.g., *Moore and Rymer* (2007) and *Moore and Lockner* (2007)] and its ability to explain creep phenomenon such as afterslip (*Marone et al.*, 1991) and slip-driven aftershock sequences (*Perfettini and Avouac*, 2004). Rate dependent creep is most often associated with phyllosilicates (micas, talc, clays). Dislocation glide is a plasticity mechanism that arises in materials that undergo dislocation motion at low temperature, for example talc (*Escartin et al.*) and olivine (*Evans and Goetze*, 1979) at room temperature. For glide, dislocation climb is prevented at these temperatures due to kinetic or structural reasons. Dislocation creep arises at higher temperatures in olivine and also in most other silicates including quartz (*Evans*, 1984) but does not occur at high temperature in phyllosilicates (*Escartin et al.*). Pressure solution is a water assisted grain boundary diffusion creep mechanism that requires mineral dissolution, transport and precipitation [e.g., *Robin* (1978)]. The frictional strength of wet quartzofeldspathic rocks are thought to be limited by pressure solution (*Chester*, 1995). We consider each of the these mechanisms in turn.

Power law - Dislocation creep/pressure solution

Dislocation creep and pressure solution follow a power law rheology with the generic form

$$\dot{\varepsilon} = \dot{\varepsilon_0} A \left(\frac{\sigma}{\sigma_0} \right)^n \tag{4.6a}$$

where σ is the differential stress, A is a dimensionless constant and $\dot{\varepsilon_0}$ is the strain rate at the background strain rate which we associate with that at the plate velocity V_L. The differential stress at the background strain rate is σ_0 and n is the stress exponent, expected to be 1 for pressure solution and 3 to 6 for dislocation creep. Note that equation 4.6a(6a) uses different constants from the standard power law form for specific mechanisms. For example the flow law for dislocation creep is often written as where A has dimensions of strain rate/ stressn [e.g., *Hirth et al.* (2001)]. Our need to normalize the strain rate motivates the equivalent form (6a); for dislocation creep and , where Q is an activation energy, R is the gas constant, and T is absolute temperature. So long as the shear zone thickness is constant, as would be expected for steady state flow, then $\dot{\varepsilon}/\dot{\varepsilon_0} = V/V_L$, as above, and we expect for seismic failure of small brittle patches on a creeping fault plane

$$\frac{N_{obs}}{N_{exp}} = \frac{V}{V_L} = A \left(\frac{\sigma}{\sigma_0} \right)^n. \tag{4.6b}$$

Differential stress is related to shear stress in the direction of shearing by a geometrical constant ($\sigma = 2\tau/\sin(2\phi)$, where ϕ is the angle between the greatest principal stress and the fault zone) so the ratio $\sigma/\sigma_0 = \tau/\tau_0$. Defining $\Delta\tau = \tau - \tau_0$ as the deviation of shear stress

from its nominal stress level τ_0, $\Delta\tau$ is the periodic (tidal) component of the shear stress. So $\tau/\tau_0 = \Delta\tau/\tau_0 + 1$, and we find that the rheological equivalent of equation 4.5b for the data in Figure 4.1 is

$$\frac{N_{obs}}{N_{exp}} = \frac{V}{V_L} = A\left(\frac{\Delta\tau}{\tau_0} + 1\right)^n. \tag{4.6c}$$

Pressure solution is linearly viscous, $n = 1$; using this constraint the best fit value of the data in Figure 4.1 for b and the ambient shear stress, are 1.03 and 476 Pa, respectively (Figure 4.6). For dislocation creep we use a power law exponent $n = 4$ that is appropriate for quartz (*Hirth et al.*, 2001). For dislocation creep the best-fit value of A, and the ambient shear stress are 0.96 and 1704 Pa, respectively (Figure 4.6).

Dislocation glide

Dislocation glide can be represented by the flow law

$$\dot{\varepsilon} = \dot{\varepsilon_0}\left(\frac{\sigma}{\sigma_0}\right)^2 \exp\left(\frac{-Q}{RT}\left(1 - \sqrt{\frac{\sigma}{\sigma_p}}\right)\right) \tag{4.7a}$$

(*Mei et al.*, 2010; *Frost and Ashby*, 1982), where the reference strain rate, and differential stress have the same interpretation as in (6b). σ_p is the Peirels stress which is the yield strength at absolute zero and Q is activation energy at zero stress. Again replacing the ratio of differential stress to its reference value with the equivalent ratio of shear stress, replacing the differential stress with 2τ and considering an imposed change yields

$$\frac{N_{obs}}{N_{exp}} = \frac{V}{V_L} = \left(\frac{\Delta\tau}{\tau_0} + 1\right)^2 \exp\left(\frac{-Q}{RT}\left(1 - \sqrt{\frac{2(\Delta\tau + \tau_0)}{\sigma_p}}\right)\right) \tag{4.7b}$$

for glide. The data in Figure 4.1 were fit with the flow law (7b) resulting in $\tau_0 = 971$ Pa, $Q_p/RT = 0.56$ and $\sigma_p = 2133$ Pa (Figure 4.6).

Rate dependent friction

In room temperature experiments rock friction is constant to first order; to second order friction depends on slip speed and state (which is thought to represent, slip rate, slip, and time dependences) (*Dieterich*, 1979; *Ruina*, 1983) such as represented by rate and state constitutive relations. While rate and state dependences determine the stability of sliding they complicate analysis of stable fault creep which invariably arises when the direct rate dependence exceeds the state dependence (velocity strengthening). Accordingly, prior studies of afterslip and fault creep (*Marone et al.*, 1991; *Perfettini and Avouac*, 2004; *Ader et al.*, 2012) simplify the full rate and state equations by ignoring state; doing so is rigorously correct, for example, during sliding over short slip distances, or sliding at steady-state.

More general ignorance of state effects is appropriate for friction of some phyllosilicates such as muscovite and talc which lack a significant state dependence at room temperature [e.g., *Scruggs* (1997) and *Beeler* (2007)]. For simplicity, and other reasons detailed in the discussion section below we use talc as a representative phase for deep frictional slip on the SAF and assume purely rate dependent friction

$$\tau = \tau_0 + a\sigma \ln\left(\frac{V}{V_L}\right) \tag{4.8a}$$

where effective normal stress is σ_e, τ_0 is shear resistance at the nominal loading rate VL and a is a positive constant. Rearranging leads to

$$\frac{N_{obs}}{N_{exp}} = \frac{V}{V_L} = \exp\left(\frac{\Delta\tau}{a\sigma_e}\right). \tag{4.8b}$$

As above $\Delta\tau = \tau - \tau_0$ is the deviation of shear stress from its nominal stress level τ_0. And, as above, $\Delta\tau$ can be equated with the periodic (tidal) component of the shear stress. Data in Figure 4.1 are fit with (8b) to determine the single free parameter, the product $a\sigma_e$= 464 Pa.

Varying normal stress

The normal stress changes from the tides resolved onto the SAF are approximately ten times larger than the shear stresses, yet they have less influence on LFE occurrence (*Thomas et al.*, 2011). This would seem to place significant constraints on the fault rheology. Unfortunately, they do not. A primary reason is that, because pressure solution, dislocation glide and dislocation creep have nearly no dependence on normal stress, the observed lack of normal stress influence is expected for three out of the four rheologies considered. Another issue is that our model implemented with the fourth rheology, purely rate strengthening friction, rather than having a single dependent variable, as was the case with the shear stresses (equation 4.8b), has 4 (fault friction, fault normal stress, patch normal stress and a) for changing normal stress. This may be too many free parameters to well constrain fault properties. Finally, as discussed below there are poroelastic and hydraulic factors, independent of rheology, that may make deep frictional faults insensitive to tidal normal stress changes (*Hawthorne and Rubin*, 2010).

4.6 Discussion

We compare the inferred rheological constants from the fits of the data (Figure 4.3) to independent laboratory measurements of the expected values for the various rheologies. To make direct comparisons we use laboratory data from quartz, olivine and talc to represent the constants. Quartz was selected because it is brittle in the shallow crust and is well studied in the frictional regime where it is quite strongly rate weakening when deformation is localized

and not influenced by solution transport processes *Chester* (1995). It deforms by dislocation creep in the deeper crust (*Hirth et al.*, 2001) and it is among the most well studied minerals at elevated temperature and pressure. Olivine has a similar frictional strength to quartz but the underlying contact-scale deformation mechanisms are better understood than quartz (*Evans and Goetze*, 1979; *Boettcher et al.*, 2007). Low temperature plasticity operates in olivine at room temperature and extends to much greater temperatures (*Evans and Goetze*, 1979), as does the frictional regime (*Boettcher et al.*, 2007), and the flow behavior of olivine at high temperatures is well established (*Hirth and Kohlstedt*, 2003). Feldspar, which we do not consider in the present paper, has rheological properties that are intermediate between quartz and olivine [e.g., (*Scholz*, 2002)].

Talc is used to represent a material undergoing frictional creep. In the friction regime it is among the very weakest materials (*Moore and Lockner*, 2004; *Moore and Lockner*, 2007), if not the weakest, and the SAF is thought to be as weak as talc at least by some researchers (*Zoback et al.*, 1987). Talc is present in rock recovered from drilling through the SAF (*Moore and Rymer*, 2007). Talcs frictional properties are well described (*Scruggs*, 1997; *Morrow et al.*, 2000; *Moore and Lockner*, 2004; *Moore and Lockner*, 2007) and have a strong physical basis [e.g., *Morrow et al.* (2000); *Moore and Lockner* (2004); *Beeler* (2007). Talcs flow behavior is established over a limited range of conditions but it is not well studied nor or completely understood (*Hickman et al.*, 1997; *Escartin et al.*). Talc is hydrous and its dehydration temperature is just below the tremor zone, thus besides being mechanically relevant it provides a source of fluid, widely thought to play a role in the physical properties of the transition zone. Talc well represents the rheology of phyllosilicates which are generally not well studied but nonetheless, being a class of minerals that are common in mature fault zones, merit further examination.

Pressure solution

The physical interpretation of b and τ_0 in (6) for pressure solution depends on the assumed rate limiting step, diffusion or interface reaction control (*Rutter*, 1976; *Raj*, 1982). The rate limiting step is not well constrained by natural observations. Furthermore, even given knowledge of the rate limiting step there can be large differences in grain size sensitivity, depending on the particular grain scale theoretical model (*Gratz*, 1991; *den Brok*, 1998). Perhaps related to these are large differences between naturally inferred rates of quartz pressure solution and laboratory measured rates (*Gratz*, 1991) which may also indicate that the presence of secondary phases control the natural rates. These issues would make it difficult to verify whether fault creep of the SAF is consistent with a pressure solution mechanism. Fortunately, for pressure solution stress and strain rate are related linearly (*Rutter*, 1976; *Raj*, 1982) which is inconsistent with the observations (Figure 4.3). Pressure solution provides the worst fit of all the rheologies and the fit is outside the error bars of the observation over much of the tidal stress range (4.3) and we dismiss it as a likely mechanism.

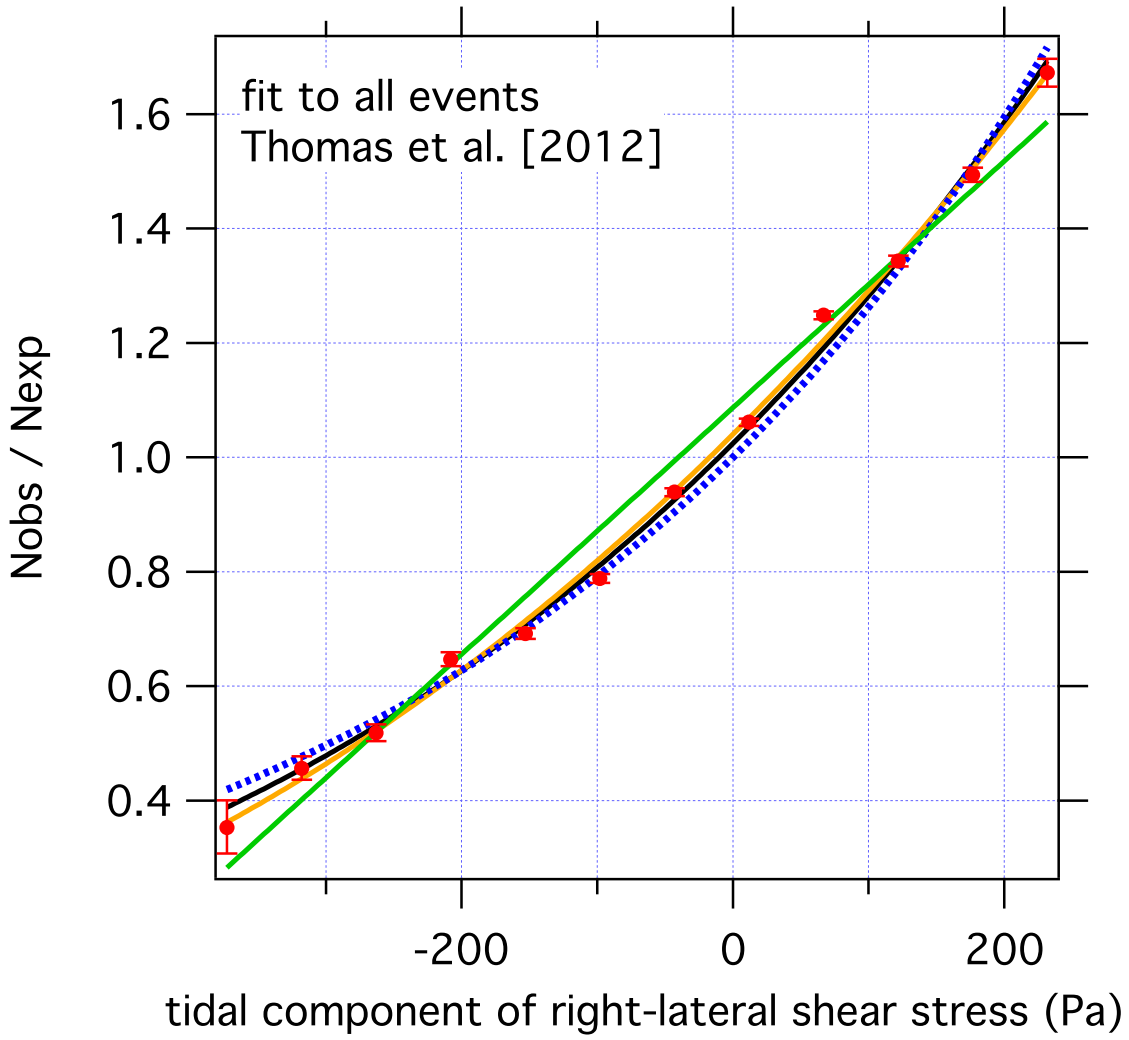

Figure 4.3: Data from *Thomas et al.* (2012) as shown in Figure 4A with fits to dislocation creep equation 4.6 (black), pressure solution equation 4.6 (green), dislocation glide equation 4.7 (orange) and purely rate strengthening friction equation 4.8 (blue dashed).

Dislocation creep

Dislocation creep (6) provides a much better fit to the observations than linear viscous pressure solution creep. Noting that the activation energy , the inferred value of Q at the depth averaged temperature of 505°C from the fit shown in Figure 4.3 is 0.257 kJ/mol. The activation of dislocation creep of quartz is $135kJ/mol$ (*Hirth et al.*, 2001) and for other rock forming minerals is of that order, for example for olivine Q = 480-520 kJ/mol, although olivine does not undergo dislocation creep at 500°C. Given the three order of magnitude difference in energy, dislocation creep can probably be eliminated for consideration as the controlling deformation mechanism for deep fault creep associated with NVT on the SAF. Similarly, though not independent of the activation energy, the value of nominal differential stress required, $\tau_0 \approx 3$ kPa, is too low to be plausible for quartz at these temperatures. Figure 4.6A shows the expected fault strength for dislocation creep on the SAF over the depth range of 15 to 30 km. The temperature profile used is from (*Blanpied et al.*, 1995) for the SAF based on *Lachenbruch and Sass* (1973) profile A. The figure shows values of τ_0 at strain rates of 10^-10, 10^-12, 10^-14/s which correspond to shear zone thicknesses of w = 10 m, 1 km and 100 km, respectively. The conversion of strain rate to thickness uses the plate rate V_L = 0.001 micron/s (31.6 mm/yr). As the weakest shear strength is associated with an implausible shear zone thickness and still is more than three orders of magnitude higher than the fit to dislocation creep, this process can be eliminated as a candidate to explain deep creep on the SAF. In addition, because of the large difference, our conclusion that dislocation creep of quartz does not control fault creep at these depths on the SAF can be extended to include other typical quartzofeldspathic and likely all possible compositions of crustal rocks.

Dislocation glide

Solving for the inferred value of the activation energy from the fit of equation 4.7b shown in Figure 4.3 at the depth averaged temperature of 505°C produces Q = 3.6 kJ/mol, whereas for dislocation glide, the operative mechanism of olivine crystal plasticity of olivine at 500°C and low strain rate, has Q = 523 kJ/mol *Evans and Goetze* (1979) to 320 kJ/mol (*Mei et al.*, 2010). Similarly, for talc the range inferred from *Hickman et al.* (1997) for talc is 56-85 kJ/mol. This rules out glide of olivine and talc as a candidate for controlling fault creep. More generally, the apparent activation energy for glide in silicates is on the order of many tens to many hundreds of kJ per mole [e.g., *Shea and Kronenberg* (1992)], therefore, we entirely eliminate glide as explaining deep fault creep on the SAF.

A similar conclusion is reached from the inferred shear strength from the fits. The nominal value of shear stress for the glide flow law has the same interpretation as for dislocation creep - it is the shear stress for deformation at the plate rate. The inferred value for glide is very low at 0.97 kPa and is of the same order as the tidal shear stresses themselves. Taking the differential stress to be twice the shear stress, the resulting 1.9 kPa is very low relative to the differential stress of olivine at these conditions (Figure 4.6b) which exceeds 500 MPa.

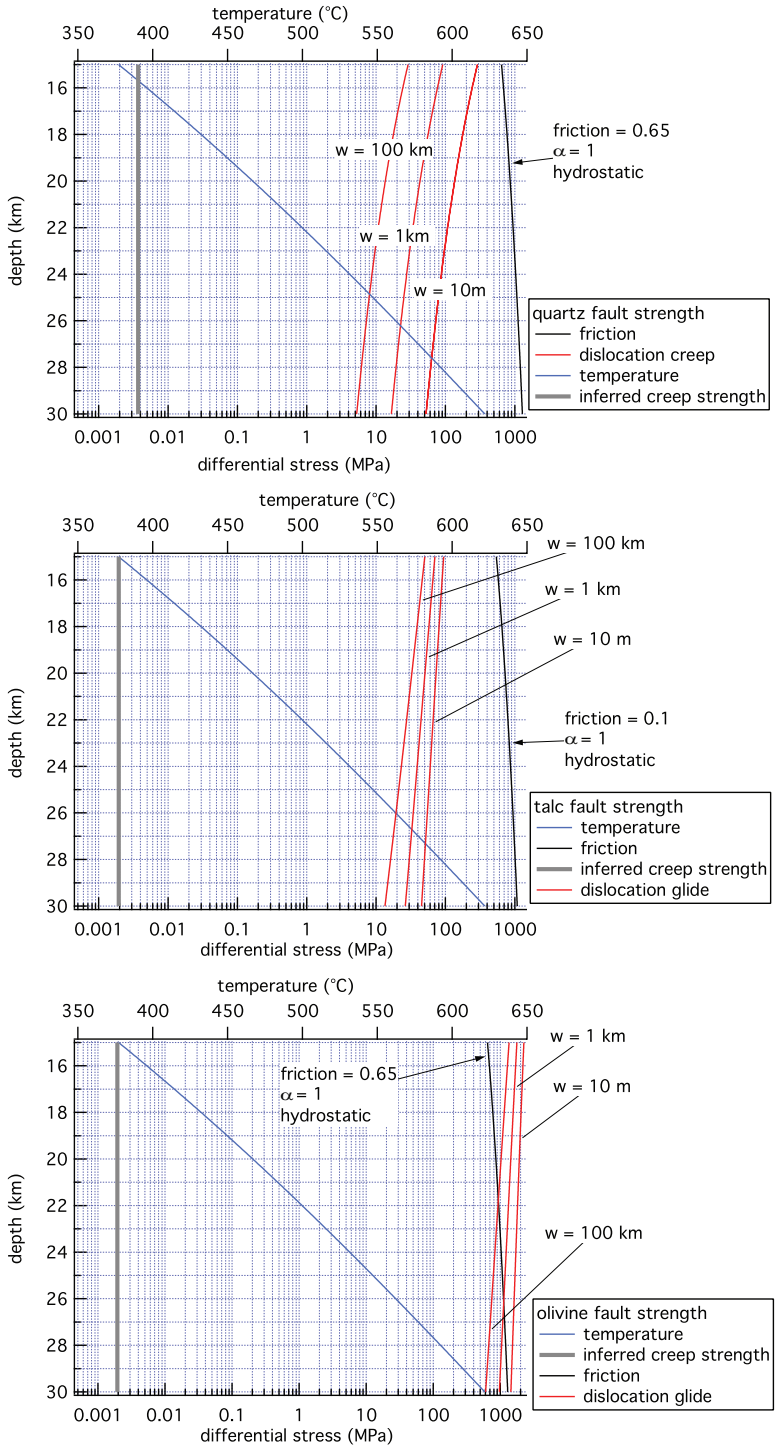
temperature (°C)
350 400 450 500 550 600 650
depth (km)
16 18 20 22 24 26 28 30
0.001 0.01 0.1 1 10 100 1000
differential stress (MPa)
w = 100 km
w = 1km
w = 10m
friction = 0.65
α = 1
hydrostatic
quartz fault strength
friction
dislocation creep
temperature
inferred creep strength
temperature (°C)
w = 100 km
w = 1 km
w = 10 m
friction = 0.1
α = 1
hydrostatic
talc fault strength
temperature
friction
inferred creep strength
dislocation glide
temperature (°C)
w = 1 km
w = 10 m
friction = 0.65
α = 1
hydrostatic
w = 100 km
olivine fault strength
temperature
inferred creep strength
friction
dislocation glide

Figure 4.4: The estimated shear strength of faults in the transition zone in a strike slip faulting environment. To estimate the stresses, we assume overburden, m, equal to the average of the greatest and least principal stresses, $(\sigma_1 + \sigma_3)/2$, [e.g., *Townend and Zoback* (2000)]. In the shallow faulting regime, the fault normal stress, for a fixed coefficient of friction μ, and an optimally oriented fault is $\sigma_n = \sigma_m \sin(\tan^{-1}\mu)\cos(\tan^{-1}\mu)/\mu$, and the fault differential stress for friction is $\sigma_\Delta = 2\mu(\sigma_n - \alpha p)/\cos(\tan^{-1}\mu)$. In the calculations shown pore pressure is hydrostatic (10 MPa/km) and overburden is 28 MPa/km. The resulting differential stress from friction is shown in black. Differential stress from the flow laws are shown in red at strain rates of $10^{-10}, 10^{-12}, 10^{-14}/s$ which correspond to shear zone thicknesses of w = 10 m, 1 km and 100 km, respectively. For flow due to dislocation glide or dislocation creep the fault differential strength is given by the flow law, equation 4.6 or 4.7b and the shear stress inferred from the data fit, is $\tau = \sigma_\Delta/2$. In blue is the temperature (top axis) estimated following *Lachenbruch and Sass* (1973) profile A for the San Andreas. Panel A: Quartz. The frictional strength (black) assumes $\mu = 0.65$ The grey line is the inferred differential strength from the fit of equation 4.6 to the data, σ_Δ = 3.4 kPa. In red are predictions of the flow law equation 4.6 for strain rates of quartz using $n = 4$, Q = 135 kJ/mol, and $\dot{\varepsilon_0}/\sigma_0^4 = 1 * 10^{-9}$ /MPa^{4}s [after *Hirth et al.* (2001)]. Panel B. Olivine. The frictional strength (black) assumes = 0.65. The grey line is the inferred differential strength from the fit of equation 4.7b to the data, σ_Δ = 1.9 kPa. In red are predictions of the flow law equation 4.7a, Q = 320 kJ/mol, σ_p = 5900 MPa, and $\dot{\varepsilon_0}/\sigma_0^2 = 1.4 * 10^{-7}$ /MPa^{2}s *Mei et al.* (2010). Panel C Talc. The frictional strength (black) assumes $\mu = 0.1$. The grey line is the inferred differential strength from the fit of equation 4.7b to the data, σ_Δ = 1.9 kPa. In red are predictions of the flow law equation 4.7a for talc using Q=166 kJ/mol, σ_p=377 MPa, and $\dot{\varepsilon_0}/\sigma_0^2 = 0.08$ /MPa^{2}s (*Hickman et al.*, 1997).

For talc the estimated differential stress is greater than 10 MPa based on our extrapolation of *Hickman et al.* (1997) and *Edmond and Paterson* (1971).

Rate dependent friction

For purely rate strengthening friction, the fit requires $a\sigma_e$ = 0.46 kPa. If the frictional parameter a for talc is controlled by low temperature plasticity, a is expected to increase in direct proportion to temperature (*Nakatani*, 2001; *Rice et al.*, 2001), following a flow law of the form (7). Comparison of the friction rate dependence at room temperature a = 0.0045 with rate dependence corrected for differences in stress and temperature shows good agreement (*Beeler*, 2007). Extrapolating the room temperature value to the transition zone results in a = 0.012 for talc. Assuming hydrostatic fluid pressure, the depth averaged effective normal stress is 401 MPa and expected ae for talc at this depth range is 4.8 MPa, four orders of magnitude higher than the fit to the tremor data (Figure 4.3). Thus, talc

friction could control the rate dependence only if the effective normal stress is 40 kPa, four orders of magnitude lower than our hydrostatic, $\alpha = 1$ assumption shown in Figure 4.6. That would require that the depth averaged fluid pressure to be elevated above hydrostatic by greater than 400 MPa.

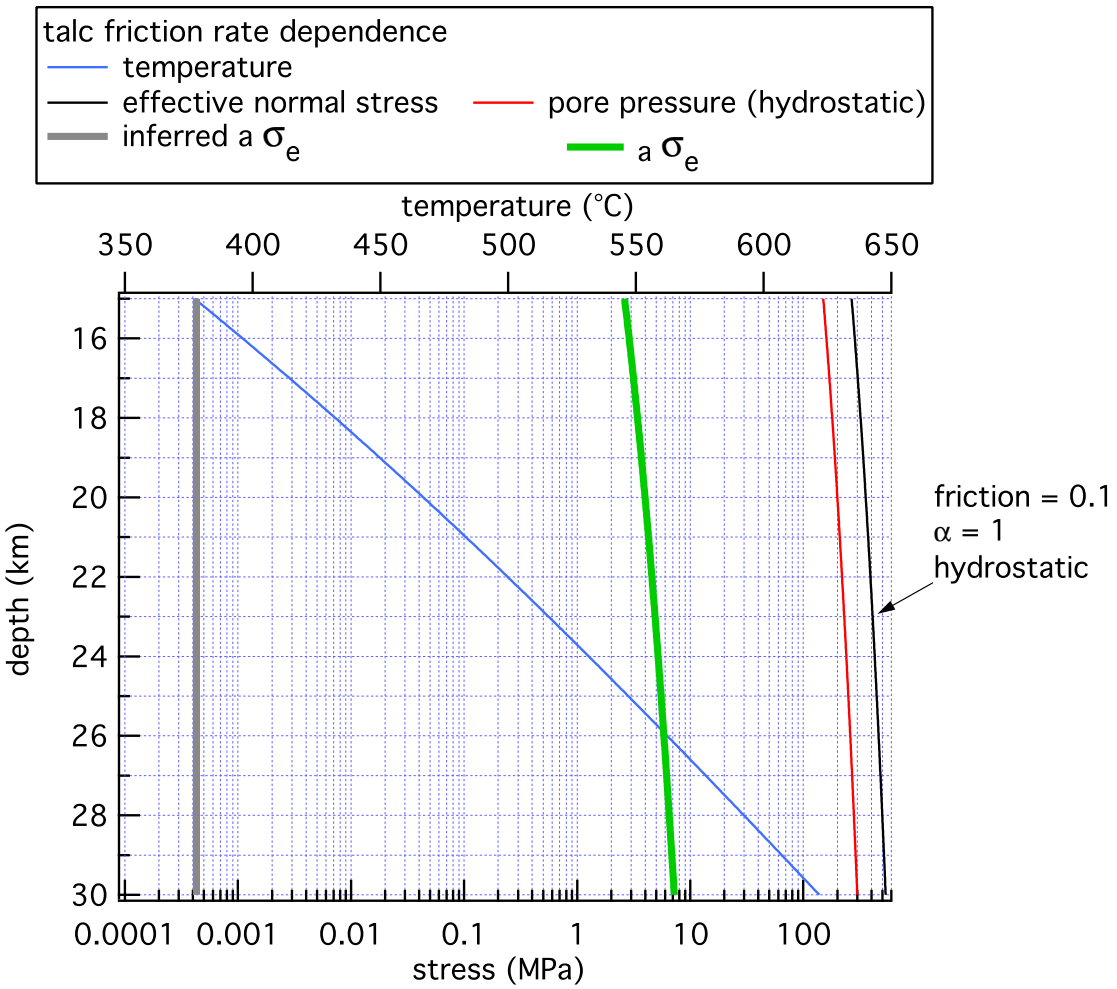

The effective normal stress and direct rate dependence of talc in the transition zone in a strike-slip faulting environment assuming hydrostatic fluid pressure. The stresses are calculated as described in the caption to Figure 4.6. The friction constitutive parameter a is assumed proportional to absolute temperature (see text) and has a depth-averaged value of 0.011 over this range; the product $a\sigma_e$ is plotted in green. For comparison is the inferred value of ae from the fit to *Thomas et al.* (2012) LFEs using equation 4.8a (grey). Temperature (top axis) is shown in blue.

Summary of constraints on shear stress from fault creep

The reason none of the conventional flow mechanisms can fit the observations with the expected rheological parameters is essentially because the small tidal stresses are producing a large effect on the strain rate. That is only possible for these flow mechanisms for rock forming minerals if the stress perturbation is on the order of the ambient material shear strength, τ_0. The failure of the mechanisms to represent the observations does imply indirectly that fault creep is controlled by friction, or in otherwords that the shear stress in the region of fault creep is lower than the flow strength. Since for quartz and talc the depth averaged flow strength expressed as shear stress is on the order of 10 MPa to 100 MPa (Figure 4.6), we can take this as the upper bound on shear strength of the creeping portion of the deep San Andreas in this region.

A possible lower bound on shear stress in the deep creeping portion comes from the fit with rate dependent friction. Taking the resulting value of $a\sigma_e = 0.46kPa$ and assuming talc friction with $a = 0.012$ and $m = 0.1$, if fault strength were controlled by talc, the average shear resistance in this depth range would be $\sim$4 kPa.

Constraints on fluid pressure and shear stress from the LFEs

The existence of low frequency earthquakes in the transition zone, when combined with the constraint on earthquake patch size from our analysis of fault creep puts a lower limit on effective pressure in the source. Since LFEs produce stress drops and radiated energy they are most easily explained by rate weakening friction (*Dieterich*, 1979; *Ruina*, 1983) and using the constraint on the maximum size of these events from our analysis of creep in the surrounding region we can consider a minimum effective normal stress that allows for the existence of length $L = 100$ m earthquakes at these depths. Taking the earthquake patch stiffness as $k_2 = G/(1-\nu)L$, where G is the shear modulus, ν is Poissons ratio, and the critical stiffness for instability to be $k_c = (b-a)\sigma_e/d_c$, we find the requirement for earthquake occurrence to be

$$\sigma_e > \frac{d_c G}{(b-a)(1-\nu)L} \tag{4.9}$$

(*Dieterich*, 1979). Here d_c, the slip weakening distance and $(b-a)$, the rate dependence, are the fault patchs frictional properties. Quartz is one of the most rate weakening of the crustal minerals, having $(b-a)$ at room temperature between 0.002 and 0.004 (*Chester*, 1995). Using the arguments of temperature proportionality (*Nakatani*, 2001) this extrapolates to depth as $b - a = 0.0078$. Using a lab $d_c = 5$ μm, appropriate for a lower bound on σ_e, G = 30000 MPa, and $\nu = 0.25$, the minimum effective pressure for earthquake occurrence is 0.26 MPa. This is nearly an order of magnitude higher than required for fault creep to be controlled by friction. Unfortunately, quartz is unlikely to be rate weakening at these depths *Chester* (1995). For olivine, which is known to be rate weakening up to 600°C, $b-a = 0.003$ (*Boettcher et al.*, 2007), making the minimum effective pressure in (9) $0.65MPa$, larger by

about a factor of 2.5. From this we can conclude that if friction controls fault creep and also controls the occurrences of LFEs significant material differences and differences in pore pressure between the creeping fault and the LFEs are required. The material difference is necessary to produce a change in sign of the rate dependence of friction from positive in the creeping region to negative in the seismic patches. The difference in pore pressure is required because the inferred effective normal stress of the creeping fault zone ($\sigma_e = 40$ kPa) is too low for the LFE patches to be unstable ($\sigma_e > 0.65$ MPa).

Shear stress at LFEs is controlled presumably by olivine, feldspar or similarly strong phase that is refractory at temperatures between 400 and 600°C, undergoing frictional sliding below the flow strength. The upper limit of shear strength for olivine is in the range of hundreds of MPa (Figure 4.6). An approximate lower limit follows from (9) using a friction coefficient of $\mu = 0.65$ we estimate 0.4 MPa.

Constraints from tidal normal stress

Among the potential reasons that the relatively large tidal normal stresses would produce weak changes in earthquake rate are

1. fault creep is controlled by a ductile process that has no normal stress dependence
2. fault creep is controlled by friction but the pore pressure in the fault is undrained over the time scale of the tidal period (*Hawthorne and Rubin*, 2010)
3. that fault creep is controlled by friction but that the intrinsic friction coefficient is very small (*Thomas et al.*, 2009).

Based on our analysis of tidally induced shear stresses on the SAF, we can eliminate 1 from consideration. For an undrained fault, as in 2, if the fault poroelastic properties are suitable changes in fault normal stress may produce no change in effective normal stress. The relation between normal stress change and fault pore pressure is characterized by the Skempton coefficient $B = dp/d\sigma_m$ where σ_m is the mean stress. Laboratory faults are *Brown and Scholz* (1985), and shallow crustal faults are thought to be, highly anisotropic, being much more compliant normal to the fault (*Cocco and Rice*, 2002) than in-plane. While it is uncertain whether or not faults at this depth are more compliant normal to the fault and whether the Skempton coefficient is 1, under such conditions $B \approx dp/d\sigma_n$. Therefore, as long as $B \approx 1$, as it is in the shallow subsurface, any change in normal stress is exactly counterbalanced by an opposing change in pore pressure (*Hawthorne and Rubin*, 2010). Undrained conditions might be expected at this depth due to low permeability resulting from high temperature and overburden (*Manning and Ingebritsen*, 1999).

With regard to 3, constraints on the intrinsic friction coefficient from the previous study of NVT on the SAF, *Thomas et al.* (2009) assumed that tremor occurrence reflects patch intrinsic properties, whereas in the present model tremor occurrence reflects the properties of the creeping fault surrounding the patch. Still, a similar constraint on fault friction

coefficient arises in the present model. As mentioned above, when normal stress changes are considered in the present model there are more free parameters to consider than a simple patch friction coefficient. There may be useful constraints on patch friction and ambient normal stress from this model but those are beyond the scope of the present study.

Suggested future research directions

The analysis and conclusions from analysis of tidal stress and LFE occurrence on the SAF in the present paper also apply to NVT on the SAF as described by *Thomas et al.* (2009). In that study tremor rate (minutes per day) is shown to correlate with the tidal shear stress (*Thomas et al.*, 2012, Figure 3). Those rate data when normalized by the average rate and cast in the context of the (*Shelly et al.*, 2007a) model have the same interpretation as N_{obs}/N_{exp} in the present study (equation 4.5d). Furthermore, when the normalized *Thomas et al.* (2009) data are fit with equations 4.6, 4.7 and 4.8 very similar rheological constants are found (Appendix, Table 1). The two catalogs were determined independently, using entirely different techniques and cover different time periods. This correspondence suggests that there are no significant differences between the occurrence of LFEs that compose a portion of the NVT tremor and the tremor as a whole. Because tremor catalogs are easier to construct from standard network data than LFEs, tremor detected in subduction environments could be analyzed for tidal sensitivity and the inferred source properties compared with the SAF. Related to such analysis is a need to evaluate whether the tectonic loading/rate and state model of tidal triggering (*Dieterich*, 1987; *Lockner and Beeler*, 1999) can be excluded for NVT/LFEs in subduction zones as was concluded by *Thomas et al.* (2011, 2012) for the SAF.

Single LFE families show behaviors significantly different than the average (*Thomas et al.*, 2012, Supplement) both in shear and normal stress sensitivity. In the case of the shear tides, often the maximum rate of occurrence lags behind the peak tidal stress *Thomas et al.* (2012). This lag cannot arise in the present model if equation 4.5d holds and the creeping fault is purely rate dependent. So the lag may be symptomatic of a more complicated frictional relation [Allan Rubin, personal communication; *Ader et al.* (2012)], deviations of the LFE from our idealized small source model [Allan Rubin, personal communication], local deviations of the fault strike from the assumed surface trend, fluid effects delaying failure time or other unimagined possibilities. Some LFE families show resolvable systematic correlation with normal stress. These too may reflect differences in rheology, geometry or effective normal stress and are intended targets of our future work.

4.7 Conclusion

The occurrence rate of low frequency earthquakes among non-volcanic tremor on the deep extent of the San Andreas fault in central California shows strong systematic correlation with the daily solid earth tides resolved as shear stress in the direction of right-lateral slip

on the fault (*Thomas et al.*, 2012). The rate of LFE occurrence is in phase with this tidal stress, the amplitude of the SAF shear stress tides is 400 Pa and the rate of occurrence is modulated by 75%. This behavior can be well represented by a model in which the LFE sources are small seismic patches that fail at a threshold stress and that are on an otherwise creeping fault plane. In such a model, the seismic patches are loaded tectonically, directly by the tides and also by time-dependent creep of the surrounding fault. Fault creep dominates LFE occurrence so long as the LFE source is 100 m or smaller. Under these restrictive conditions the model predicted LFE rate is proportional to the fault creep rate.

Using the observed occurrence data, the model can constrain the rheological properties of the creeping fault, essentially by equating the occurrence rate vs tidal stress data to a strain rate vs stress relationship and fitting that data with candidate rheologies. We find that ductile processes: dislocation creep, dislocation glide and pressure solution are not consistent with the observed fault creep in the source region of NVT, because for rock forming minerals these processes require a nominal flow strength on the order the tidal stress to produce the observed strongly modulated occurrence rate. Lab observed flow strengths are higher by orders of magnitude for a wide range of possible fault materials and conditions. Purely rate dependent friction can be consistent with the observations but only if the product of the friction rate dependence and effective normal stress is extremely low, approximately 0.5 kPa. For talc the friction rate dependence extrapolated to this depth is on the order of 0.01 which we take to be typical for frictional creep of phyllosilicates in the deep crust. This would require the effective normal stress to be $\sim$50 kPa. Were effective normal stress this low, and friction controlled by talc, the SAF shear resistance would be $\sim$4 kPa.

Given the failure of all the ductile rheologies in explaining the observations, the lack of laboratory studies of faulting in the presence of pore fluid at the temperature and pressures of the transition zone, and the extremely low inferred shear stress, our conclusion that friction controls fault creep is one that is not verified experimentally and will be difficult to verify. Nevertheless, if the LFE source is as small as 100 m, temperature extrapolated friction properties require that the minimum effective pressure at the LFE source is $\sim$0.65 MPa. Therefore if lab-like friction controls both fault creep and seismicity, then there are both material contrasts and differences in effective stress between the creeping and seismic parts of the fault.

The weak correlation between the normal stress component of the tides and LFE occurrence is not explained by our work, despite the relatively large amplitude of the tidal normal stress being approximately ten times the shear stress that strongly correlates. For this model we present here there may be too many free parameters to produce unique constraints on fault rheological parameters. There are likely hydraulic and/or poroelastic phenomena that reduce the sensitivity to normal stress at these depths.

Chapter 5

Conclusion

In the work presented here I have shown that both tremor and LFEs in Parkfield are sensitive to stresses induced by the solid Earth tides. While the tidally-induced normal stresses are nearly an order of magnitude larger than shear stresses, the latter appear to be dominant in modulating NVT and LFE occurence. One way for such small stresses to be effective at depth where pressure is high is for pore fluids within the fault zone to be at similarly high pressures reducing the effective normal stress to near zero. Other researchers have come to similar conclusions using different datasets and analysis techniques. Additionally, low effective stress is favored in many models of slow slip. For example, in models that involve quasi-dynamic changes in pore fluid pressure, the slip quenching mechanism (i.e. dilatancy) is more effective at low effective stress. Nevertheless, it is important to thouroughly vet inferences before accepting them as fact as there are observations that cannot be explained solely by implicating high-pore fluid pressures. For example, if near-lithostatic pore fluid pressures are present in the LFE source region then there should be little to no correlation with normal stress changes. While this is largely true, there are some families that have shear and normal stress N_{ex} values of near 30%. There are ways to circumvent this problem, but they require parameter tuning that may be unjustified. In the end these inconsistencies suggest that we revisit the assumptions in our analysis and theoretical considerations of how deep faults should operate to better understand what implications our data have for the mechanical properties of deep faults. Ultimately, the fact that there is no unifying framework for understanding the spectrum of fault slip behaviors is also very exciting and bodes well for the future of the field.

Bibliography

Ader, T. J., J.-P. Ampuero, and J.-P. Avouac (2012), The role of velocity-neutral creep on the modulation of tectonic tremor activity by periodic loading, *Geophys. Res. Lett.*, *39*, L16310, doi:10.1029/2012GL052326.

Agnew, D. C. (1997), NLOADF: A program for computing ocean-tide loading, *Journal of Geophysical Research*, *102*(B3), 5109–5110.

Ando, R., R. Nakata, and T. Hori (2010), A slip pulse model with fault heterogeneity for low-frequency earthquakes and tremor along plate interfaces, *Geophys. Res. Lett.*, *37*, L10310, doi:10.1029/2010GL043056.

Audet, P., M. G. Bostock, N. I. Christensen, and S. M. Peacock (2009), Seismic evidence for overpressured subducted oceanic crust and megathrust fault sealing, *Nature*, *457*, 76–78, doi:10.1038/nature07650.

Bartlow, N. M., D. Lockner, and N. M. Beeler (2010), The effect of water on triggering of stick slip by oscillatory loading meeting, *2010 SCEC Annual Meeting*, (2-095).

Bartlow, N. M., S. Miyazaki, A. M. Bradley, and P. Segall (2011), Space-time correlation of slip and tremor during the 2009 Cascadia slow slip event, *Geophys. Res. Lett.*, *38*, L18309, doi:10.1029/2011GL048714.

Becken, M., O. Ritter, S. K. Park, P. A. Bedrosian, U. Weckmann, and M. Weber (2008), A deep crustal fluid channel into the San Andreas Fault system near Parkfield, California, *Geophysical Journal International*, *173*, 718–732, doi:10.1111/j.1365-246X.2008.03754.x.

Beeler, N. M. (2007), Laboratory-observed faulting in intrinsically and apparently weak materials: Strength, seismic coupling, dilatancy, and pore-fluid pressure, in *The Seismogenic Zone of Subduction Thrust Faults*, edited by T. H. Dixon and C. J. Moore, Margins theoretical and experimental earth science, p. 317, Columbia University Press.

Beeler, N. M., and D. A. Lockner (2003), Why earthquakes correlate weakly with the solid Earth tides: Effects of periodic stress on the rate and probability of earthquake occurrence, *Journal of Geophysical Research (Solid Earth)*, *108*, 2391, doi:10.1029/2001JB001518.

Beroza, G. C., and S. Ide (2011), Slow Earthquakes and Nonvolcanic Tremor, *Annual Review of Earth and Planetary Sciences*, *39*, 271–296, doi:10.1146/annurev-earth-040809-152531.

Bilham, R., and G. King (1989), The morphology of strike-slip faults - Examples from the San Andreas Fault, California, *Journal of Geophysical Research*, *941*, 10,204–10,216, doi:10.1029/JB094iB08p10204.

Blanpied, M. L., D. A. Lockner, and J. D. Byerlee (1995), Frictional slip of granite at hydrothermal conditions, *Journal of Geophysical Research*, *1001*, 13,045–13,064, doi:10.1029/95JB00862.

Boettcher, M., G. Hirth, and B. Evans (2007), Olivine friction at the base of oceanic seismogenic zones, *Journal of Geophysical Research*, *112*(B1), B01,205.

Boyarko, D. C., and M. R. Brudzinski (2010), Spatial and temporal patterns of nonvolcanic tremor along the southern Cascadia subduction zone, *Journal of Geophysical Research (Solid Earth)*, *115*, B00A22, doi:10.1029/2008JB006064.

Brenguier, F., M. Campillo, C. Hadziioannou, N. M. Shapiro, R. M. Nadeau, and E. Larose (2008), Postseismic Relaxation Along the San Andreas Fault at Parkfield from Continuous Seismological Observations, *Science*, *321*, 1478–1481, doi:10.1126/science.1160943.

Brown, J. R., G. C. Beroza, S. Ide, K. Ohta, D. R. Shelly, S. Y. Schwartz, W. Rabbel, M. Thorwart, and H. Kao (2009), Deep low-frequency earthquakes in tremor localize to the plate interface in multiple subduction zones, *Geophys. Res. Lett.*, *36*, L19306, doi:10.1029/2009GL040027.

Brown, S. R., and C. H. Scholz (1985), Closure of random elastic surfaces in contact, *Journal of Geophysical Research*, *90*(B7), 5531–5545.

Brudzinski, M. R., H. R. Hinojosa-Prieto, K. M. Schlanser, E. Cabral-Cano, A. Arciniega-Ceballos, O. Diaz-Molina, and C. DeMets (2010), Nonvolcanic tremor along the Oaxaca segment of the Middle America subduction zone, *Journal of Geophysical Research (Solid Earth)*, *115*, B00A23, doi:10.1029/2008JB006061.

Bufe, C. G., P. W. Harsh, and R. O. Burford (1977), Steady-state seismic slip-A precise recurrence model, *Geophys. Res. Lett.*, *4*, 91–94, doi:10.1029/GL004i002p00091.

Bürgmann, R., and G. Dresen (2008), Rheology of the Lower Crust and Upper Mantle: Evidence from Rock Mechanics, Geodesy, and Field Observations, *Annual Review of Earth and Planetary Sciences*, *36*, 531–567, doi:10.1146/annurev.earth.36.031207.124326.

Cembrano, J., A. Lavenu, P. Reynolds, G. Arancibia, G. Lopez, and A. Sanhueza (2002), Late Cenozoic transpressional ductile deformation north of the Nazca-South America-Antarctica triple junction, *Tectonophysics*, *354*, 289–314, doi:10.1016/S0040-1951(02)00388-8.

Chester, F. (1995), A rheologic model for wet crust applied to strike-slip faults, *Journal of Geophysical Research*, *100*(B7), 13,033–13,044.

Cocco, M., and J. R. Rice (2002), Pore pressure and poroelasticity effects in coulomb stress analysis of earthquake interactions, *Journal of Geophysical Research*, *107*(2030), doi:10.1126/science.1103961.

Cochran, E. S., J. E. Vidale, and S. Tanaka (2004), Earth Tides Can Trigger Shallow Thrust Fault Earthquakes, *Science*, *306*, 1164–1166, doi:10.1126/science.1103961.

de Juan, J., P. Elósegui, M. Nettles, T. B. Larsen, J. L. Davis, G. S. Hamilton, L. A. Stearns, M. L. Andersen, G. Ekström, A. P. Ahlstrøm, L. Stenseng, S. A. Khan, and R. Forsberg (2010), Sudden increase in tidal response linked to calving and acceleration at a large Greenland outlet glacier, *Geophys. Res. Lett.*, *371*, L12501, doi:10.1029/2010GL043289.

den Brok, S. (1998), Effect of microcracking on pressure-solution strain rate: The gratz grain-boundary model, *Geology*, *26*(10), 915–918.

Dieterich, J. (1979), Modeling of rock friction 1. experimental results and constitutive equations, *Journal of Geophysical Research*, *84*(B5), 2161–2168.

Dieterich, J. (1987), Nucleation and triggering of earthquake slip: effect of periodic stresses, *Tectonophysics*, *144*, 127–139, doi:10.1016/0040-1951(87)90012-6.

Dieterich, J. (1992), Earthquake nucleation on faults with rate-and state-dependent strength, *Tectonophysics*, *211*, 115–134, doi:10.1016/0040-1951(92)90055-B.

Dieterich, J. (1994), A constitutive law for rate of earthquake production and its application to earthquake clustering, *J. Geophys. Res.*, *99*, 2601–2618, doi:10.1029/93JB02581.

Dieterich, J. H. (2007), Applications of Rate- and State-Dependent Friction to Models of Fault Slip and Earthquake Occurrence, *Treatise on Geophysics*, *4*, 107–129, doi: doi:10.1016/B978-044452748-6.00065-1.

Dieterich, J. H., and B. Kilgore (1996), Implications of Fault Constitutive Properties for Earthquake Prediction, *Proceedings of the National Academy of Science*, *93*, 3787–3794, doi:10.1073/pnas.93.9.3787.

Dieterich, J. H., and B. D. Kilgore (1994), Direct observation of frictional contacts: New insights for state-dependent properties, *Pure and Applied Geophysics*, *143*, 283–302, doi: 10.1007/BF00874332.

Dragert, H., K. Wang, and T. S. James (2001), A Silent Slip Event on the Deeper Cascadia Subduction Interface, *Science*, *292*, 1525–1528, doi:10.1126/science.1060152.

Dragert, H., K. Wang, and G. Rogers (2004), Geodetic and seismic signatures of episodic tremor and slip in the northern Cascadia subduction zone, *Earth, Planets, and Space*, *56*, 1143–1150.

Edmond, J., and M. Paterson (1971), Strength of solid pressure media and implications for high pressure apparatus, *Contributions to Mineralogy and Petrology*, *30*(2), 141–160.

Escartin, J., M. Andreani, G. Hirth, and B. Evans (), Relationships between the microstructural evolution and the rheology of talc at elevated pressures and temperatures, *Earth and Planetary Science Letters*, *268*(3), 463–475.

Evans, B. (1984), The effect of temperature and impurity content on indentation hardness of quartz, *Journal of Geophysical Research*, *89*(B6), 4213–4222.

Evans, B., and C. Goetze (1979), The temperature variation of hardness of olivine and its implication for polycrystalline yield stress, *Journal of Geophysical Research*, *84*(B10), 5505–5524, doi:10.1029/JB084iB10p05505.

Fletcher, J. B., and A. McGarr (2011), Moments, magnitudes, and radiated energies of nonvolcanic tremor near Cholame, CA, from ground motion spectra at UPSAR, *Geophys. Res. Lett.*, *381*, L16314, doi:10.1029/2011GL048636.

Frost, H., and M. Ashby (1982), Deformation mechanism maps: the plasticity and creep of metals and ceramics.

Ghosh, A., J. E. Vidale, Z. Peng, K. C. Creager, and H. Houston (2009), Complex nonvolcanic tremor near Parkfield, California, triggered by the great 2004 Sumatra earthquake, *Journal of Geophysical Research (Solid Earth)*, *114*, B00A15, doi:10.1029/2008JB006062.

Gomberg, J., J. L. Rubinstein, Z. Peng, K. C. Creager, J. E. Vidale, and P. Bodin (2008), Widespread Triggering of Nonvolcanic Tremor in California, *Science*, *319*, 173–, doi:10.1126/science.1149164.

Gratz, A. J. (1991), Solution-transfer compaction of quartzites: progress toward a rate law, *Geology*, *19*(9), 901–904.

Gu, J., J. R. Rice, A. L. Ruina, and S. T. Tse (1984), Slip motion and stability of a single degree of freedom elastic system with rate and state dependent friction, *Journal of Mechanics Physics of Solids*, *32*, 167–196, doi:10.1016/0022-5096(84)90007-3.

Harkrider, D. G. (1970), Surface waves in multilayered elastic media. Part II. Higher mode spectra and spectral ratios from point sources in plane layered Earth models, *Bulletin of the Seismological Society of America*, *60*(6), 1937–1987.

Hart, R. H. G., M. T. Gladwin, R. L. Gwyther, D. C. Agnew, and F. K. Wyatt (1996), Tidal calibration of borehole strain meters: Removing the effects of small-scale inhomogeneity, *Journal of Geophysical Research (Solid Earth)*, *101*, doi:10.1029/96JB02273.

Hawthorne, J. C., and A. M. Rubin (2010), Tidal modulation of slow slip in Cascadia, *Journal of Geophysical Research (Solid Earth)*, *115*, B09406, doi:10.1029/2010JB007502.

Heaton, T. H. (1982), Tidal triggering of earthquakes, *Bulletin of the Seismological Society of America*, *72*(6), 2181–2200.

Hickman, J. B., E. N. Zhurina, and A. K. Kronenberg (1997), Deformation of talc and pyrophyllite: Disruption of van der Waals bonds and comparisons with calculated interlayer forces, *Eos Trans. AGU*, *78*, Fall Meet. Suppl., Abstract F724.

Hill, D. P. (2010), Surface-Wave Potential for Triggering Tectonic (Nonvolcanic) Tremor, *The Bulletin of the Seismological Society of America*, *100*, 1859–1878, doi:10.1785/0120090362.

Hirose, H., K. Hirahara, F. Kimata, N. Fujii, and S. Miyazaki (1999), A slow thrust slip event following the two 1996 Hyuganada earthquakes beneath the Bungo Channel, southwest Japan, *Geophys. Res. Lett.*, *26*, 3237–3240, doi:10.1029/1999GL010999.

Hirth, G., and D. Kohlstedt (2003), Rheology of the upper mantle and the mantle wedge: A view from the experimentalists, *GEOPHYSICAL MONOGRAPH-AMERICAN GEOPHYSICAL UNION*, *138*, 83–106.

Hirth, G., C. Teyssier, and J. Dunlap (2001), An evaluation of quartzite flow laws based on comparisons between experimentally and naturally deformed rocks, *International Journal of Earth Sciences*, *90*, 77–87, doi:10.1007/s005310000152.

Houston, H., B. G. Delbridge, A. G. Wech, and K. C. Creager (2011), Rapid tremor reversals in Cascadia generated by a weakened plate interface, *Nature Geoscience*, *4*, 404–409, doi:10.1038/ngeo1157.

Ide, S. (2010), Striations, duration, migration and tidal response in deep tremor, *Nature*, *466*, 356–359, doi:10.1038/nature09251.

Ide, S., G. C. Beroza, D. R. Shelly, and T. Uchide (2007), A scaling law for slow earthquakes, *Nature*, *447*, 76–79, doi:10.1038/nature05780.

Kao, H., S.-J. Shan, H. Dragert, G. Rogers, J. F. Cassidy, and K. Ramachandran (2005), A wide depth distribution of seismic tremors along the northern Cascadia margin, *Nature*, *436*, 841–844, doi:10.1038/nature03903.

Kao, H., K. Wang, H. Dragert, J. Y. Kao, and G. Rogers (2010), Estimating seismic moment magnitude (M_w) of tremor bursts in northern Cascadia: Implications for the "seismic efficiency" of episodic tremor and slip, *Geophys. Res. Lett.*, *371*, L19306, doi:10.1029/2010GL044927.

Knopoff, L. (1964), Earth tides as a triggering mechanism for earthquakes, *The Bulletin of the Seismological Society of America*, *54*, 1865–1870.

Lachenbruch, A. H., and J. H. Sass (1973), Thermo-mechanical aspects of the san andreas fault system, in *Proceedings of the Conference on Tectonic Problems of the San Andreas Fault System*, vol. 13, p. 192, Stanford University Press.

Lambert, A., H. Kao, G. Rogers, and N. Courtier (2009), Correlation of tremor activity with tidal stress in the northern Cascadia subduction zone, *Journal of Geophysical Research (Solid Earth)*, *114*, B00A08, doi:10.1029/2008JB006038.

Little, T. A., R. J. Holcombe, and B. R. Ilg (2002), Kinematics of oblique collision and ramping inferred from microstructures and strain in middle crustal rocks, central Southern Alps, New Zealand, *Journal of Structural Geology*, *24*, 219–239, doi:10.1016/S0191-8141(01)00060-8.

Liu, Y., and J. R. Rice (2005), Aseismic slip transients emerge spontaneously in three-dimensional rate and state modeling of subduction earthquake sequences, *Journal of Geophysical Research (Solid Earth)*, *110*, B08307, doi:10.1029/2004JB003424.

Liu, Y., and J. R. Rice (2007), Spontaneous and triggered aseismic deformation transients in a subduction fault model, *Journal of Geophysical Research (Solid Earth)*, *112*, B09404, doi:10.1029/2007JB004930.

Lockner, D. A., and N. M. Beeler (1999), Premonitory slip and tidal triggering of earthquakes, *Journal of Geophysical Research*, *104*, 20,133–20,152, doi:10.1029/1999JB900205.

Manning, C. E., and S. E. Ingebritsen (1999), Permeability of the continental crust: Implications of geothermal data and metamorphic systems, *Reviews of Geophysics*, *37*(1), 127–150, doi:doi:10.1029/1998RG900002.

Marone, C. (1998), Laboratory-derived friction laws and their application to seismic faulting, *Annual Reviews of Earth and Planetary Sciences*, *26*, 643–696.

Marone, C., and B. Kilgore (1993), Scaling of the critical slip distance for seismic faulting with shear strain in fault zones, *Nature*, *362*, 618–621, doi:10.1038/362618a0.

Marone, C. J., C. H. Scholtz, and R. Bilham (1991), On the mechanics of earthquake afterslip, *J. Geophys. Res.*, *96*, 8441–8452, doi:10.1029/91JB00275.

McNutt, S. R., and R. J. Beavan (1984), Patterns of earthquakes and the effect of solid earth and ocean load tides at Mount St. Helens prior to the May 18, 1980, eruption, *Journal of Geophysical Research*, *89*, 3075–3086, doi:10.1029/JB089iB05p03075.

Mei, S., A. M. Suzuki, D. L. Kohlstedt, N. A. Dixon, and W. B. Durham (2010), Experimental constraints on the strength of the lithospheric mantle, *Journal of Geophysical Research (Solid Earth)*, *115*, B08204, doi:10.1029/2009JB006873.

Métivier, L., O. de Viron, C. P. Conrad, S. Renault, M. Diament, and G. Patau (2009), Evidence of earthquake triggering by the solid earth tides, *Earth and Planetary Science Letters*, *278*, 370–375, doi:10.1016/j.epsl.2008.12.024.

Miller, M. M., T. Melbourne, D. J. Johnson, and W. Q. Sumner (2002), Periodic slow earthquakes from the Cascadia subduction zone, *Science*, *295*, 2423, doi: 10.1126/science.1071193.

Miyazawa, M., and E. E. Brodsky (2008), Deep low-frequency tremor that correlates with passing surface waves, *Journal of Geophysical Research (Solid Earth)*, *113*, B01307, doi: 10.1029/2006JB004890.

Moore, D. E., and D. A. Lockner (2004), Crystallographic controls on the frictional behavior of dry and water-saturated sheet structure minerals, *Journal of Geophysical Research (Solid Earth)*, *109*, B03401, doi:10.1029/2003JB002582.

Moore, D. E., and D. A. Lockner (2007), Friction of the smectite clay montmorillonite: A review and interpretation of data, in *The Seismogenic Zone of Subduction Thrust Faults*, edited by T. H. Dixon and C. J. Moore, Margins theoretical and experimental earth science, p. 317, Columbia University Press.

Moore, D. E., and M. J. Rymer (2007), Talc-bearing serpentinite and the creeping section of the San Andreas fault, *Nature*, *448*, 795–797, doi:10.1038/nature06064.

Morrow, C. A., D. E. Moore, and D. A. Lockner (2000), The effect of mineral bond strength and adsorbed water on fault gouge frictional strength, *Geophys. Res. Lett.*, *27*, 815–818, doi:10.1029/1999GL008401.

Murray, J., and J. Langbein (2006), Slip on the San Andreas Fault at Parkfield, California, over Two Earthquake Cycles, and the Implications for Seismic Hazard, *Bull. Seism. Soc. Am.*, *96*, 283, doi:10.1785/0120050820.

Nadeau, R. M., and D. Dolenc (2005), Nonvolcanic Tremors Deep Beneath the San Andreas Fault, *Science*, *307*, 389, doi:10.1126/science.1107142.

Nadeau, R. M., and A. Guilhem (2009), Nonvolcanic Tremor Evolution and the San Simeon and Parkfield, California, Earthquakes, *Science*, *325*, 191–194, doi: 10.1126/science.1174155.

Nadeau, R. M., and L. R. Johnson (1998), Seismological studies at Parkfield VI: moment release rates and estimates of source parameters for small repeating earthquakes, *Bull. Seism. Soc. Am.*, *88*, 790–814, doi:110.1126/science.1090353.

Nadeau, R. M., and T. V. McEvilly (2004), Periodic Pulsing of Characteristic Microearthquakes on the San Andreas Fault, *Science*, *303*, 220–222, doi: 110.1126/science.1090353.

Nakata, R., N. Suda, and H. Tsuruoka (2008), Non-volcanic tremor resulting from the combined effect of Earth tides and slow slip events, *Nature Geoscience*, *1*, 676–678, doi: 10.1038/ngeo288.

Nakatani, M. (2001), Conceptual and physical clarification of rate and state friction: Frictional sliding as a thermally activated rheology, *J. Geophys. Res.*, *106*, 13,347–13,380, doi:10.1029/2000JB900453.

Obara, K. (2002), Nonvolcanic Deep Tremor Associated with Subduction in Southwest Japan, *Science*, *296*, 1679–1681, doi:10.1126/science.1070378.

Obara, K. (2010), Phenomenology of deep slow earthquake family in southwest Japan: Spatiotemporal characteristics and segmentation, *Journal of Geophysical Research (Solid Earth)*, *115*, B00A25, doi:10.1029/2008JB006048.

Obara, K., H. Hirose, F. Yamamizu, and K. Kasahara (2004), Episodic slow slip events accompanied by non-volcanic tremors in southwest Japan subduction zone, *Geophys. Res. Lett.*, *312*, L23602, doi:10.1029/2004GL020848.

Peng, Z., and J. Gomberg (2010), An integrated perspective of the continuum between earthquakes and slow-slip phenomena, *Nature Geoscience*, *3*, 599–607, doi:10.1038/ngeo940.

Peng, Z., J. E. Vidale, A. G. Wech, R. M. Nadeau, and K. C. Creager (2009), Remote triggering of tremor along the San Andreas Fault in central California, *Journal of Geophysical Research (Solid Earth)*, *114*, B00A06, doi:10.1029/2008JB006049.

Perfettini, H., and J.-P. Avouac (2004), Postseismic relaxation driven by brittle creep: A possible mechanism to reconcile geodetic measurements and the decay rate of aftershocks, application to the Chi-Chi earthquake, Taiwan, *Journal of Geophysical Research (Solid Earth)*, *109*, B02304, doi:10.1029/2003JB002488.

Raj, R. (1982), Creep in polycrystalline aggregates by matter transport through a liquid phase, *J. Geophys. Res.*, *87*, 4731–4739, doi:10.1029/JB087iB06p04731.

Rice, J., N. Lapusta, and K. Ranjith (2001), Rate and state dependent friction and the stability of sliding between elastically deformable solids, *Journal of the Mechanics and Physics of Solids*, *49*(9), 1865–1898.

Rice, J. R., and A. L. Ruina (1983), Stability of Steady Frictional Slipping, *Journal of Applied Mechanics*, *50*, 343, doi:10.1115/1.3167042.

Robin, P. Y. F. (1978), Pressure solution at grain-to-grain contacts, *Geochimica et Cosmochimica Acta*, *42*(9), 1383–1389.

Rogers, G., and H. Dragert (2003), Episodic Tremor and Slip on the Cascadia Subduction Zone: The Chatter of Silent Slip, *Science*, *300*, 1942–1943, doi:10.1126/science.1084783.

Rubin, A. M. (2008), Episodic slow slip events and rate-and-state friction, *Journal of Geophysical Research (Solid Earth)*, *113*, B11414, doi:10.1029/2008JB005642.

Rubin, A. M. (2011), Designer friction laws for bimodal slow slip propagation speeds, *Geochemistry, Geophysics, Geosystems*, *120*, Q04007, doi:10.1029/2010GC003386.

Rubinstein, J. L., J. E. Vidale, J. Gomberg, P. Bodin, K. C. Creager, and S. D. Malone (2007), Non-volcanic tremor driven by large transient shear stresses, *Nature*, *448*, 579–582, doi:10.1038/nature06017.

Rubinstein, J. L., M. La Rocca, J. E. Vidale, K. C. Creager, and A. G. Wech (2008), Tidal Modulation of Nonvolcanic Tremor, *Science*, *319*, 186–, doi:10.1126/science.1150558.

Ruina, A. (1983), Slip instability and state variable friction laws, *Journal of Geophysical Research*, *881*, 10,359–10,370, doi:10.1029/JB088iB12p10359.

Rutter, E. H. (1976), The Kinetics of Rock Deformation by Pressure Solution, *Royal Society of London Philosophical Transactions Series A*, *283*, 203–217, doi:10.1098/rsta.1976.0079.

Ryder, I., and R. Bürgmann (2008), Spatial variations in slip deficit on the central San Andreas Fault from InSAR, *Geophysical Journal International*, *175*, 837–852, doi:10.1111/j.1365-246X.2008.03938.x.

Schmidt, D. A., and H. Gao (2010), Source parameters and time-dependent slip distributions of slow slip events on the Cascadia subduction zone from 1998 to 2008, *Journal of Geophysical Research (Solid Earth)*, *115*, B00A18, doi:10.1029/2008JB006045.

Scholz, C. H. (2002), *The Mechanics of Earthquakes and Faulting*.

Schulz, W. H., J. W. Kean, and G. Wang (2009), Landslide movement in southwest Colorado triggered by atmospheric tides, *Nature Geoscience*, *2*, 863–866, doi:10.1038/ngeo659.

Scruggs, V. J. (1997), Frictional constitutive properties and related microstructures of albite, muscovite, biotite and talc, Ph.D. thesis, Brown University.

Segall, P., A. M. Rubin, A. M. Bradley, and J. R. Rice (2010), Dilatant strengthening as a mechanism for slow slip events, *Journal of Geophysical Research (Solid Earth)*, *115*, B12305, doi:10.1029/2010JB007449.

Shea, W. T., and A. K. Kronenberg (1992), Rheology and deformation mechanisms of an isotropic mica schist, *J. Geophys. Res.*, *97*, 15,201, doi:10.1029/92JB00620.

Shelly, D. R. (2009), Possible deep fault slip preceding the 2004 Parkfield earthquake, inferred from detailed observations of tectonic tremor, *Geophys. Res. Lett.*, *36*, L17318, doi:10.1029/2009GL039589.

Shelly, D. R. (2010), Periodic, Chaotic, and Doubled Earthquake Recurrence Intervals on the Deep San Andreas Fault, *Science*, *328*, 1385–, doi:10.1126/science.1189741.

Shelly, D. R., and J. L. Hardebeck (2010), Precise tremor source locations and amplitude variations along the lower-crustal central San Andreas Fault, *Geophys. Res. Lett.*, *37*, L14301, doi:10.1029/2010GL043672.

Shelly, D. R., and K. M. Johnson (2011), Tremor reveals stress shadowing, deep postseismic creep, and depth-dependent slip recurrence on the lower-crustal San Andreas fault near Parkfield, *Geophys. Res. Lett.*, *381*, L13312, doi:10.1029/2011GL047863.

Shelly, D. R., G. C. Beroza, S. Ide, and S. Nakamula (2006), Low-frequency earthquakes in Shikoku, Japan, and their relationship to episodic tremor and slip, *Nature*, *442*, 188–191, doi:10.1038/nature04931.

Shelly, D. R., G. C. Beroza, and S. Ide (2007a), Non-volcanic tremor and low-frequency earthquake swarms, *Nature*, *446*, 305–307, doi:10.1038/nature05666.

Shelly, D. R., G. C. Beroza, and S. Ide (2007b), Complex evolution of transient slip derived from precise tremor locations in western Shikoku, Japan, *Geochemistry, Geophysics, Geosystems*, *81*, Q10014, doi:10.1029/2007GC001640.

Shelly, D. R., W. L. Ellsworth, T. Ryberg, C. Haberland, G. S. Fuis, J. Murphy, R. M. Nadeau, and R. Bürgmann (2009), Precise location of San Andreas Fault tremors near Cholame, California using seismometer clusters: Slip on the deep extension of the fault?, *Geophys. Res. Lett.*, *36*, L01303, doi:10.1029/2008GL036367.

Shelly, D. R., Z. Peng, D. P. Hill, and C. Aiken (2011), Triggered creep as a possible mechanism for delayed dynamic triggering of tremor and earthquakes, *Nature Geoscience*, *4*, 384–388, doi:10.1038/ngeo1141.

Simpson, R. W., M. Barall, J. Langbein, J. R. Murray, and M. J. Rymer (2006), San Andreas Fault Geometry in the Parkfield, California, Region, *The Bulletin of the Seismological Society of America*, *96*, 28, doi:10.1785/0120050824.

Smith, E. F., and J. Gomberg (2009), A search in strainmeter data for slow slip associated with triggered and ambient tremor near Parkfield, California, *Journal of Geophysical Research (Solid Earth)*, *114*, B00A14, doi:10.1029/2008JB006040.

Thomas, A., N. M. Beeler, R. Burgmann, and D. R. Shelly (2011), The frequency dependence of friction in experiment, theory, and observations of low frequency earthquakes, *AGU Fall Meeting Abstracts*, p. B2249.

Thomas, A. M., R. M. Nadeau, and R. Bürgmann (2009), Tremor-tide correlations and near-lithostatic pore pressure on the deep San Andreas fault, *Nature*, *462*, 1048–1051, doi:10.1038/nature08654.

Thomas, A. M., R. Bürgmann, D. R. Shelly, N. M. Beeler, and M. L. Nadeau (2012), Tidal triggering of low frequency earthquakes near Parkfield, California: Implications for fault mechanics within the brittle-ductile transition, *Journal of Geophysical Research (Solid Earth)*, *117*, B05301, doi:doi:10.1029/2011JB009036.

Thurber, C., H. Zhang, F. Waldhauser, A. Michael, J. Hardebeck, and D. Eberhart-Phillips (2006), Three-Dimensional Compressional Wavespeed Model, Earthquake Relocations (1966- 2005), and Focal Mechanisms for the Parkfield, California, Region, *The Bulletin of the Seismological Society of America*, *96*, 38, doi:10.1785/0120050825.

Townend, J., and M. D. Zoback (2000), How faulting keeps the crust strong, *Geology*, *28*, 399, doi:10.1130/0091-7613(2000)28¡399:HFKTCS¿2.0.CO;2.

Vidale, J. E., D. C. Agnew, M. J. S. Johnston, and D. H. Oppenheimer (1998), Absence of earthquake correlation with Earth tides: An indication of high preseismic fault stress rate, *Journal of Geophysical Research*, *1032*, 24,567–24,572, doi:10.1029/98JB00594.

Waldhauser, F., and D. P. Schaff (2008), Large-scale relocation of two decades of Northern California seismicity using cross-correlation and double-difference methods, *Journal of Geophysical Research (Solid Earth)*, *113*, B08311, doi:10.1029/2007JB005479.

Wech, A. G., and K. C. Creager (2011), A continuum of stress, strength and slip in the Cascadia subduction zone, *Nature Geoscience*, *4*, 624–628, doi:10.1038/ngeo1215.

Wech, A. G., K. C. Creager, and T. I. Melbourne (2009), Seismic and geodetic constraints on Cascadia slow slip, *Journal of Geophysical Research (Solid Earth)*, *114*, B10316, doi: 10.1029/2008JB006090.

Wilcock, W. S. D. (2001), Tidal triggering of microearthquakes on the Juan de Fuca Ridge, *Geophysical Research Letters*, *28*, 3999–4002, doi:10.1029/2001GL013370.

Zoback, M., M. Zoback, J. Eaton, V. Mount, and J. Suppe (1987), New evidence on the state of stress of the san andreas fault system, *Science*, *238*(4830), 1105–1111.